Structural characterisation of cyanobacterial phytochrome Cph1

Dissertation

zur Erlangung des akademischen Grades eines

Doktors der Naturwissenschaften (Dr. rer. nat.)

dem

Fachbereich Biologie und Chemie der Justus-Liebig-Universität

Gießen

vorgelegt von

Joël Mailliet

aus

Niederfeulen (Luxembourg)

Gießen 2011

Erstgutachter:

Prof. Ph.D. Jon Hughes

Fachbereich Biologie u. Chemie, Justus-Liebig-Universität Gießen

Zweitgutachter:

Prof. Dr. Lars-Oliver Essen

Fachbereich Chemie, Philipps-Universität Marburg

Parts of this work were published in:

Mailliet, J., Psakis, G., Sineshchekov, V., Essen, L. O. & Hughes, J.

Spectroscopy and a high-resolution crystal structure of Tyr-263 mutants of cyanobacterial phytochrome Cph1

J. Mol. Biol.: accepted (2011)

Mailliet, J., Psakis, G., Schroeder, C., Kaltofen, S., Durrwang, U., Hughes, J., & Essen, L. O.

Dwelling in the dark: procedures for the crystallography of phytochromes and other photochromic proteins

Acta Crystallographica Section D 65: 1232-1235. (2009)

Essen, L.-O., Mailliet, J., & Hughes, J.

The structure of a complete phytochrome sensory module in the Pr ground state

Proc. Natl. Acad. Sci. USA 105: 14709-14714. (2008)

1. Introduction

Living organisms use a multitude of different physicochemical sensors to perceive and adapt to various environmental cues. One important family of sensors are photoreceptors, which absorb and react to specific light stimuli to trigger appropriate responses on a genetic and physiological level. Plants, in particular, have developed a wide variety of specific photoreceptors not only to use light as an energy source, but also to control their growth and development depending on different light conditions.

Photoreceptors are initially classified according to their absorbing wavelength range. Physiological experiments presume the existence of UV-B sensors in plants (1, 2) and recently UVR8 has been identified to perceive UV-B via a specific tryptophan (3). Several families of blue-light receptors, absorbing light between 320 and 500 nm (UV-A and blue), exist in plants: phototropins using a flavin mononucleotide (FMN) as chromophore are responsible for phototropism, stomata opening and chloroplast movement (4), cryptochromes utilise flavin adenine dinucleotide (FAD) as catalytic and pterins as antenna cofactors to regulate deetiolation, flowering and the circadian clock in plants (5, 6). Zeitlupe (ZTL/FKF1/LKP1/ADO1) is another family of blue-light photoreceptors involved in the circadian rhythm of plants (7) which use FMN to perceive blue light.

In the late nineteen fifties Butler and Siegelman (8) discovered a family of photoreceptors capable of distinguishing between red (R, 660 nm) and far red (FR, 730 nm) light: phytochrome.

1.1. Phytochrome

In plants, phytochromes regulate many developmental processes like seed germination, seedling deetiolation, shade avoidance responses and flowering (9). Phytochromes were thought to be exclusive to the plant kingdom, but with the increased sequencing of bacterial as well as eukaryotic genomes, the R / FR photoreceptors were also discovered in cyanobacteria

(10, 11) participating in phototaxis (12), nonoxygenic bacteria regulating pigment biosynthesis (13), fungi (14) involved in the repression of sexual development (15), and lately in diatoms (16).

1.1.1. Domain architecture and classification

Canonical phytochromes consist of two modules: the sensor part perceives the light and transmits the energy to the transmitter module (17). The sensory moiety of the photoreceptor comprises an N-terminal extension of variable length, the Period/Arnt/Singleminded (PAS), cGMP phosphodiesterase / adenylyl cyclase / FhlA (GAF) and phytochrome-specific (PHY) domains. Both the GAF and PHY domains belong to the PAS superfamily (18, 19). The transmitter module is a protein kinase composed of a dimerisation and phosphoacceptor (DHP/DXP) and a catalytic ATPase (CAT) domain (Figure 1). In bacterial (BphP and Cph) and fungal (Fph) phytochromes, the phosphoacceptor in the kinase module is a histidine. In fungi and diatoms (Dph), the response regulator (RR) follows directly after the C-terminal transmitter module contrary to other phytochromes, where the RR constitutes a separate protein. Phosphorylation assays showed that higher plant phytochromes (phyA-E) have an active serine / threonine protein kinase (20). Autophosphorylation of plant phytochromes are thought to be involved in the regulation of phytochrome stability (21, 22). Furthermore, plant phytochromes possess two plant-specific PAS domains (PSP), located between the sensor and the transmitter.

Phytochromes use an open-chain tetrapyrrole, covalently attached to a cysteine via a thioether link, to perceive light. BphP and Fph utilize biliverdin (BV) bound to an N-terminal cysteine as chromophore, the first product of the heme breakdown accomplished by a heme oxygenase (HO). Cyanobacterial and plant phytochromes fix phycocyanobilin (PCB) or phytochromobilin (PΦB) respectively to a cysteine located within the GAF domain.

Apart from the canonical ones, there are phytochromes that deviate from the general domain architecture: *Synechococcus* OSA and OSB' Cph1-like phytochromes (SyA / B) lack the N-terminal PAS domain in the sensor module. *Synechocystis* Cph2-like phytochromes present a

completely different domain architecture: irrespective of the missing PAS domain, Cph2 is also deficient of a transmitter module. The photoreceptor is comprised of two N-terminal GAF domains, the former being able to covalently bind the chromophore PCB. This bidomain is followed by a diguanylate cyclase (GGDEF) and an EAL domain, which are responsible for the production and degradation of cyclic diGMP respectively (23, 24). A third GAF domain, with a covalently attached PCB and a second GGDEF domain complete this unusual phytochrome family, which is not only able to absorb R/FR but also responds to blue light (25).

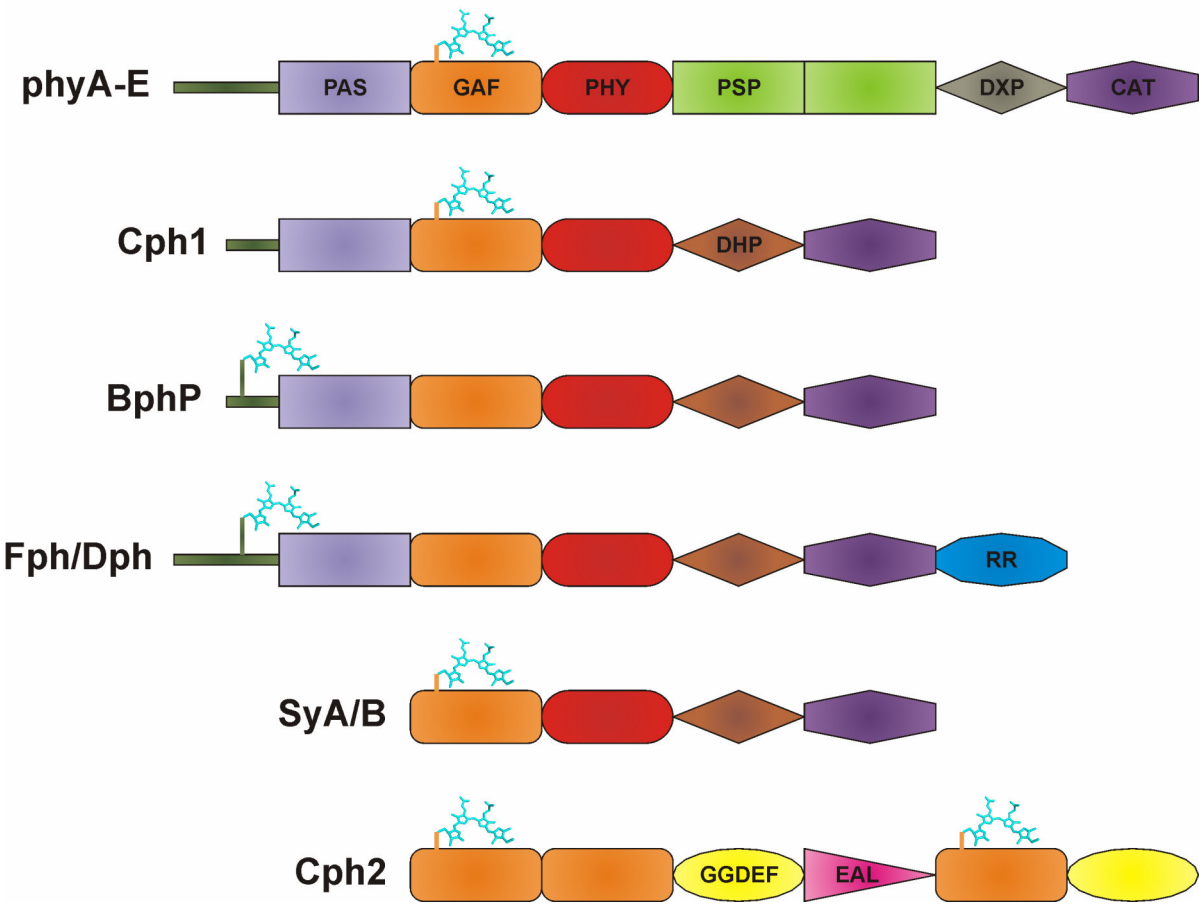

Figure 1: Domain architecture of known phytochrome families.
The variable N-terminal extension is shown in dark green, the PAS, GAF and PHY domains of the sensor module are shown in slate, orange and red respectively. The plant-specific PAS repeat is shown in green. The dimerisation / phosphoacceptor and the ATPase domain are grey/brown or violet respectively. The response regulator (RR) of the Fph / Dph phytochromes is coloured blue. The cyclic-diGMP regulating domains GGDEF and EAL are shown in yellow and pink respectively. The chromophore with its attachment site either in the extreme N-terminal region or within the GAF domain is shown in cyan.

Aside from the classification according to their domain structure, phytochromes can further be subdivided depending on the light quality they absorb. Canonical phytochromes are in the

R absorbing Pr ground state (in darkness) and photoconvert to the FR absorbing Pfr state upon irradiation with R light. Bathyphytochromes, which present the same domain architecture, have the Pfr form as their ground state (26). Furthermore, there are PCB-binding GAF proteins similar to phytochromes (cyanobacteriochromes), that are able to distinguish between red and green (27, 28) or blue and green (29) light respectively.

1.1.2. 3D crystal structure

The first three-dimensional crystal structure of the PAS-GAF bidomain from the sensor module of the BphP in the Pr ground state from *Deinococcus radiodurans* was solved at 2.5 Å resolution in 2005 (30). A surprising feature of this structure is observed in the tight interaction of the PAS and GAF domain via a figure-of-eight knot formed between the N-terminus and a protruding loop from the GAF domain (Figure 2). This knot is formed by conserved residues in the PAS and GAF domains, implying that this rare structural phenomenon is present in all canonical phytochromes. The chromophore BV is deeply buried within the GAF cavity. The A-ring vinyl group of the chromophore, which forms the thioether linkage with Cys-24, is also in close proximity to Met-259, which corresponds to the conserved cysteine residue binding PCB or PΦB in cyanobacterial and plant phytochromes respectively. This suggests that the chromophore pocket does not considerably differ in structural terms within the different phytochrome families. In published X-Ray structure of the PAS-GAF moiety of the bacteriophytochrome DrBphP1, the chromophore BV is not completely shielded from the solvent. Furthermore, this bidomain is not able to photoconvert to a stable Pfr state. These two observations suggest that a) the PHY domain and hence a complete sensor module is necessary for immaculate photoconversion from Pr to Pfr and b) the PHY domain somehow interacts with the GAF domain.

Indeed, the surface representation of the 1ZTU structure, coloured according to the sequence identity among various phytochrome families, shows that not only the knot region, but also the chromophore cavity is highly conserved (Figure 3). Furthermore, this illustration suggests that the missing PHY domain might be covering and thus sealing the chromophore pocket.

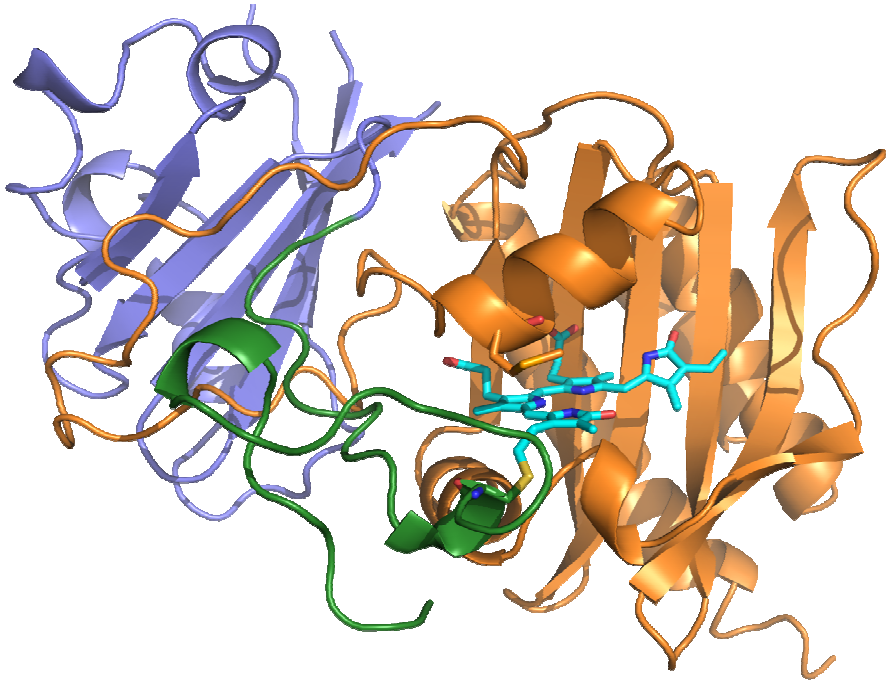

Figure 2: Cartoon representation of the *D. radiodurans* PAS-GAF bidomain structure.
The N-terminal random-coil extension (shown in dark green) binds BV (cyan) to Cys-24 and forms a knot with the GAF (shown in orange) protrusion. The PAS domain is represented in slate. Cys-24, which covalently binds BV and its structural homolog in plants and cyanobacteria Met-259 are shown as sticks (PDB code: 1ZTU).

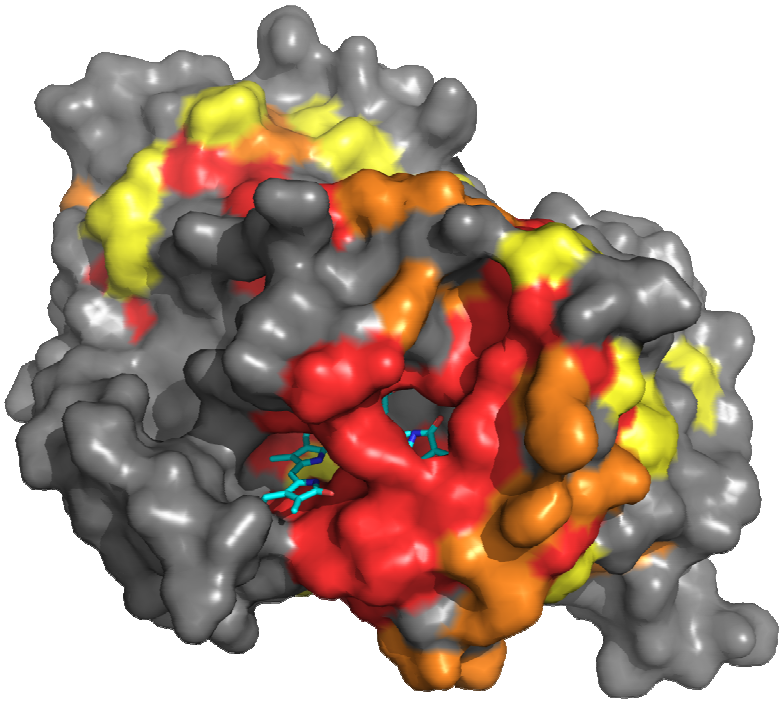

Figure 3: Surface representation of the *D. radiodurans* PAS-GAF bidomain structure.
The surface is coloured according to the sequence identity among different phytochrome families, where 90 % conservation is shown in red, 75 % in orange and 60 % in yellow. The chromophore BV (shown in cyan), buried within the GAF domain, is clearly accessible to the outside solvent (based on figure 4a from (30)).

In 2007, a high-resolution structure (1.5 Å) of the *D. radiodurans* PAS-GAF bidomain with a single surface mutation, revealed a more detailed insight in the chromophore attachment to Cys-24 (31). The 3D structure of the *Rhodopseudomonas palustris* phytochrome 3 (RpBphP3) PAS-GAF bidomain showed that phytochromes with an unusual photoconversion from Pr to the near-red absorbing Pnr state display the same 3D structure as canonical phytochromes (32).

1.1.3. Photoconversion mechanism

As mentioned above, phytochromes use a covalently attached, open-chain tetrapyrrole to absorb light in the red region and switch between two stable states: the R absorbing Pr and FR absorbing Pfr form. Upon irradiation with R, the chromophore changes its configuration from *5Zsyn, 10Zsyn, 15Zanti* to *ZZEssa* by photoisomerisation of the C15 = C16 double bond between the C and D ring (33-36) and moves from the Pr ground state to the excited lumi-R state (37, 38) (Figure 4).

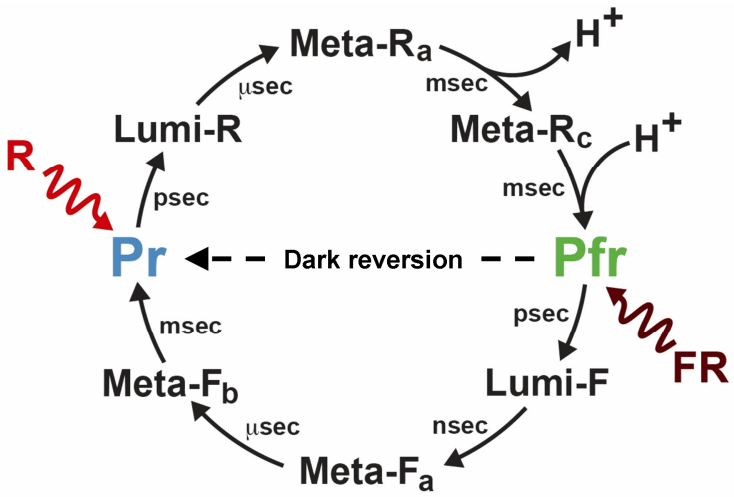

Figure 4: Phytochrome photocycle modified from (39).
The Pr ground state absorbs R light to convert to the Pfr form via intermediates Lumi-R, Meta-Ra and Meta-Rc respectively. A de- and reprotonation of the chromophore (Meta-Rc) is necessary for the formation of the meta-stable Pfr state. Pfr either converts back by FR irradiation or reverts back in darkness to the Pr state.

This transition constitutes a two-step process: the first step involves the formation of an unstable temperature-dependent pre-lumi-R state necessitating an activation barrier to be overcome and probably corresponds to D ring isomerisation (Figure 5). This process occurs with a quantum efficiency close to unity at ambient temperature, but competes with the

fluorescent decay to Pr at low temperatures. In a second step, pre-lumi-R may either revert back to the Pr ground state or transform into lumi-R thus dictating the overall quantum yield of phototransformation (37). The extended π-electron system in the excited lumi-R state allows the chromophore to absorb light at higher wavelengths, notably in the FR region. From excited lumi-R, phytochrome switches to the Meta-Ra state and reaches Meta-Rc by a temporary deprotonation of the chromophore. Reprotonation of the chromophore leads to the meta-stable Pfr state (33, 40). FR converts the chromophore back to the Pr state via similar intermediates designated lumi-F, meta-Fa and meta-Fb respectively (41, 42). Generally, the active Pfr state is not stable for a long period of time: in darkness, canonical phytochromes revert back to the Pr ground state by thermal relaxation. This process is known as dark reversion (43, 44).

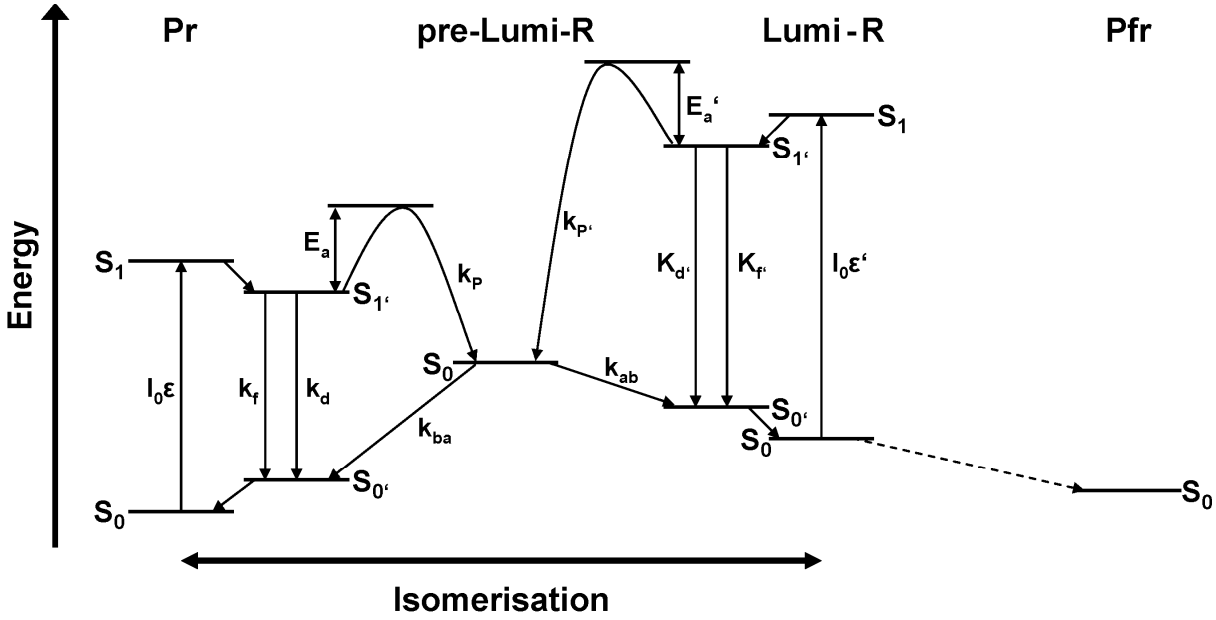

Figure 5: Energy and transition scheme of phytochrome photoconversion from Pr to Lumi-R.
This hypothetical scheme (37, 45) shows the transition of exciting light (I_0) from the ground state (S_0) to the excited state (S_1), the rate constants of fluorescence (kf), the temperature-independent degradation of excitation (k_d), the primary photoreaction from Pr to pre-lumi-R (k_P), the phototransformation into Lumi-R (k_{ab}) and finally the return to the initial ground state (k_{ba}) and the activation energy of the temperature-dependent primary photoreaction (E_a).

1.2. Cyanobacterial phytochrome Cph1

1.2.1. Cph1 as a model phytochrome

The discovery of cyanobacterial phytochrome Cph1 from *Synechocystis 6803* refuted the long thought belief that phytochromes are exclusive to the plant kingdom (10). Cph1 displays the same domain structure and a high sequence similarity in the sensor module to plant phytochromes. In contrast to biliverdin binding phytochromes, the attachment site of the chromophore is located within the GAF domain. These facts make Cph1 an ideal candidate to study not only the structure/ function but also the photoconversion mechanism of phytochromes in general. Cph1 does not possess the plant-specific PAS repeats and binds PCB, as stated above.

The C-terminal transmitter module comprises a DHP and CAT domain and hence Cph1 constitutes a true sensory histidine protein kinase (SHPK), capable of hydrolysing ATP for autophosphorylation and subsequent transmission to the response regulator Rcp1. Interestingly, the Pr ground state of Cph1 shows phosphorylation activity whereas the Pfr state does not transfer the phosphor to Rcp1 (11, 46). Furthermore, there is practically no dark reversion from Pfr to the Pr ground state. Whether and how these observations have any implications on the regulation of Cph1 activity cannot be determined, since the physiological function of Cph1 is still unknown.

1.2.2. Photochemical properties

Cph1, as all phytochromes to date, is able to covalently attach its chromophore to a cysteine within the GAF domain autocatalytically. The absorbance maximum of the Pr form is around 660 nm. Upon irradiation with saturating R with the same wavelength only ~ 70 % (80 % in plants (47)) is converted to the Pfr state, which has its maximum at ~ 705 nm, due to the fact that Pfr also absorbs light in the red region and converts back to Pr. Thus irradiation with R

results in a photoequilibrium with a mixed population of Pr and Pfr. When irradiated with FR ($\lambda_{max} \approx 730$ nm), almost 100 % occupancy of the Pr state is reached.

Removing the C-terminal transmitter module does not influence the absorbance properties of Cph1, hence a truncated version of this phytochrome, Cph1Δ2, consisting of the first 514 amino acids, constitutes a perfect model to study the structure/function of the sensor module of phytochromes in general (11). The chromophore PCB is synthesized from heme by two enzymes: HO and ferredoxin oxidoreductase (PcyA). By using a dual plasmid system, it is possible to obtain *in vivo* assembled phytochrome in *E. coli*, which not only enables the production of holoprotein, but also offers the possibility of *in vivo* studies (48, 49).

1.2.3. Protein-chromophore interactions

Site-directed mutagenesis of conserved amino acids in the GAF domain revealed key residues supposed to be involved in the photoconversion mechanism. Mutation of Tyr-176 almost completely prevents Cph1 from converting from Pr to Pfr. Interestingly, locking the chromophore in the Pr state leads to a significant increase of fluorescence, making Cph1 an ideal fluorescent marker for *in vivo* imaging (50-52). Furthermore, the same mutation results in a light-independent constitutively active phytochrome in plants (53) and might be one of the two tyrosines, hypothesized to be essential for photoconversion (54).

NMR studies have shown that the chromophore has fully protonated nitrogens in both the Pr and Pfr states (55, 56). Furthermore, the chromophore gets deprotonated prior to Meta-Rc formation and reprotonated to form Pfr (40). Two possible crucial residues have been identified to be involved in the protonation step: Asp-207 and His-260 (57). Mutation of Asp-207 leads to a bleaching effect after R irradiation: the Pr peak is reduced, but there is no formation of the Pfr peak. Mutating His-260 results in pH-dependent Pfr formation strongly suggesting that this residue is indeed involved in the protonation of the chromophore. The structure of the chromophore binding bidomain from *D. radiodurans* shows that these conserved residues are located below (Asp-207) and above (His-260) the chromophore, enabling them to hypothetically accept and/or transfer a proton (30).

1.3. Aim of this work

The X-Ray structure of the *D. radiodurans* PAS-GAF bidomain published in 2005 gave new and important insights into the structure/function of the sensor module of phytochromes and revealed key amino acids implicated in the photoconversion mechanism (30). However, missing the crucial PHY domain, this protein is not able to form stable Pfr and is thus photochemically impotent. This work aims to crystallise and solve the 3D structure of the complete and fully functional sensor module of the cyanobacterial phytochrome Cph1 from *Synechocystis 6803*: Cph1Δ2.

Key residues involved in the photoconversion mechanism have been previously described without relying on structural data of phytochrome (50, 57). Based on the obtained X-Ray structure of Cph1Δ2, this work aims to identify crucial amino acids within the PAS, GAF and PHY domains, involved in the protonation of the chromophore and photoconversion mechanism in general. Site-directed mutagenesis of these residues and characterisation of the resulting mutants will show how they interact with the chromophore and function within the sensor module. Crystallisation and structure solution of important players in the phototransformation mechanism will hopefully give new insights in how canonical phytochromes work.

2. Material and methods

2.1. Material

2.1.1. Instruments

Autoclave	FVD 2 (Fedegari)
	VX-150 (Systec)
Water purification system	Ion separator GENO-sep (Grünbeck)
	Ultrafiltration module (membraPure)
Centrifuges	Biofuge stratos (Heraeus)
	Centrifuge 5415 B (Eppendorf)
	Centrifuge 5415 R (Eppendorf)
	Centrikon T-124 (Kontron)
	RC2-B (Sorvall)
Concentrator	Stirred ultrafiltration cell (Millipore)
Cuvettes	Quartz precision cells (Hellma)
Digital cameras	Coolpix 995 (Nikon)
	EC 3 (Leica)
Fluorescence spectroscopy	Fluoromax4 spectrofluorometer (HORIBA)
	Liquid Nitrogen Dewar Assembly (HORIBA)
FPLC	Äkta™ Purifier (GE Healthcare)
French pressure cell press	PP60KN (Watz Hydraulik)
Gel apparatuses	Agarose gel chamber (JLU Giessen)
	Mini-PROTEAN Tetra Cell (Biorad)
Heating block	Driblock DB-3 (Techne)
	Thermomixer comfort (Eppendorf)
Incubator	B 5042 (Heraeus)
IR equipment	IR LED (λ_{max} = 940 ± 45 nm; Roithner Optics)
	CCD video camera (#190974; Conrad Electronic)

	HMV display (3-Scope; Trivisio Prototyping)
Light sources	LEDs (Roithner)
	PRADO Universal (Leitz)
Microscopes	B061 (Olympus)
	SZ60 (Olympus)
	MZ 8 (Leica)
	S8 APO (Leica)
	Z16 APO A (Leica)
Optical filters	Interference filters (Schott)
	Cut-off filters (Schott)
pH meter	inoLab pH level 1 (wtw)
Pipetting robots	Cartesian™ Dispensing System (Genomic solutions)
	Liquid Handling Sampling Robot (Zinsser Analytic)
Rotary evaporator	Rotavapor-RE (Büchl)
Scales	AJ50L (Mettler)
	PJ400 (Mettler)
	PL1200 (Mettler)
Shaker	TR-125 (Infors HT)
	CERTOMAT® HK (Sartorius)
	CERTOMAT® R (Sartorius)
UV-Vis spectroscopy	8453 detector-array spectrophotometer (Agilent)
	Microspectrophotometer (ESRF)
	Microspectrophotometer (Marburg)
	UVmini-1240 (Shimadzu)
Water bath	1002 (GFL)
	1083 (GFL)

2.1.2. Consumables

Column material	Ni-NTA Superflow (Qiagen)
Columns (prepacked)	HisTrap FF 1 & 5 ml (GE)
	HisTrap HP 1 & 5 ml (GE)
	Sep-Pak Plus C18 cartridges (Waters)
	Superdex 200 16/60 prep grade (GE)
	Superdex 200 26/60 prep grade (GE)
	UltraSep ES PHARM RP18E (Sepserv)
Cover slips	Ø 18 mm (Glaswarenfabrik Karl Hecht KG)
	Ø 22 mm (Hampton Research)
Crystallisation accessories	96-well plates (Greiner Bio-one)
	CrystalCap HT (Hampton Research)
	Nunclon™ Surface (NUNC)
	SWISSCI MRC 2 Well plates (Jena Bioscience)
	Baysilone paste (GE, Bayer)
Filter devices	Amicon Ultrafree-MC (Millipore)
	Filtropur S 0.2 (Sarstedt)
Membrane filters	YM10 (Millipore)
	YM30 (Millipore)
Single-use cuvettes	Polystyrene cuvettes (Sarstedt)

2.1.3. Chemicals

Chemicals used were purchased from Applichem, Merck and Sigma-Aldrich respectively. The following crystallisation kits were used for initial screening:

- NeXtal suites (Qiagen): AMS, anions, classics, classics lite, classics II, cryos, MbClass, MbClass II and PACT
- Sigma kits (Sigma-Aldrich): basic, cryo, extension and low ionic strength

2.1.4. Buffers and solutions

Media used for plasmid transformation:

SOC-medium

0.5 % (w/v) yeast extract
2 % (w/v) tryptone
10 mM NaCl
2.5 mM KCl
10 mM $MgCl_2$
20 mM $MgSO_4$
20 mM glucose
Sterile filtered

LB Medium

1 % (w/v) tryptone
0.5 % (w/v) yeast extract
1 % (w/v) NaCl
Adjusted to pH 7.3 with NaOH
Autoclaved

LB Agar plates

1.5 % agar in LB medium
Respective antibiotics

Media and solutions used for protein production:

M9-medium

1x M9-salts
0.4 % (w/v) glucose
1.4 % (v/v) amino acid mixture
0.2 % (v/v) M9-minerals
Sterile filtered

5x M9-salts

0.2 M Na_2HPO_4
0.1 M KH_2PO_4
0.04 M NaCl
0.09 M NH_4Cl
Sterile filtered

M9-minerals

0.5 M $MgSO_4$
0.08 mM $Fe(II)SO_4 \cdot 7H_2O$
0.05 % (w/v) thiamine
Sterile filtered

amino acid mixture

0.7 % (w/v) L-lysine
0.7 % (w/v) L-threonine
0.7% (w/v) L-phenylalanine
0.35 % (w/v) L-valine

0.35 % (w/v) L-leucine

0.35 % (w/v) L-isoleucine

Sterile filtered

Buffers used for protein purification:

TES-β

50 mM Tris

300 mM NaCl

5 mM EDTA

1 mM β-mercaptoethanol

Adjusted to pH 7.8 with HCl

Sterile filtered and degassed

K_nPO_4 buffer (pH 7.0)

61.5 % (v/v) 100 mM K_2HPO_4

38.5 % (v/v) 100 mM KH_2PO_4

5 mM EDTA

$TISI^{10}$-β

50 mM Tris

300 mM NaCl

1 mM IDA

10 mM Imidazole

1 mM β-mercaptoethanol

Adjusted to pH 7.8 with HCl

Sterile filtered and degassed

$TISI^{250}$-β

50 mM Tris

300 mM NaCl

1 mM IDA

250 mM Imidazole

1 mM β-mercaptoethanol

Adjusted to pH 7.8 with HCl

Sterile filtered and degassed

Buffer used for protein precipitation:

AMS

50 mM Tris

1 mM IDA

3.3 M $(NH_4)_2SO_4$

Adjusted to pH 7.8 with HCl

Sterile filtered

Buffer used for protein crystallisation:

TS/20

2.5 mM Tris

15 mM NaCl

Adjusted to pH 7.8 with HCl

Sterile filtered

Buffers and solutions used for SDS-PAGE:

4x stacking gel buffer

0.5 M Tris

0.6 % (w/v) SDS

Adjusted to pH 6.8 with HCl

4x resolving gel buffer

1.5 M Tris

0.6 % (w/v) SDS

Adjusted to pH 8.8 with HCl

Acrylamide solution (30 %)

30 % (v/v) acrylamide 4K solution

37.5 : 1 (acrylamide: bisacrylamide)

Stacking gel

1.2 ml H_2O

0.5 ml 4x stacking gel buffer

0.26 ml acrylamide (30 %)

30 µl APS (10 % (v/v))

5 µl TEMED

Resolving gel (12 %)

2.1 ml H_2O

1.5 ml 4x resolving gel buffer

2.4 ml acyrlamide (30 %)

50 µl APS (10 % (v/v))

10 µl TEMED

SDS electrophoresis buffer

25 mM Tris Base

0.2 M Glycine

1 % (w/v) SDS

6x SDS loading buffer

67 % (v/v) 4x stacking gel buffer

30 % (v/v) glycerol

1 % (w/v) SDS

0.5 M DTT

0.09 % (w/v) bromphenol blue

1 % (v/v) β-mercaptoethanol

Solutions used for Coomassie staining:

Coomassie staining solution

0.5 % (w/v) Coomassie R250

25 % (v/v) isopropanol

10 % (v/v) acetic acid

Destaining solution

10 % (v/v) acetic acid

2.1.5. Strains and plasmids

For the production of Cph1Δ2 as apoprotein the plasmid p926.5 (Figure 6), created by Jon Hughes, was transformed in chemically competent BL21 (DE3) *E. coli* (genotype: *ompT, hsdS (rB- mB-), gal, dcm, F-, λ (DE3)*) harboring the plasmid pSE111. p926.5 is based on a pQE12 vector (Qiagen), which contains the gene for Cph1Δ2 production, comprising the first 514 amino acids of Cph1 followed by a histidine tag (6xHis) and a gene for ampicillin resistance. p926.5 has a ColE1 origin of replication and uses a T5 promoter / lac operator element for the expression of Cph1Δ2. The plasmid pSE111 (58) has a p15A origin of replication and includes a gene for the production of a rare arginine tRNA *argU*, a gene for kanamycin resistance and a $lacI^Q$ gene for the overexpression of the lac repressor.

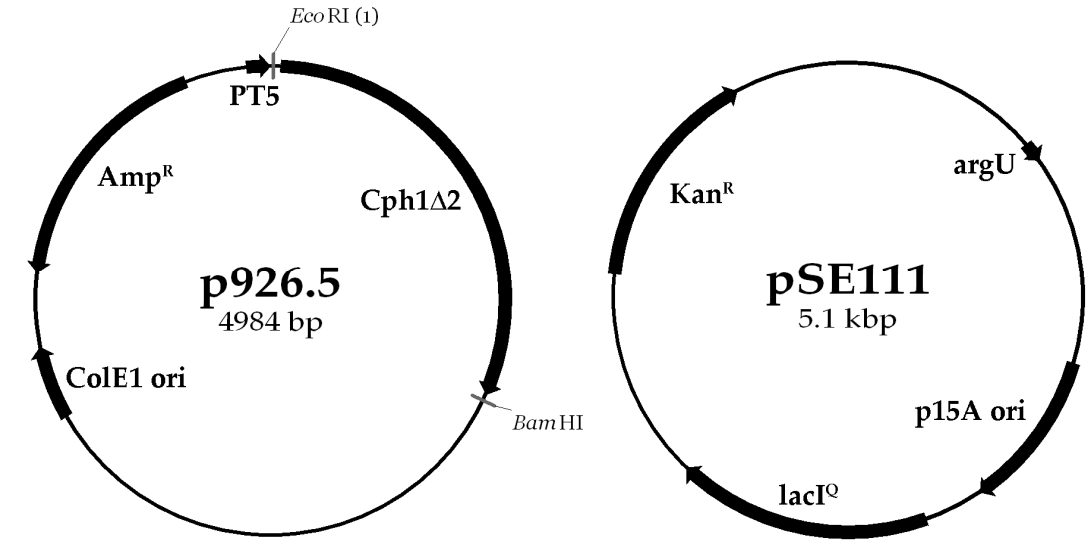

Figure 6: Plasmids p926.5 and pSE111 used for apophytochrome production.

For the production of Cph1Δ2 as holoprotein the plasmids p83 and p171 (Figure 7), were transformed in chemically competent BL21PRO *E. coli* (*ompT, hsdS_B (rB- mB-), gal, dcm, F-*). p83 is based on a pPROLar.A122 vector (Clontech), which contains the gene for Cph1Δ2 production, comprising the first 514 amino acids of Cph1 followed by a histidine tag (6xHis) and a gene for kanamycin resistance. p83 has a p15A origin of replication and uses a lac / ara hybrid promoter for the expression of Cph1Δ2. The plasmid p171 is based on a pQE12 vector (Qiagen) and includes two *Synechocystis* genes, the heme oxygenase *ho* and the ferredoxin

oxidoreductase *pcyA* for the synthesis of PCB from heme. p171 has a ColE1 origin of replication and uses a T5 promoter / lac operator element for the expression of *ho* and *pcyA*. Depending on the plasmids used, the media described above were supplied with the following antibiotics concentrations:

p926.5: ampicillin (100 mg / ml) with a final concentration of 0.1 mg /ml

p83 & p171: ampicillin (100 mg / ml) and kanamycin (50 mg / ml) with final concentrations of 0.1 and 0.05 mg / ml respectively.

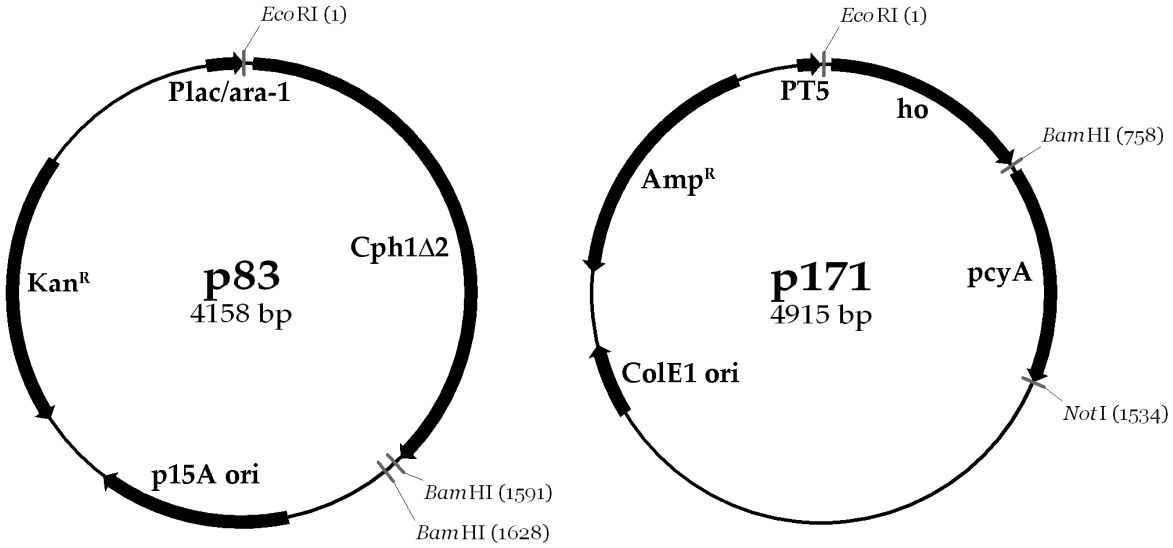

Figure 7: Plasmids p83 and p171 used for holophytochrome production.

2.2. Methods

2.2.1. Generation of site-directed mutants

Site directed mutants of Cph1 2 were generated by Dr. Georgios Psakis, using the "round the horn" PCR based method (59), in which back to back phosphorylated primer pairs, carrying the mismatch of interest, were used to amplify the complete p83 and / or p926.5 plasmids. PCR amplified products were DpnI (NEB) treated for the removal of methylated or hemi-methylated parental plasmid DNA. Self ligations of the constructed plasmids were catalysed

by T4-DNA ligase (NEB) in the presence of 0.5 mM ATP at 16 °C and for a maximum of 6 hours, prior to transformation with the bacterial strain of interest.

2.2.2. Transformation of *E. coli*

For the chemical transformation of plasmids needed for apophytochrome production, 0.1 µl of p926.5 (100 ng / µl) was transferred into 100 µl of chemically competent BL21 (DE3) *E. coli* containing pSE111 and incubated for 30 minutes on ice. The mixture was then put in a 42 °C water bath for 90 s. 600 µl SOC medium was added and the mixture was incubated at 37 °C at 150 rpm for 1 h. After incubation, the cells were centrifuged for 3 minutes at 4500 g, 550 µl of the supernatant was discarded and the rest was mixed and evenly distributed on a LB agar plate. The plates were incubated overnight (~ 16 h) at 37 °C.

For the chemical transformation of plasmids needed for holophytochrome production, 0.4 µl of p83 (or the respective plasmid carrying a site-directed mutation in the Cph1Δ2 gene) and 0.2 µl of p171 (stock concentrations at 100 ng / µl) were transferred into 100 µl of chemically competent BL21PRO *E. coli* and the same procedure as described above followed.

2.2.3. Production of phytochrome

Pre-culture

A colony of *E. coli* carrying the plasmids for phytochrome production taken from an overnight grown agar plate or alternatively a small amount of *E. coli* from a glycerol stock of a pre-culture was transferred into a 250 ml flask containing 50 ml autoclaved LB medium and the respective antibiotics. The culture was shaken at 150 rpm and grown for 16 hours at 37 °C. 250 µl of the pre-culture was transferred into 500 µl glycerol, gently and thoroughly mixed, shock-frozen in liquid nitrogen and stored at -80 °C.

Production of phytochrome in LB medium

15 % of the pre-culture was transferred to a 2 l flask containing 750 ml autoclaved LB medium and the respective antibiotics. The culture was shaken at 150 rpm and grown at 37 °C until an OD_{600} of 0.4 was reached. The culture was cooled down to 4 °C in an ice / water bath. 0.2 %

arabinose and 1 mM IPTG or 50 µM IPTG were added for holo- or apophytochrome production, respectively. The culture was put at 18 °C in darkness and shaken for 20 h at 150 rpm.

Production of phytochrome in M9-medium

To remove any remains of LB medium, the 15 % of the pre-culture was centrifuged for 3 minutes at 1300 g and 4 °C. The supernatant was removed and the pellet was resuspended in 7.5 ml M9-medium. The resuspended cells were transferred to a 2 l flask containing 750 ml M9-medium with the respective antibiotics. The culture was shaken at 150 rpm and grown at 37 °C until an OD_{600} of 0.4 was reached. The culture was cooled down to 4 °C in an ice / water bath. 37.5 mg (dissolved in 1 ml H_2O) L-selenomethionine, 0.2 % arabinose and 1 mM IPTG were added for holophytochrome production. The culture was put at 18 °C in darkness and shaken for 20 h at 150 rpm.

Cell harvest and protein isolation

After 20 h of incubation at 18 °C, the cells were harvested by centrifugation at 6000 g for 15 minutes at 4 °C. The supernatant was discarded and the pellet was resuspended in TES-β and centrifuged at 5000 g for 15 minutes at 4 °C to remove any remains of the medium. The supernatant was discarded and the pellet was resuspended in TES-β. The cells were cracked using a cooled French pressure cell with a force of ~ 21500 N. This step was repeated twice in total for complete cell disintegration. Clarification was done at 50000 g for 30 minutes at 4 °C. The supernatant was precipitated with AMS at 2:3 volumes and stored at 4 °C for at least 2 h before affinity chromatography.

2.2.4. Purification by affinity chromatography

The AMS-precipitated protein was centrifuged at 5000 g for 30 minutes at 4 °C. The supernatant was discarded and the pellet was centrifuged additional 10 minutes to remove any remaining liquid. The pellet was resuspended in $TISI^{10}$-β and centrifuged at 50000 g for 20 minutes at 4 °C. The supernatant was used for Ni-NTA affinity chromatography.

Depending on the yield of phytochrome determined by UV-Vis spectroscopy (section 2.2.7.), an affinity column containing a total volume of 1 to 5 ml of Ni-NTA material was used. The respective column was connected to an Äkta™ Purifier (GE Healthcare) and equilibrated in subsequent steps with filtered and degassed Milli-Q and TISI^{10}-β. The clarified supernatant was injected via a 10 ml superloop into the column. The chromatography was monitored at 280 nm (which accounts for all proteins) and at λ_{max} of phytochrome or the respective mutant. The column was washed with 20 – 30 column volumes (cv) of TISI^{10}-β to remove any unbound protein. The bound protein was eluted from the column by a linear concentration gradient of imidazole, using TISI^{10}-β and TISI^{250}-β and collected in 1 ml fractions. Phytochrome typically eluted at a concentration of 100 – 120 mM imidazole. To remove any remaining protein from the column, a washing step of 5 cv of TISI^{250}-β was carried out. The column was further washed with 3 cv of Milli-Q and stored in 20 % (v/v) ethanol at 4 °C.
Fractions containing phytochrome (determined in the chromatogram by absorbance at λ_{max}) were pooled and the protein yield was determined by UV-Vis spectroscopy (section 2.2.7.). The eluted phytochrome was precipitated with AMS at 2:3 volumes and stored at 4 °C for at least 2 h before the next purification step.

2.2.5. Apophytochrome assembly with PCB

Preparation of PCB was essentially done by Christina Lang as described for ^{13}C- and ^{15}N-labeled PCB (60). *Spirulina* algae pellets (greenValley®) were dissolved in cold K_nPO_4 buffer pH 7.0 and after clarification for 15 minutes at 5000 g at 4 °C the supernatant was precipitated with AMS at 1:3 volumes and stored in darkness at 4 °C for 16 h. The precipitate was centrifuged for 15 minutes at 5000 g at 4 °C in subdued light and the pellet was resuspended and washed with cold methanol until the supernatant was clear and colourless. The pellet was resuspended in cold methanol and methanolysed at 54 °C in darkness under constant stirring for 16 h. After clarification for 15 minutes at 5000 g at 4 °C the supernatant was concentrated in a rotary evaporator, pre-purified manually via Sep-Pak Plus C18 cartridges and finally purified via HPLC using a UltraSep ES PHARM RP18E with a 18 ml pre-column at a flow rate of 6 ml / min and 4.2 MPa, using a running buffer with 70 % 7.5 mM $NaPO_4$ (pH 6.0) and

30% acetonitrile. After HPLC the solvent was exchanged via a C18- cartridge into methanol and the purified PCB was concentrated to ~ 1 mM by evaporation and stored in darkness at -80 °C.

For assembly with apophytochrome, PCB was dissolved in TES-β by ultrasonication. Three times molar excess of PCB was added to Ni-NTA-purified apophytochrome in TES-β for complete autocatalytic *in vitro* assembly in darkness at 4 °C overnight.

2.2.6. Size exclusion chromatography

Preparative gel filtration

Overnight *in vitro* assembled holophytochrome was concentrated to a volume of 5 ml and clarified by hard centrifugation for 20 minutes at 50000 g at 4 °C. Precipitated *in vivo* assembled holophytochrome was centrifuged at 5000 g for 30 minutes at 4 °C. The supernatant was discarded and the pellet was centrifuged an additional 10 minutes to remove any remaining liquid. The pellet was resuspended in TES-β in a total volume of 5 ml and centrifuged at 50000 g for 20 minutes at 4 °C. The supernatant was used for preparative gel filtration.

Size exclusion chromatography using a Superdex 200 26/60 prep grade column (V_t = 318 ml, V_0 = 105 ml) connected to the Äkta™ Purifier was performed essentially as described (61). Samples with typical concentrations varying between 5 and 10 mg / ml were irradiated in 250 µl steps with saturating FR prior to injection into the column via a 10 ml superloop. The whole procedure was carried out in darkness using safelight (λ_{max} = 490 ± 20 nm) to avoid photoconversion. The chromatography was run at 2 ml / min with TES-β as running buffer and monitored at 280 nm (which accounts for all proteins) and at λ_{max} in the red region, where phytochrome or the respective mutant absorbs. Eluted fractions containing monodisperse phytochrome were pooled and stored at 4 °C.

Analytical gel filtration

Although the Superdex 200 16/60 prep grade column (V_t = 120.6 ml, V_0 = 39.8 ml) is not suited for precise and detailed analysis of the quaternary structure of proteins, this method

allows to distinguish between phytochrome monomers and dimers as described (61). Samples with a concentration varying between 1 and 5 mg / ml in a total volume of 1 ml were irradiated in 250 µl steps with saturating R prior to injection into the column via a 1 ml superloop. To avoid photoconversion, IR visualisation equipment was used (62) and samples as well as the eluting fractions were handled in complete darkness. The chromatography was run at 1 ml / min and monitored at λ_{max} and λ_{ibp} in the red region of phytochrome absorbance and at 700 nm, where mostly Pfr absorbs. Eluted fractions were discriminated between and pooled as monomer and dimer respectively and their photochemical state was determined by UV-Vis spectroscopy.

2.2.7. Protein concentration

Following polishing by size exclusion chromatography, monodisperse phytochrome was concentrated to 10 mg / ml (≈ 0.17 mM) using a stirred ultrafiltration cell. For crystallisation, the buffer was exchanged from TES-β to TS/20 by concentrating the protein to a volume of 1 ml and adding 9 ml of TS/20. This procedure was repeated three times to effectively change the buffer.

2.2.8. SDS-PAGE

20 µl of Cph1Δ2 and its respective mutants at a concentration of 0.4 mg / ml were mixed with 4 µl of 6x SDS loading buffer and incubated for 5 minutes at 95 °C. After clarification at 4500 g for 5 minutes, 10 µl of the supernatant was pipetted into a lane of a 12 % SDS gel. The gel was run at 0.2 mA until the dye front reached the end of the gel. The gel was thereafter cleaned with water, incubated for 15 minutes in 1 mM zinc acetate, washed with water and photographed under UV light to confirm covalent attachment of the PCB chromophore to phytochrome (63). Subsequent Coomassie staining revealed all protein bands under white light.

2.2.9. UV-Vis spectroscopy

Absorbance spectra of phytochrome in solution were recorded in a quartz cuvette on a modified Agilent 8453 UV–Vis diode detector-array spectrophotometer (57). The modification regards the cuvette holder, which allows the sample to be irradiated either by saturating FR or R, respectively. Narrower slits in the measuring pathway minimize scattering effects. Absorbance spectra of phytochrome were taken after FR and R irradiation, respectively.

The determination of the quantum yield of phototransformation (Φ_P) was done using an UVmini-1240 spectrophotometer (Shimadzu). The Pr → Pfr photoconversion was monitored at λ_{max} of the Pfr state to measure the increase of the Pfr fraction by irradiating the sample at their respective Pr λ_{max} (fluence rates: 6.7 – 7.9 $\mu mol \cdot m^{-2} \cdot s^{-1}$) using appropriate interference filters (wildtype: λ = 660 nm, T_{max} = 37 %, FWHM = 16 nm; Y263F: λ = 651 nm, T_{max} = 45 %, FWHM = 13 nm; Y263H / Y263S: λ = 643 nm, T_{max} = 41 % FWHM = 10 nm; Schott). The photoconversion rate constant k and the quantum efficiency of photoconversion Φ_P were determined based on the equations of Butler et al. and Pratt (47, 64), integrating with respect to wavelength from 620 nm to 680 nm to account for the spectral distributions of the light sources measured with a spectroradiometer (Ocean Optics) (40):

$$\Phi_P(Pr \rightarrow Pfr) = \frac{k \cdot \chi_{Pfr,\,max}}{\int_{620}^{680} I(\lambda) \cdot \varepsilon_{Pr}(\lambda) d\lambda} \quad \text{, where}$$

k = photoconversion rate constant

$\chi_{Pfr,\,max}$ = maximum mole fraction of Pfr at photoequilibrium

I = actinic quantum fluence rate

ε_{Pr} = molar extinction coefficient after FR irradiation

The photoconversion rate constant k is determined by extrapolating the initial slope of the resulting curves of phototransformation using the following equation:

$$k \cdot t = -\log \Delta P \text{ , where } \Delta P \text{ is the proportion of phytochrome converted (64)}$$

The measuring light did not induce significant photoconversion relative to the actinic source. To determine the quantum yield for the reverse reaction Φ_P (Pfr → Pr), the following relation (47, 64) was used:

$$\Phi_P(\mathrm{Pfr} \rightarrow \mathrm{Pr}) = \frac{\Phi_P(\mathrm{Pr} \rightarrow \mathrm{Pfr})}{(\frac{A_{min}}{A_{max}} \cdot \frac{1}{\chi_{Pr,max}}) - 1}$$, where

A_{min} = absorbance at λ_{max} (Pr) at photoequilibrium

A_{max} = absorbance at λ_{max} (Pr) after FR

$\chi_{Pr,\,max}$ = Pr fraction at photoequilibrium

2.2.10. Protein quantification

The extinction coefficient (in the red region) of phytochrome was determined by measuring the absorbance of the samples in equal concentrations in TES-β and in 8 M Urea pH 2.0 (under unfolding conditions) at their respective λ_{max}. With the known extinction coefficient at 662 nm (λ_{max}) of phycocyanin of 35.5 $mM^{-1} \cdot cm^{-1}$ in acidic buffer (65) and assuming that only assembled holophytochrome absorbs in the red region and hence $c_{Phy} = c_{PCB}$, the extinction coefficient of the mutants were determined according to the formula:

$$\varepsilon_{Phy,\lambda_{max,red}} = \frac{A_{Phy,\lambda_{max,red}} \cdot \varepsilon_{PCB}}{A_{PCB}}$$, where

c = concentration of the sample

A = absorbance at λ_{max} in the red region

ε = molar extinction coefficient

After determination of the extinction coefficient, the phytochrome concentration was calculated:

$$c_{Phy} = \frac{A_{Phy,\lambda_{max,red}} \cdot M_w}{\varepsilon_{Phy,\lambda_{max,red}}}, \text{ where}$$

c = concentration of the sample

A = absorbance at λ_{max} in the red region

ε = molar extinction coefficient

M_w = molecular weight (g / mol)

Knowing the concentration of a specific sample and its spectra after FR and R irradiation, the amount of phytochrome in impure samples was determined through the difference spectrum (FR - R):

$$\Delta\Delta A = \Delta A_{max} - \Delta A_{min} \Rightarrow c_{Phy} = a \cdot \Delta\Delta A \text{ , where}$$

ΔΔA = 2nd order difference

ΔA_{max} = maximum of the difference spectrum

ΔA_{min} = minimum of the difference spectrum

c = concentration of the sample

a = specific constant (= 1 for wt Cph1Δ2)

Furthermore, knowing both the extinction coefficient at 280 nm and at λ_{max}, the theoretical specific absorbance ratio (SAR) was calculated to determine the purity of phytochrome samples:

$$SAR_{theor} = \frac{\varepsilon_{\lambda_{max,red}}}{\varepsilon_{280}} \quad \text{and} \quad SAR_{meas} = \frac{A_{\lambda_{max,red}}}{A_{280}}, \text{ where}$$

SAR_{theor} = theoretical SAR

SAR_{meas} = measured SAR

The extinction coefficient at 280 nm comprises the extinction coefficient of phytochrome (Cph1Δ2 ≈ 58 $mM^{-1} \cdot cm^{-1}$) and PCB (≈ 3.5 $mM^{-1} \cdot cm^{-1}$). The purity of the samples was determined by the ratio of SAR_{meas} to SAR_{theor}.

2.2.11. Fluorescence spectroscopy

Fluorescence spectra and kinetics were recorded using a Fluoromax4 spectrofluorometer (HORIBA Jobin Yvon). To minimize spectral artefacts deriving from self-absorption and scattering a protein concentration of approximately 0.1 mg / ml was used. Emission spectra were measured using an excitation wavelength of 610 nm, a slit bandwidth of 0.3 nm and a red interference filter (λ_{max} = 610 nm, T_{max} = 40 %) to minimise phytochrome photoconversion during the scan. To exclude possible interference of scattered exciting light with the fluorescence spectra measurements, a 600 nm cut-off filter was used and the spectra were recorded from 630 to 750 nm with slit bandwidth of 10 nm and an integration time of 0.1 s. The low protein concentration and the reduced integration time necessitated three separate scans, which were then averaged and smoothed (by adjacent averaging method) for the final emission spectrum.

To determine the fluorescence quantum yield (Φ_F), chlorophyll a (Chla) with a defined Φ_F = 0.3 was used as a reference (66) together with the following formula:

$$\Phi_F^x = \frac{F^x}{F^{Chla}} \cdot \frac{(1-T)^{Chla} \cdot \Phi_F^{Chla}}{(1-T)^x}, \text{ where}$$

x = sample

F = fluorescence

T = transmittance

The fluorescence F is determined by integrating the emission spectrum from 630 to 750 nm.

Excitation spectra were recorded from 580 – 700 nm and 350 – 700 nm with a slit bandwidth of 1 nm and using a 1 % grey transmission filter to minimize photoconversion. The emission was measured at 720 nm with a slit bandwidth of 10 nm and using a 680 nm cut-off filter to avoid interference from scattered light. The integration time was 0.1 s and excitation spectra were averaged and smoothed (by adjacent averaging method) from 3 measurements.

To determine Φ_P (Pr → Pfr) by fluorescence spectroscopy, a kinetic measurement was done with excitation light at the respective λ_{max} (fluence rate ~ 5 µmol · m^{-2} · s^{-1}), with slit bandwidth of 10 nm to irradiate the whole sample, a 0.2 % transmission grey filter and an integration

time of 0.1 s. It was assumed that only the Pr state of the investigated samples is fluorescent. Emission was recorded for 600 s at 720 nm, slit bandwidth of 10 nm and a cut-off filter of 680 nm. The resulting initial slope of the curve determines the rate constant of photoconversion and with the known Φ_P of Cph1Δ2 = 0.13, which was determined independently by absorbance spectroscopy (section 2.2.7.), Φ_P of the samples can be calculated using the following formula:

$$\Phi_P^x(Pr \rightarrow Pfr) = \frac{k^x \cdot \int_{620}^{680} I(\lambda) \cdot \varepsilon_{Pr}(\lambda) d\lambda \cdot \Phi_P(Pr \rightarrow Pfr)}{k \cdot \int_{620}^{680} I^x(\lambda) \cdot \varepsilon_{Pr}^x(\lambda) d\lambda}, \text{ where}$$

k = photoconversion rate constant

I = actinic quantum fluence rate

ε_{Pr} = molar extinction coefficient after FR irradiation

x = samples with unknown Φ_P

Low temperature fluorescence measurements were performed in a quartz tube placed in a Dewar flask (HORIBA Jobin Yvon), coated with a mixture of 50% glycerol and 50% ethanol to avoid condensation on the outer surface of the Dewar. The samples were irradiated with saturating FR before being submerged in liquid nitrogen. Upon thawing, either fluorescence spectra (for the determination of λ_{max} shift) or single wavelength measurements at λ_{max} of the emission at 85 K (for the determination of activation energies Ea) were taken in 10 or 20 K steps respectively. Emission spectra were essentially recorded as mentioned above using excitation slit bandwidth of 1 nm and emission slit bandwidth of 5 nm. Temperature was monitored using a thermocouple. The Φ_F at 85 K was determined as shown above for ambient temperatures (T_a) by using Φ_F of the respective protein at T_a and equal concentrations as reference. The determination of the fluorescence decay activation energies (Ea) were determined as described (45) by linearization of the temperature-dependent fluorescence measurements in Arrhenius coordinates:

$$y = \ln\left(\frac{1}{\Phi_F} - 1 - \frac{k_d}{k_f}\right) \text{ and } x = \frac{1}{T}, \text{ where}$$

k_d = rate constant of the temperature-independent excitation degradation

k_f = radiative rate constant

The ratio k_d / k_f was estimated from the fitting of the observed temperature-dependent fluorescence decay in Arrhenius coordinates. k_f was determined based on the theoretical oscillator strength f at λ_{max} (67):

$$k_f = 3 \cdot 10^{-9} \cdot \nu_{max}^2 \cdot \int \varepsilon_{\lambda_{max,red}} \cdot d\nu, \text{ where}$$

ν_{max} = energy corresponding to λ_{max} (cm^{-1})

ε = molar extinction coefficient of the Pr λ_{max}

$d\nu$ = energy corresponding to FWHM at λ_{max}

The radiative lifetime τ_0 was determined as reciprocal of k_f and the fluorescence lifetime τ_f was determined as the product of τ_0 and Φ_F. The rate constant of the temperature-dependent dissipation of excitation energy k_{p0} was calculated based on the following equation (45):

$$\Phi_F = \frac{k_f}{k_f + k_d + k_p} = \frac{k_f}{k_f + k_d + k_{p_0} \cdot e^{-\frac{Ea}{R \cdot T}}} \Leftrightarrow k_{p_0} = \frac{\frac{k_f}{\Phi_F} - k_f - k_d}{e^{-\frac{Ea}{R \cdot T}}}, \text{ where}$$

k_p = primary photoreaction (Pr → prelumi-R)

R = gas constant = 8.31 $J \cdot mol^{-1} \cdot K^{-1}$

T = temperature (K)

After determination of k_f, k_d and k_{p0}, the quantum yield of the primary photoreaction (= deactivation along the photochemical route) Φ_P (Pr → prelumi-R) was determined according to the following equation (45):

$$\Phi_P(Pr \rightarrow prelumi - R) = \frac{k_{p_0} \cdot e^{-\frac{Ea}{R \cdot T}}}{k_f + k_d + k_{p_0} \cdot e^{-\frac{Ea}{R \cdot T}}}$$

Finally, assuming that the Φ_P (Pr → Pfr) is the same as Φ_P (Pr → lumi-R), the quantum yield of phototransformation Φ_{ab} (prelumi-R → lumi-R) can be determined according to the following equation (45):

$$\Phi_{ab} = \frac{\Phi_P\,(Pr \rightarrow lumi - R)}{\Phi_P\,(Pr \rightarrow prelumi - R)}$$

2.2.12. Crystallisation

Initial crystallisation screens were carried out in darkness with phytochrome concentrations of 5 and 10 mg / ml and a drop size of 400 nl (200 nl protein + 200 nl reservoir solution) using the sitting-drop vapour-diffusion method in 96-well (Greiner Bio-one) and MRC (Jena Bioscience) plates. Crystallisation plates were stored at 291 K in complete darkness for 6 to 12 months with weekly observations under infrared (62) or blue-green light (490 ± 20 nm). Optimization was performed in 24-well plates (NUNC) with a 2 µl drop size (1 µl protein + 1 µl reservoir solution) using hanging-drop vapour diffusion by varying the pH of the buffer, the precipitant concentration and by exchanging the sodium ions for different monovalent or divalent cations. SeMet-labelled crystals were grown under essentially the same conditions as obtained for Cph1Δ2. Crystals were frozen in their respective reservoir buffer supplemented with 20 – 30 % glycerol or adequate cryo-salts (62, 68). Crystallisation and cryo-freezing conditions as well as optimizations of Cph1Δ2 and its mutants are described in detail in the results (section 3.4).

Diffraction patterns were recorded at beamlines X13, EMBL Hamburg, ID14-2 and ID14–3, ESRF Grenoble. To remove any remaining ice crystals and optimize diffraction, flash cryo-annealing in darkness was applied (62, 69). Spectra of crystallised Cph1Δ2 and its mutants were recorded at the cryobench in Marburg or at the ESRF (70), respectively. To attempt

photoconversion, crystals were irradiated with 532 nm (24 mW, NG-11010-110, JDS Uniphase) or 632 nm (10 mW, GLG 5410, NEC) lasers. The crystals were rotated for 5–10 s on the goniometer during illumination. The solved 3D structures of Cph1Δ2 and its mutants are presented in the results (section 3.4).

3. Results

3.1. Expression and purification

Expression of Cph1Δ2 in LB medium yielded ~ 30 mg / l of *in vivo* assembled protein of which approximately 70 % remained after Ni^{2+} affinity chromatography (Figure 8A) with an SAR of 1 – 1.2 (~ 90 % pure). At a concentration of ~ 5 mg / ml and saturated FR irradiation, *in vivo* assembled Cph1Δ2 eluted almost exclusively as a dimer in size exclusion chromatography (Figure 8B) and was ~ 100 % pure with an SAR of 1.3 – 1.4, its purity was further confirmed by SDS-PAGE (Figure 8C). Zinc acetate fluorescence showed that the chromophore was covalently bound to the protein and *in vivo* assembly was complete (Figure 8C). Purified Cph1Δ2 (Figure 8D) was concentrated to ~ 10 mg / ml for further handling. Expression of Cph1Δ2 in M9 medium containing selenomethionine yielded only ~ 10 mg / l of *in vivo* assembled protein, but purification proved similarly successful as for Cph1Δ2 produced in LB medium.

Expression of apo-Cph1Δ2 for *in vitro* assembly with PCB and production of almost all Cph1Δ2 mutations (assembled either *in vivo* or *in vitro*) in LB medium gave similar yields of ~ 30 mg / ml. Mutations of conserved histidines (H260Q, H260Y and H290F) and two tyrosines (Y198S, Y203E, Y203H and Y203N) within the chromophore pocket resulted in considerably lower amounts (max. 5 mg / l culture) of protein. Furthermore *in vivo* assembly for these specific mutants was incomplete and autocatalytic *in vitro* assembly with PCB to achieve higher amounts of holophytochrome was not successful. As shown before (57), expression of apo-H260Q proved unproblematic and gave similar protein yields as apo-Cph1Δ2. Although covalent attachment with PCB was possible, 100 % assembly could not be obtained reliably (Figure 9) and hence further characterisation of this particular mutant proved difficult. Zinc acetate staining performed on SDS-PAGE gels showed covalent attachment of PCB in all mutants (Figure 45 in appendix 11.1). In the case of Q27E, Y198S, D207N. D207S, D207R/R472D, R222A, R222K, H260Y, S272A, H290A, H290F, W450A and Q473S protein yields were too poor and purity too low for SDS-PAGE analysis. Nevertheless, it can be assumed that these mutants also attached PCB covalently to its cysteine as similar mutants or

mutations at the same position were analysed by SDS-PAGE and showed covalent linkage to Cys-259.

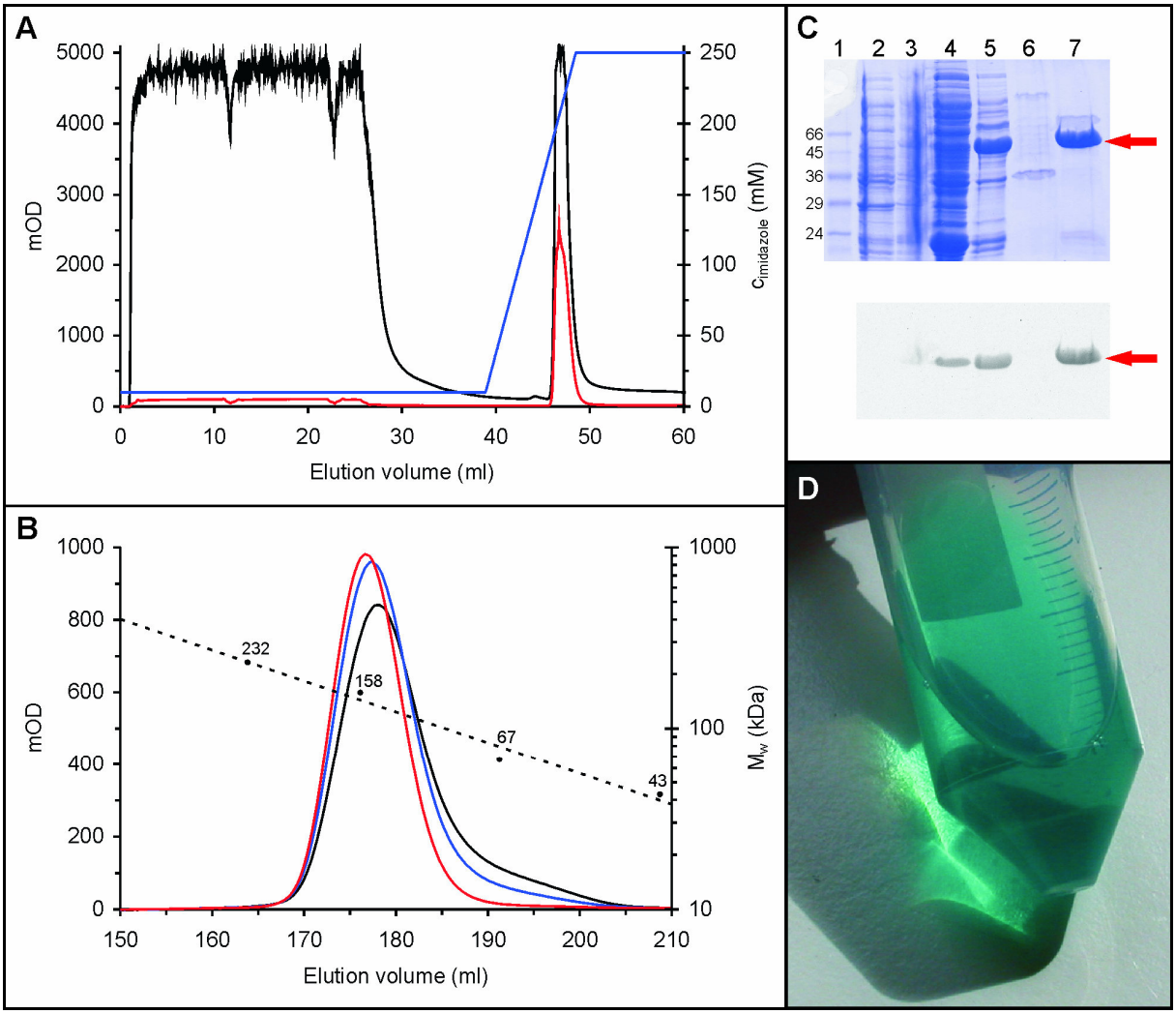

Figure 8: Purification of *in vivo* assembled Cph1Δ2.
(A) Ni^{2+} affinity chromatography of Cph1Δ2 monitored at 280 nm (black) and 660 (red) nm. The concentration of imidazole used for the elution of the bound protein is shown in blue. (B) SEC of Cph1Δ2 monitored at 280 nm (black) and $\lambda_{max, Pr}$ = 660 nm (red). The dotted line represents the column calibration with marker proteins (kDa). (C) SDS-gel showing Coomassie-stained proteins (above) and PCB-assembled Cph1Δ2 by zinc acetate fluorescence (below) before induction of Cph1Δ2 expression (2), after cell harvesting (3), after cell lysis (4), after Ni^{2+} affinity chromatography with the main eluate (5) and a contaminant (6) and after SEC (7). Molecular weight markers (kDa) are indicated in (1). The red arrows indicate the position of assembled Cph1Δ2. (D) Purified *in vivo* assembled Cph1Δ2 after SEC displays a blue-green colour.

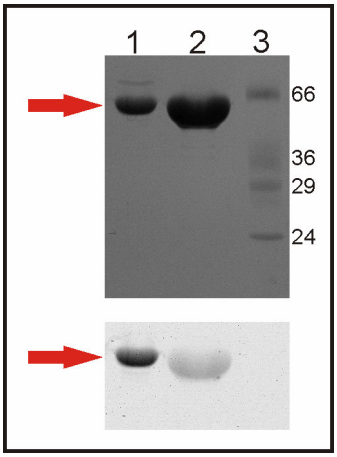

Figure 9: SDS-PAGE gel of H260Q.
Coomassie staining (above) and zinc acetate fluorescence (below) shows *in vivo* assembled Cph1Δ2 (1), *in vitro* assembled H260Q (2) and appropriate molecular weight markers in kDa (3). The red arrows indicate the position of the respective protein.

3.2. Spectroscopic analyses

3.2.1. UV-Vis spectra

In vivo assembled wild type Cph1Δ2 had its red maximum at 660 nm after FR irradiation. After saturating R irradiation a photoequilibrium was reached where 70 % of the phytochrome was in the Pfr state and 30 % remained in the Pr state (Figure 10 and Figure 46 – Figure 48 in appendix 11.2.1). The extinction coefficient ε (Pr λ_{max}) of the Cph1Δ2 Pr state at $\lambda_{max, red}$ was 85000 $M^{-1} \cdot cm^{-1}$ (Table 6 in appendix 11.2.2) as reported previously for the *in vitro* assembled full-length protein (71). However, $\lambda_{max, red}$ (Pr) of the *in vitro* assembled Cph1Δ2 was blue-shifted by 4 nm leading to a more prominent Pfr shoulder after FR irradiation. Still, the extent of phototransformation ($\chi_{Pfr, max}$) remained the same (Figure 46 – Figure 48 and Table 6 in appendix 11.2).

Only four of the investigated mutants (Q27E, K303A, G451A and Q473S) had almost identical spectral characteristics as wild type Cph1Δ2, showing only minor hypsochromic shifts (1 – 4 nm) of the Pr λ_{max} and λ_{soret}. ε (Pr λ_{max}), the oscillator ratio (relative absorbance strengths of the red and near UV (λ_{soret}) peaks) and $\chi_{Pfr, max}$ were almost unaffected (Figure 46, Figure 48 and Table 6 in appendix 11.2).

The UV-Vis spectra of most mutants (NTL Δ(1 – 20), S11A, Y203F, Y203W, L201Q, F216A, S251A, R254A, R254K, S272A, H290Q, G452A, Y458A, Y458S, E468A, R472A, F475H and

F475Y) were very similar to wild type Cph1Δ2. Interestingly, the Pr λ_{max} of S11A, Y203W and H290Q was red-shifted by ~ 3 nm leading to a higher extent of phototransformation ($\chi_{Pfr,\,max}$ = 0.75) and also a higher oscillator ratio (~3.4), although ε (Pr, $\lambda_{max,\,red}$) was reduced. The other mutants of this group had a blue-shifted Pr λ_{max} of 4 – 20 nm and a slightly reduced $\chi_{Pfr,\,max}$ between 0.6 and 0.7 (Figure 46 – Figure 48 and Table 6 in appendix 11.2). The oscillator ratio and ε (Pr, $\lambda_{max,\,red}$) of mutants within the chromophore pocket interacting directly or indirectly with the chromophore (L201Q, F216A, S251A, R254A, R254K, S272A, G452A, R472A, F475H and F475Y) was lower than for the wild type, implying a slight change in the chromophore status. As an example of this group of mutations, the spectra of S251A are shown (Figure 10).

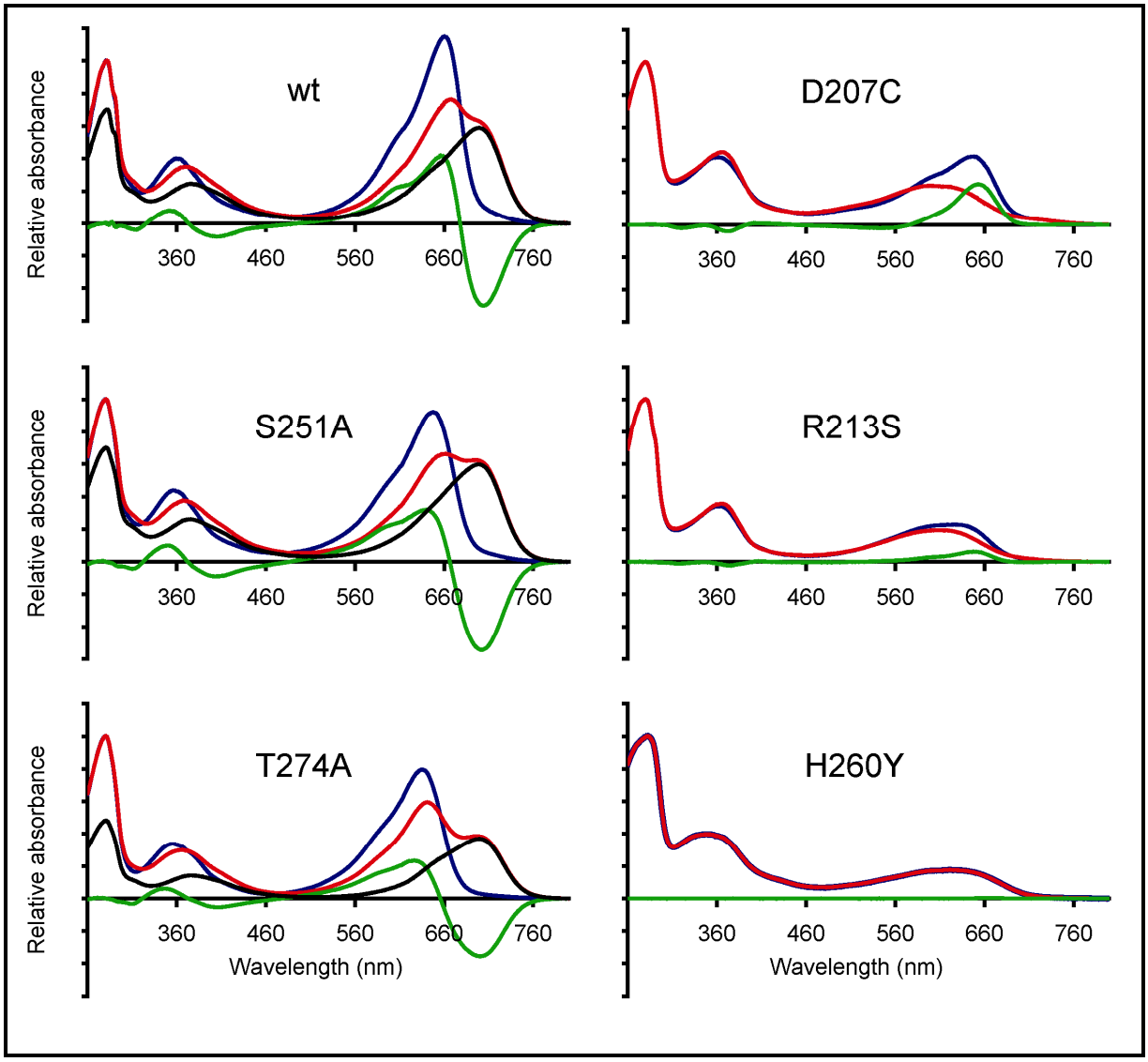

Figure 10: Absorbance spectra of wild type Cph1 and exemplary mutants.
The spectra were recorded after FR (blue) and R (red) irradiation. The resulting difference spectra are shown in green and the calculated Pfr spectrum (black) are based on the estimated $\chi_{Pfr,max}$ from Table 6.

Interestingly and in contrast to the wild type Cph1Δ2, $\lambda_{max, red}$ (Pr and Pfr) of *in vivo* assembled R254A was 5 nm blue-shifted when compared to the same, but *in vitro* assembled mutant. Furthermore, the oscillator ratio was reduced even more (1.6 vs. 2.1) and the FWHM was broader (54 vs. 46) suggesting that the chromophore PCB adopts different conformations in both cases. L201Q was of special interest since bathy-phytochromes, which possess a dark-adapted Pfr, have either a glutamine or an asparagine at position 188 (32, 72-77), implying that this residue is essential for Pfr stabilisation. Mutating the present leucine to a glutamine in Cph1Δ2 did not increase Pfr formation or induce dark reversion to 100 % Pfr occupancy as observed for bathy-phytochromes (Figure 46 and Table 6 in appendix 11.2). However, a slight increase in the Pfr proportion was observed after leaving the red irradiated sample in the dark for ~ 30 seconds leading to a 5 % increase of the calculated $\chi_{Pfr,max}$ (Figure 11).

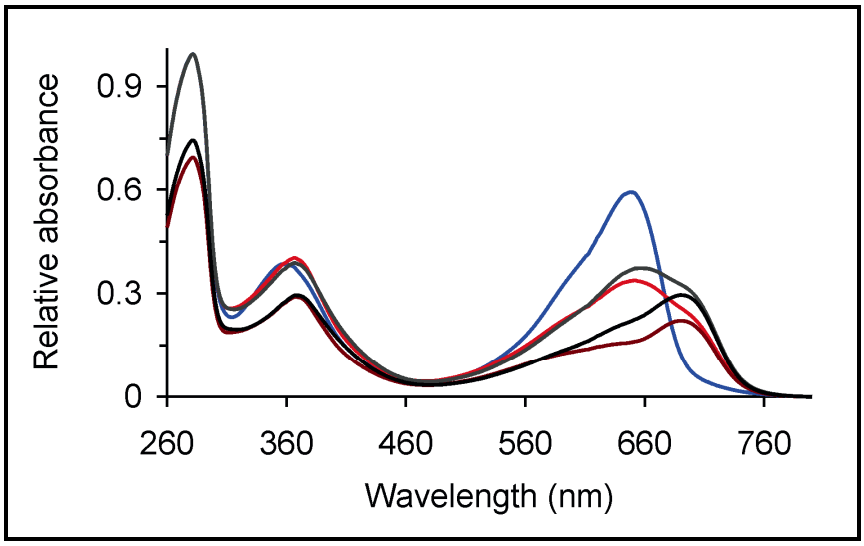

Figure 11: Absorbance spectra of L201Q.
Absorbance spectra of L201Q after FR (blue line) and R (red line) irradiation with the calculated Pfr spectrum (brown) based on the estimated $\chi_{Pfr,max}$ in Table 6. The dark adapted spectrum after initial R irradiation is shown in grey with its calculated Pfr spectrum in black.

T274A UV-Vis spectra (Figure 10) were representatively used for the group of mutants showing normal Pr characteristics but a reduced extent of phototransformation at photoequilibrium (R222A, R222K, H260Q, Y263F, Y263H, Y263S, T274A, W450A, F475A, W478F and tongue Δ(462 – 480)). The λ_{max} (Pr) was blue-shifted by 8 – 20 nm and the oscillator ratio as well as ε (Pr, $\lambda_{max, red}$) were reduced to 1.2 – 2.4 and 47000 – 80000 $M^{-1} \cdot cm^{-1}$ (with the exception of Y263F with a ratio = 2.8 and ε = 85000 $M^{-1} \cdot cm^{-1}$), respectively. The maximum mole fraction of Pfr present at photoequilibrium amounted to 0.46 – 0.65. $\chi_{Pfr, max}$

could not be estimated based on the spectra for the mutants R222A, R222K, H260Q, W478F and tongue Δ(462 – 480) due to the lack of a prominent Pfr shoulder at photoequilibrium.

Mutants showing a typical albeit reduced Pr peak and bleaching upon R irradiation without formation of a Pfr-like peak comprised D207C, D207N, D207S, H290A, P471G and S474A (Figure 10). Pr λ_{max} was blue-shifted by 10 – 14 nm. The oscillator ratio was considerably reduced (0.96 – 1.7), ε (Pr, $\lambda_{max, red}$) was more than halved (26000 – 37000 $M^{-1} \cdot cm^{-1}$) and $\chi_{Pfr, max}$ could not be determined based on the spectra. Earlier investigation of D207A revealed similar behaviour to that observed in the aforementioned group (57).

Y198S, Y203H, R213S and the double mutant D207R / R472D displayed an atypical spectrum after FR irradiation, with only a weak bump in the red region around 630 nm. Upon R irradiation, the ~ 630 nm bump disappeared without formation of a Pfr-like peak, as seen in the previous group of mutants. These mutants also proved difficult to purify, hence ε (Pr, $\lambda_{max, red}$) could not be determined, but based on the spectral characteristics was expected to be very low. The oscillator ratio was around 0.6 and thus almost five times lower than in the wild type. R213S was shown as an example of this group in Figure 10.

Y203N and H260Y did not show any change after FR or R irradiation respectively and displayed a bleached phenotype. λ_{max} was severely hypsochromic by 25 – 39 nm and the oscillator ratio was 0.4 – 0.6. H290F and Y176H constituted special cases. The former displayed a strong peak at 587 nm with weak shoulders at 550 and 640 nm, respectively, after FR irradiation. Photoconversion to a Pfr-like state with a peak arising around 700 nm was almost negligible after R irradiation and was not significantly increased by use of appropriate filters, leaving the ~ 70 nm blue-shift of the maximum in the red unaccounted for. The difference spectrum showed two red peaks at 590 and 650 nm, respectively. Y176H was also unable to undergo proper photoconversion. Although a strong Pr peak (ε = 69500 $M^{-1} \cdot cm^{-1}$) around 642 nm was observed after FR irradiation, subsequent bleaching and formation of a Pfr-like peak after R irradiation did not happen: the mutation seemed to lock the photoreceptor in its Pr state (50, 78).

3.2.2. Dark reversion

This work confirmed the dark reversion pattern of wild type Cph1Δ2 ($t_{½}$ > 15 days) previously observed (11) (Figure 12).

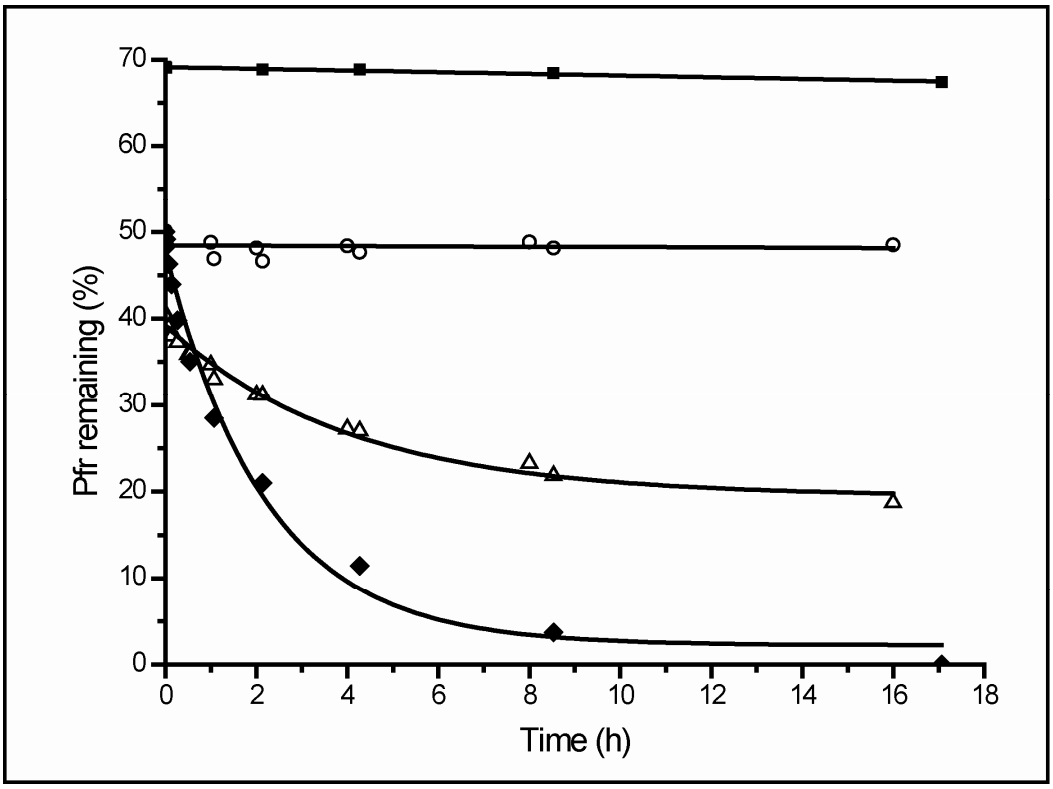

Figure 12: Dark reversion of Cph1Δ2 and the Y263 mutants.
Dark reversion curves of wild type Cph1Δ2 (▪), Y263F (○), Y263H (Δ) and Y263S (♦) are displayed as remaining Pfr over time.

Like wild type Cph1Δ2, R254A, Y263F (Figure 12) and T274A did not revert back to the Pr ground state in darkness. On the other hand, R254K and R472A showed slow dark reversion (10 – 15 % in 24 hours at 22 °C) and R222A and R222K showed increased dark reversion (20 – 40 % in 24 hours at 22 °C). Y263H and most notably Y263S reverted back to the Pr state in darkness at 22 °C with $t_{½}$ = 14 and 1.5 h, respectively (Figure 12) (79). Mutations of the conserved D207 to either A, C, N or S revealed dark reversions from the bleached Pbl state back to Pr with $t_{½}$ ~ 12 minutes (57).

3.2.3. Quantum yield of phototransformation

Phototransformation was studied in detail for wildtype Cph1Δ2 and mutants Y263F, Y263H and Y263S by absorbance and fluorescence spectroscopy (Figure 13) (79). Although the extinction coefficient and the extent of phototransformation for the wild type corresponded

closely to those published earlier (40, 71, 80), a slightly lower quantum yield of phototransformation was determined (Table 1). Φ_P (Pr → Pfr) and $\chi_{Pfr,\ max}$ determined independently by absorbance and fluorescence spectroscopy gave identical results for wild type Cph1Δ2.

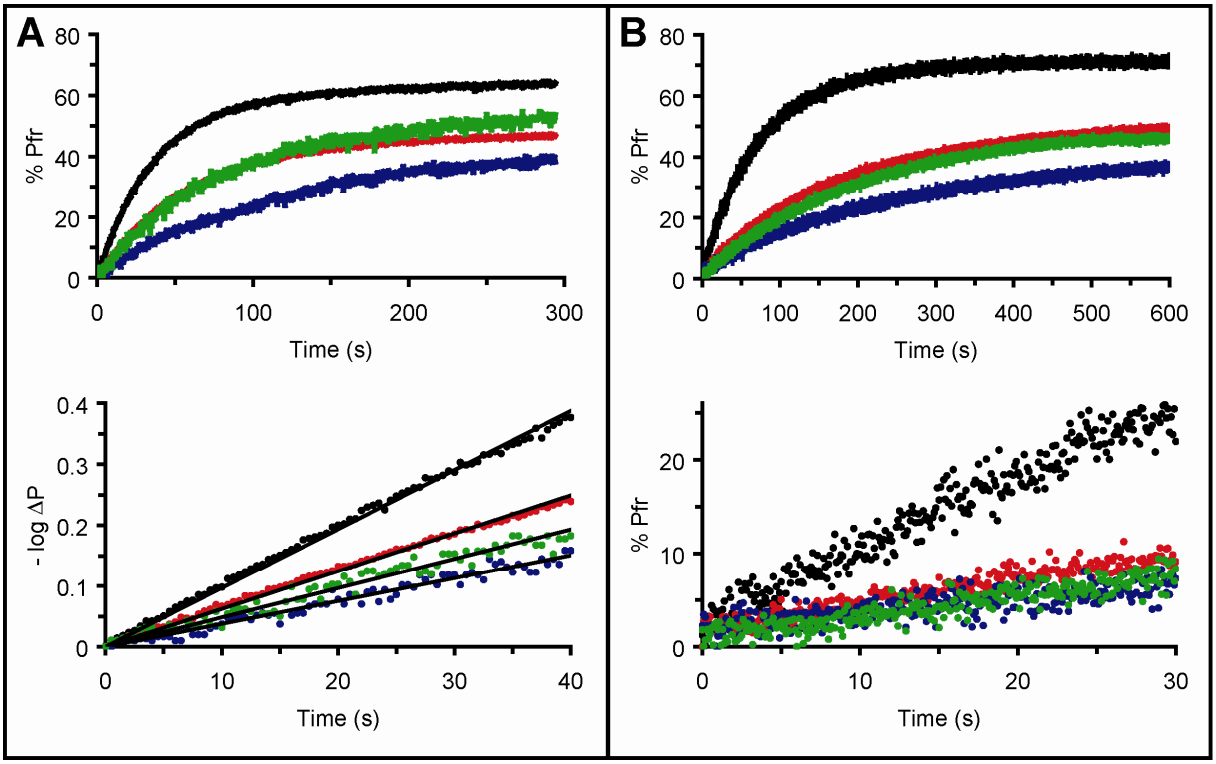

Figure 13: Phototransformation monitored by absorbance and fluorescence spectroscopy.
Pr → Pfr photoconversion of wt Cph1Δ2 (black), Y263F (red), Y263H (blue) and Y263S (green) monitored at $\lambda_{max,\ Pfr}$ by absorbance spectroscopy (A) or at 720 nm by fluorescence spectroscopy (B). The resulting initial slope of the curves (below) was used to determine the photoconversion rate constant k.

Although Y263F showed photochromicity similar to the wild type with blue-shifted maxima in Pr and Pfr (Table 6), the extent and quantum yield of phototransformation from Pr to Pfr wass considerably lower (79). Y263H generated a weak far-red shoulder associated with a similar bleaching of the Pr peak, but its photochromicity was much weaker than that of the wild type and Y263F. Nevertheless, Φ_P (Pr → Pfr) was higher in comparison to Y263F. Y263S showed a stronger bleaching of the Pr peak than was reflected in the far-red upon R irradiation. This difference rescued the $\chi_{Pfr,max}$ value, although the quantum yield of phototransformation (Φ_P = 0.05) was decreased further. Incidentally, $\chi_{Pfr,max}$ and Φ_P (Pr → Pfr) differed in both methods used, maybe due to the disproportionate decrease and increase of the

Pr and Pfr peaks, respectively. The calculated conversion from Pfr → Pr was almost the same for wild type Cph1 and the Y263 mutants.

Table 1: Photoconversion data of Cph1Δ2 and Y263 mutants.

Protein	wt	Y263F	Y263H	Y263S
Absorbance				
$\chi_{Pfr,max}$	0.70	0.50	0.46	0.60
k	0.010	0.007	0.004	0.005
Φ_P **(Pr → Pfr)**	0.13	0.05	0.07	0.05
Φ_P **(Pfr → Pr)**	0.11	0.10	0.11	0.09
Fluorescence				
$\chi_{Pfr,max}$	0.70	0.50	0.40	0.50
k	0.0050	0.0025	0.0017	0.0017
Φ_P **(Pr → Pfr)**	0.13	0.06	0.08	0.08

$\chi_{Pfr,max}$ (absorbance) was estimated by proportionally subtracting the spectrum of Pr from that following irradiation at Pr λ_{max} as described. The determination of Φ_P (Pr → Pfr) and k by measuring the photoconversion rate by UV-Vis and the calculation of Φ_P (Pfr → Pr) are described in 2.2.9. $\chi_{Pfr,max}$, k and Φ_P (Pr → Pfr) (fluorescence) were determined by measurement of the fluorescence decay upon irradiation at λ_{max} as described (2.2.11).

3.2.4. Fluorescence spectra

Wild type Cph1Δ2 and specific mutants (Y176H, Y203F, D207S, R254A (*in vitro* assembled), Y263F, Y263H, Y263S and T274A) within the chromophore pocket interacting directly (via H-bonds) with PCB in either Pr or Pfr states were characterised by fluorescence spectroscopy at ambient (T_a) temperatures (Figure 14 and Table 2).

The characteristics of the excitation and emission spectra of wild type Cph1Δ2 generally corresponded to those published earlier (81). A significant difference between the UV-Vis absorbance and fluorescence excitation spectra of the wild type was apparent (λ_{max} = 660 nm and 648 nm, respectively) however, implying that a minor, hypsochromically-shifted species might be responsible for fluorescence (see below). This effect was not significant in any of the investigated mutants, where discrepancies between $\lambda_{max,abs}$ and $\lambda_{max,exc}$ were negligible (~ 3 – 5 nm, Table 2).

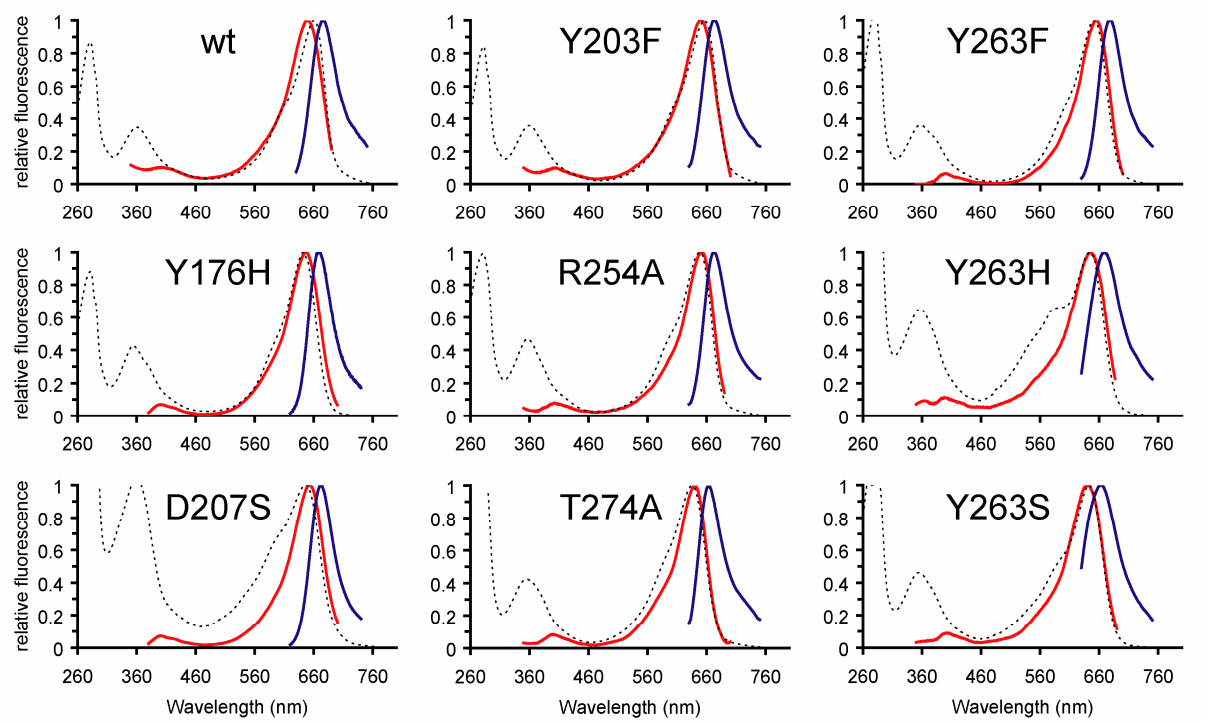

Figure 14: Fluorescence spectra of Cph1Δ2 and investigated mutants at T_a.
Excitation and emission spectra (shown in red and blue, respectively) were normalised to its maximum. The absorbance spectra (represented as dashed lines) were normalised to the maximum in the red regions)

Table 2: Fluorescence spectroscopy data of Cph1Δ2 and investigated mutants at T_a.

	Protein	wt	Y176H	Y203F	D207S	R254A	Y263F	Y263H	Y263S	T274A
	λ_{max} (Pr, abs.) (nm)	660	642	655	649	643	651	644	643	635
Excitation at T_a	λ_{max} (nm)	648	647	650	653	652	654	644	640	640
	λ_{soret} (nm)	401	401	404	401	402	400	399	402	399
	I ($\lambda_{max,red}$) / I (λ_{Soret})	9.7	14	10	14	13	15	8.9	11	12
	FWHM (nm)	62	54	56	54	46	52	62	60	46
Emission at T_a	λ_{max} (nm)	676	670	673	672	672	678	669	663	664
	FWHM (nm)	50	42	46	42	40	44	60	66	40
	Stokes shift (nm)	16	28	18	23	29	27	25	20	29
	λ_{max} (Em) - λ_{max} (Ex)	28	23	23	19	20	24	25	23	24
	Φ_F	0.024	0.15	0.027	0.094	0.025	0.084	0.067	0.10	0.060

FWHM of the excitation spectra was determined for λ_{max} by Gaussian approximation of the main red band, derived from the λ_{max} to 700 nm spectrum. FWHM of the emission spectra was determined for λ_{max} by Gaussian approximation of the main red band, derived from the 650 to λ_{max} spectrum.

Relative to the wild type, Y176H displayed the highest fluorescence quantum yield (Φ_F) of all mutants, being more than six times higher than in the wild type and consistent with almost absent photochemistry (Figure 46 and Table 6 in appendix 11.2) observed for this mutant.

Furthermore, the Stokes shift was increased considerably, implying a bigger loss of excitation energy upon decay to the lowest vibrational level of S_1. Tyr-176, is conserved among all known phytochromes, and its substitution to all other possible residues was described in detail in earlier publications (50, 78). Y203F and R254A, which has a similar albeit slightly lower extent of phototransformation (0.6 and 0.65, respectively), also has the same fluorescence quantum yield as wild type Cph1Δ2, implying that Φ_P (dependent on $\chi_{Pfr,max}$) and Φ_F are directly linked. Y203F displayed almost identical fluorescence (and absorbance) characteristics as wild type Cph1Δ2, which is not surprising considering the fact that in bacteriophytochromes, position 203 is occupied by a phenylalanine. D207S, bleaching upon R irradiation without being able to form Pfr, also showed increased Φ_F, being almost four times higher than in the wild type. The characteristics of the excitation and emission spectra of Y263F were almost identical with D207S, with a similar Φ_F. The emission maximum was red-shifted in comparison to wild-type Cph1Δ2, displaying a similarly high Stokes shift as Y176H. Interestingly, despite the dramatic difference seen in the absorbance spectra, the excitation spectrum of Y263H was almost identical to that of the wild type (79). The emission spectrum was significantly broader than that of the wild type and Y263F. Y263S showed similar excitation and emission spectra to Y263H, whereas the fluorescence quantum yield was five times that of the wild type, reflected in inefficient photochemistry. T274A, its λ_{max} (Pr) considerably blue-shifted by 25 nm, had a 2.5 times higher Φ_F, consistent with a 30 % lower extent of phototransformation than wild type Cph1Δ2.

The discrepancy between the absorbance and excitation maxima of wild type Cph1Δ2 was investigated further monitoring the excitation and emission at various wavelengths. The spectra were recorded at 77 K to prevent photoconversion from Pr to Pfr upon irradiation at wavelengths close to $\lambda_{max,red}$. Two distinct species could be identified using this procedure (Figure 15).

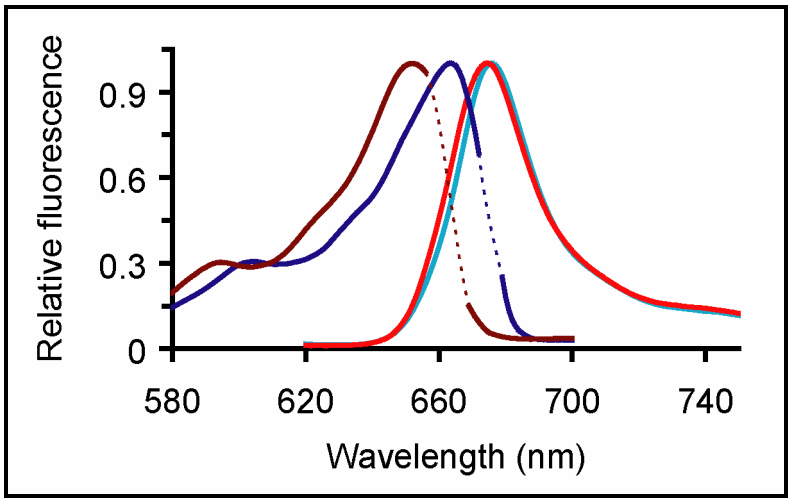

Figure 15: Fluorescence spectra of heterogeneous Cph1Δ2 at T_{77K}.
Excitation spectra were recorded at λ_{em} = 660 nm (brown) and λ_{em} = 676 nm (dark blue), respectively. Excitation at either 594 or 652 nm gave an emission spectrum with $\lambda_{max,em}$ = 674 nm (red) and excitation at either 606 or 660 nm gave an emission spectrum with $\lambda_{max,em}$ = 676 nm (cyan).

By monitoring the excitation spectrum at λ_{em} = 660 nm, a blue-shifted Cph1Δ2 form with an excitation maximum at 652 nm and a smaller, satellite peak at 594 nm could be identified. Excitation of Cph1Δ2 at either the satellite or the excitation maximum gave an emission spectrum with a maximum of 674 nm. If the excitation spectrum is recorded at λ_{em} = 676 nm on the other hand, a red-shifted Cph1Δ2 species with an excitation maximum closely matching the absorbance maximum at 664 nm and a smaller, satellite peak at 606 nm could be identified. Excitation of Cph1Δ2 at either the satellite or the excitation maximum gave an emission spectrum with a maximum of 676 nm. Since these fluorescence spectra were recorded at 77 K, a slight bathochromic shift of ~ 5 nm was to be expected since absorbance at T_{77K} also showed red-shifted λ_{max}. The two distinct species could not be identified at ambient temperatures, however.

3.2.5. Low-temperature fluorescence measurements

To investigate the primary photoprocesses involving a C15=C16 double-bound isomerisation of the D ring upon R irradiation finally leading to the formation of the lumi-R intermediate via the unstable pre-lumi-R, wildtype Cph1Δ2 and the Tyr-263 mutants (close to the D ring) were investigated by low-temperature fluorescence measurements. At 85 K, the excitation spectrum of Cph1Δ2 had its maximum at 659 nm, which was identical to the $\lambda_{max,red}$ of the

absorbance spectrum at T_a, but the peak width was much narrower at T_{85K} due to lower thermal movements (Table 3 and Figure 16).

Table 3: Fluorescence spectroscopy data of Cph1Δ2 and Y263 mutants at T_{85K}.

	Protein	wt	Y263F	Y263H	Y263S
Excitation at $T_{85\,K}$	λ_{max} (nm)	659	659	658	654
	λ_{soret} (nm)	399	399	399	402
	I ($\lambda_{max,red}$) / I (λ_{soret})	22	21	11	15
	FWHM (nm)	34	34	38	44
Emission at $T_{85\,K}$	λ_{max} (nm)	679	677	674	672
	FWHM (nm)	28	32	46	46
	λ_{max} (Em) - λ_{max} (Ex)	20	18	16	18
	ΦF	0.29	0.35	0.30	0.41
Ea	85 K - bp (kJ · mol^{-1})	3.1	2.5	3.0	2.9
	bp - 273 K (kJ · mol^{-1})	17.6	6.5	13.5	9.4
	bp (K)	219	219	225	219
Photoprocesses at T_a	k_F (10^7)	5.65	7.11	4.27	7.03
	k_d (10^8)	1.19	1.21	0.94	0.98
	k_P (10^9)	2.18	0.65	0.5	0.53
	τ_F (ns)	0.42	1.18	1.57	1.42
	Φ_P (pre-Lumi-R)	0.93	0.77	0.79	0.76
	Φ_{ab}	0.14	0.08	0.10	0.11

FWHM of the excitation spectra was determined for λ_{max} by Gaussian approximation of the main red band, derived from the λ_{max} to 700 nm spectrum. FWHM of the emission spectra was determined for λ_{max} by Gaussian approximation of the main red band, derived from the 650 to λ_{max} spectrum. Bp designates the breaking point of the linearization in Figure 18.

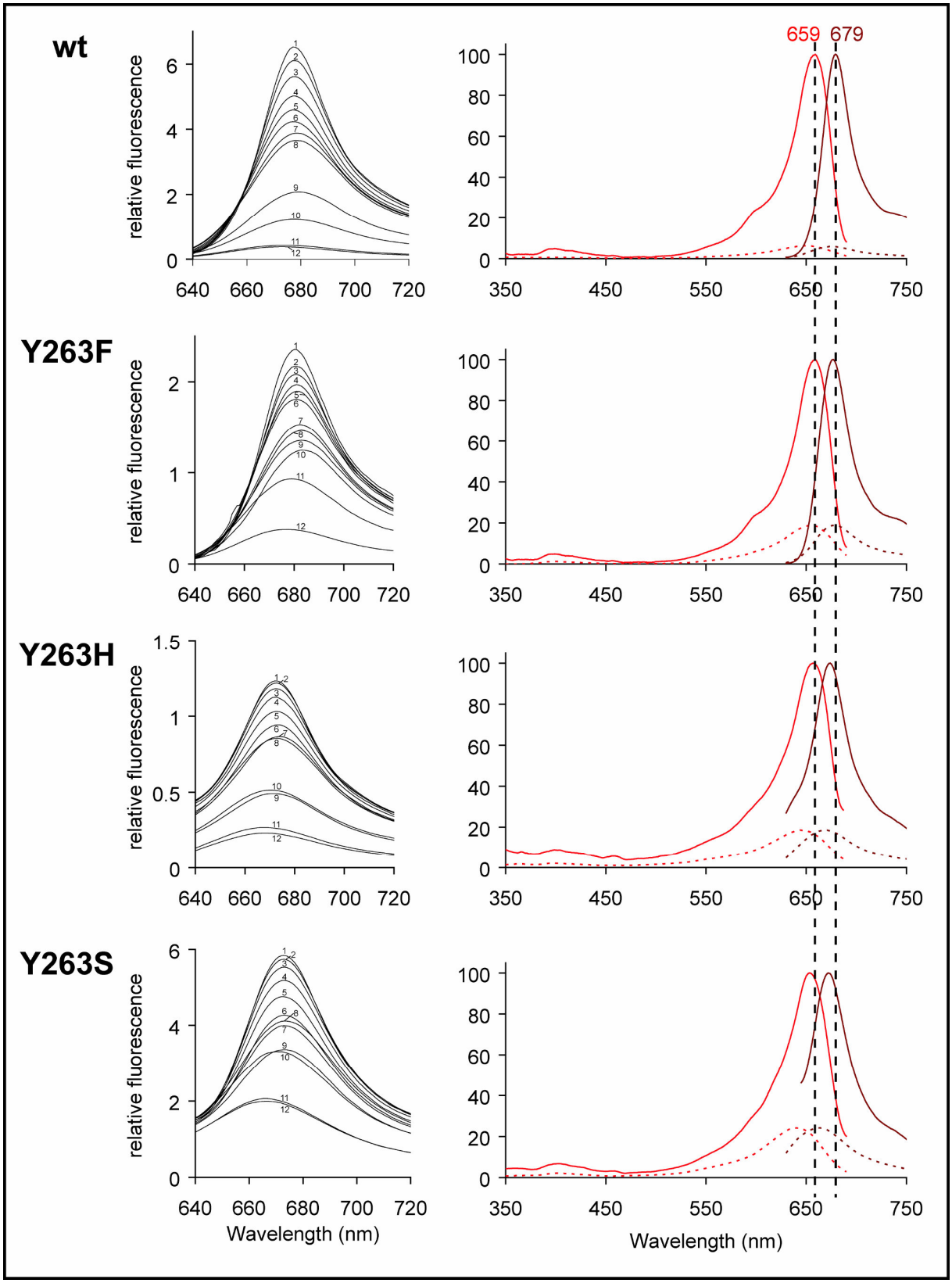

Figure 16: Temperature-dependent fluorescence spectra of wild type Cph1Δ2 and its Y263 mutants.
Temperature-dependence of the emission maximum (left) of wildtype Cph1Δ2 and its mutants Y263F, Y263H and Y263S monitored in steps of 20 K starting from 80 K (1) and going up to 300 K (12). Excitation (red) and emission (brown) spectra (right) of Cph1Δ2 and its Y263 substitutions at 293 K (dashed lines) and 85 K (solid line).

The Tyr-263 mutants had identical excitation maxima with the exception of Y263S with its excitation maximum blue-shifted by 5 nm. The excitation peaks of Y263H and Y263S were broader, implying that the chromophore might adopt several energetically favourable conformations, whereas for wild type Cph1Δ2 two distinct species could be observed (section 3.2.4). The emission maxima at T_{85K} were bathochromically shifted relative to their respective maxima at T_a. This shift was also observed in earlier low-temperature fluorescence measurements for *in vitro* assembled Cph1Δ2, where the emission spectrum not only lost fluorescence intensity but also gradually shifted to the blue with a dramatic widening around 220 K (81, 82). *In vivo* assembled Cph1Δ2 and Tyr-263 mutants also showed a similar hypsochromic shift of the emission maximum with rising temperature culminating in a severe widening of the spectrum and a ~ 3 – 5 nm blue-shift around 260 K for Cph1Δ2 and Y263F, a 5 nm blue-shift around 220 K for Y263H and a 7 nm blue-shift around 240 K for Y263S (Figure 16 and Figure 17).

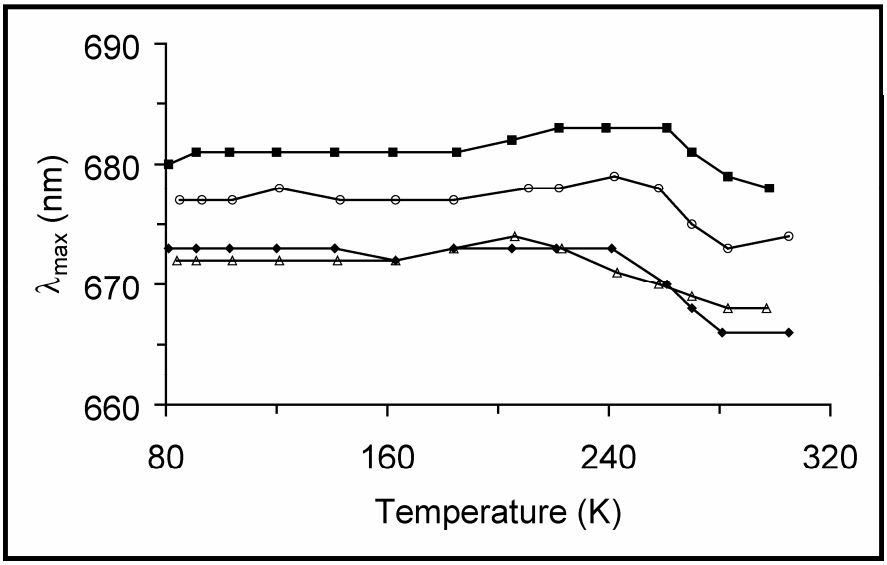

Figure 17: Temperature dependence of the emission λ_{max} of Cph1Δ2 and Y263 mutants.
The emission λ_{max} of Cph1Δ2 (▪), Y263F (○), Y263H (Δ) and Y263S (♦) were taken from the emission spectra determined in Figure 16.

The fluorescence quantum yield at T_{85K}, determined relative to the Φ_F at ambient temperatures, is ~ 0.3 for *in vivo* assembled Cph1Δ2, which corresponded to the Φ_F determined for *in vitro* assembled Cph1Δ2 and plant phytochromes (82). Y263F and Y263S displayed higher fluorescence quantum yields than wild type Cph1Δ2 at 85 K, comparable to Φ_F determined at ambient temperatures (Table 2 and Table 3). Y263H, on the other hand, had

the same Φ_F than wild type Cph1Δ2 at 85 K although at ambient temperatures the fluorescence quantum yield was almost three times higher.

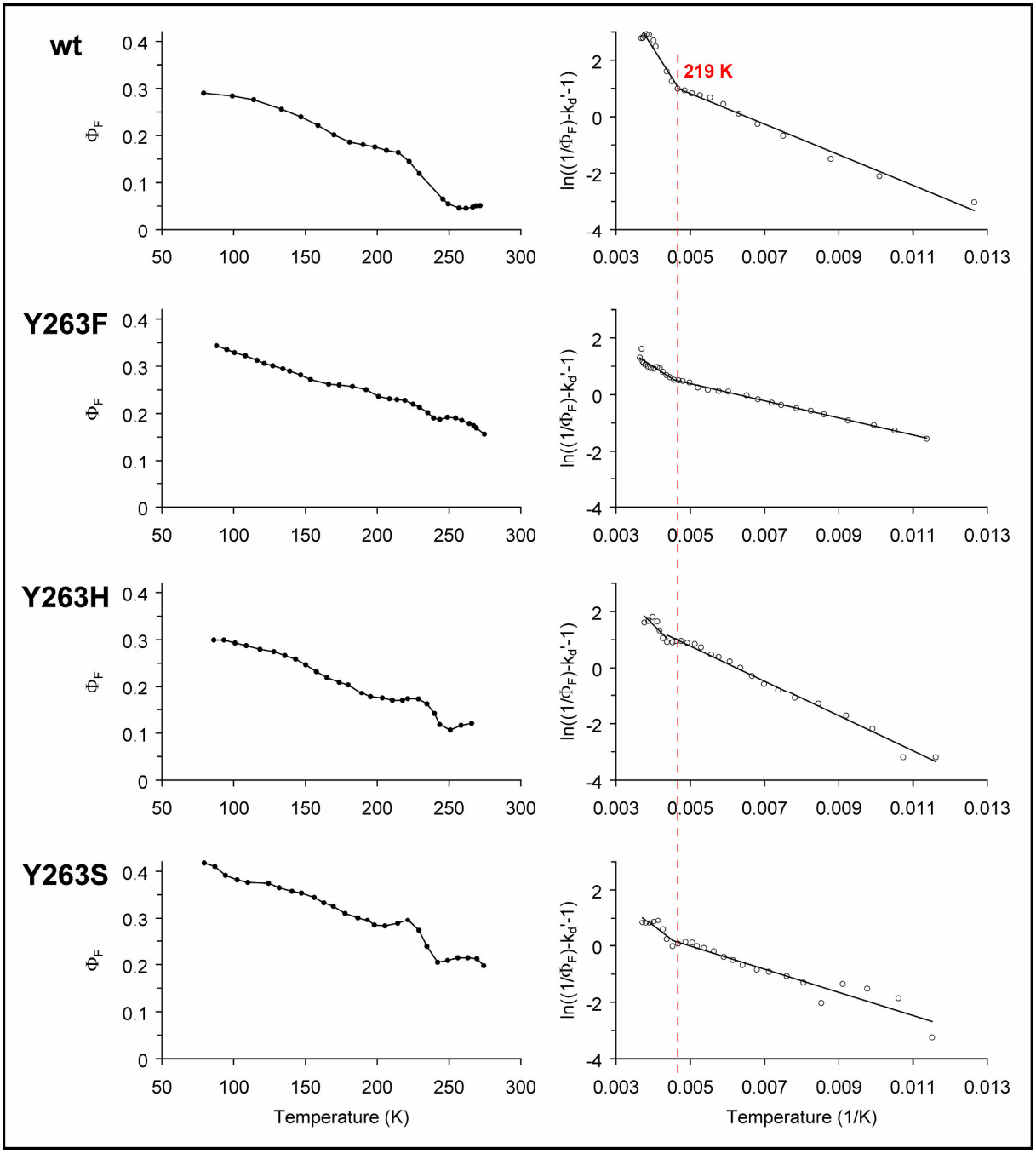

Figure 18: Temperature dependence of the fluorescence intensity of Cph1Δ2 and Y263 mutants.
Temperature dependence of the fluorescence intensity (left) of Cph1Δ2 and Y263 mutants with λ_{exc} = 610 nm was monitored at the respective $\lambda_{max,\ em}$ and linearization of the temperature-dependent curves in Arrhenius coordinates (right) was done using the Φ_F as determined in Table 3. The breaking point of the linearised curve of Cph1Δ2 at 219 K is indicated by a red dashed line (right).

As was the case for *in vitro* assembled Cph1Δ2 (82), the lumi-R state could not be trapped neither at low temperatures for *in vivo* assembled Cph1Δ2 nor the Tyr-263 mutants.

Nevertheless, the determination of the activation energies of the fluorescence decay (Ea), which correspond to the activation energy of the Pr → lumi-R photoreaction, could be obtained by linearization of the temperature-dependent intensity curves in Arrhenius coordinates (Figure 18 and Table 3). A steep decrease of the fluorescence intensity of *in vivo* assembled Cph1Δ2 could be observed upon reaching ~ 220 K, which corresponds to the breaking point in Arrhenius coordinates, a phenomenon also observed for *in vitro* assembled Cph1Δ2 (82) as well as plant phytochromes (37), leading to activation energies of 3.1 and 17.6 kJ / mol respectively. The fluorescence intensity of Y263F seemed to decrease gradually with only minor changes after 220 K, which was also reflected in the activation energies which, especially for higher temperatures, were considerably lower than in wild type Cph1Δ2. In the case of Y263H and Y263S, strong fluctuations of the fluorescence intensity were observed after 220 K, which suggests a higher flexibility of the D ring in the chromophore pocket at higher temperatures, although the activation energies were similar to those determined for Cph1Δ2 and higher than for Y263F.

The rate constant of fluorescence (k_F) is dependent on the Pr spectrum in the red region, hence Y263F, with its $\lambda_{max,\ red}$ at 651 nm and an ε identical to wild type Cph1Δ2, had the highest k_F followed by Y263S, whose $\lambda_{max,\ red}$ was even further blue-shifted, but the extinction coefficient was lower. The radiative lifetime, dependent on Φ_F, was lowest in Cph1Δ2 implying that most of the absorbed light follows the photochemical pathway, rather than decaying by fluorescence.

The temperature-independent excitation dissipation into heat (k_d) was approximately the same in all investigated samples and with an order of magnitude of 10^8 identical with those determined for plant phytochromes (45). The primary photoreaction (k_P) from Pr → pre-lumi-R was four times higher in wild type Cph1Δ2 than in the Tyr-263 mutants, which had similar rate constants. Subsequently, the quantum yield of the primary photoreaction (Φ_P (pre-Lumi-R)) was also higher and close to unity for Cph1Δ2 whereas in the Tyr-263 mutants it was close to 0.8. The quantum yield of phototransformation from pre-lumi-R to lumi-R (Φ_{ab}) was close to the quantum yield of phototransformation from Pr to Pfr and thus highest

in Cph1Δ2. As published earlier, the rate limiting step for the Pr → Pfr phototransformation is determined by the pre-lumi-R → lumi-R photoreaction.

3.3. Quaternary structure analysis

Although the dimerisation domain, located in the transmitter module of full-length Cph1, has been removed in the Cph1Δ2 construct, the sensor module comprising the first 514 amino acids, showed state-dependent dimerisation, K_A (determined by analytical ultracentrifugation) for Pfr being at least 20-fold higher than for Pr (83). To confirm state-dependent dimerisation of the *in vivo* assembled holophytochrome Cph1Δ2, both *in vitro* and *in vivo* assembled protein were subjected to analytical size exclusion chromatography at 2.3 and 0.25 mg / ml (Figure 19). Whereas *in vitro* assembled Cph1Δ2 Pfr eluted as a dimer and Pr as a monomer at 2.3 mg / ml, the *in vivo* assembled holoprotein showed one single peak around 126 kDa, corresponding to the size of the dimer. The Pr form of *in vivo* assembled Cph1Δ2 only eluted as a monomer at concentrations around 0.25 mg /ml. Along with the spectral properties, the behaviour in SEC constitutes another notable difference between *in vivo* and *in vitro* assembled Cph1Δ2. Nevertheless, the single peak observed for *in vivo* assembled Cph1Δ2 at 2.5 mg / ml was shifted when comparing the monitored wavelengths. The narrow 700 nm curve, which is indicative for the Pfr state and has its maximum absorbance at 69.8 ml, eluted first. The curves monitored at λ_{ibp} and λ_{max} (Pr) followed with their respective maxima at 70.2 and 70.5 ml and were generally broader implying that the Pr dimerisation indeed was weaker, which was shown by AUC experiments (83, 84).

Only few mutants showed the same behaviour in SEC as *in vivo* assembled wild type Cph1Δ2 (Figure 19 below, Figure 49 – Figure 51 and Table 7 in appendix 11.3). S11A, Y176H, Y203F, Y203W, F216A and G451A showed a single peak at the apparent M_w of ~120 kDa, corresponding to the dimer. With the exception of Y176H, all of these mutants showed normal photochromicity with similar ε (Pr λ_{max}) than wild type and did not seem to affect the quaternary structure of Cph1Δ2. Y176H is locked in the Pr state and hence a single peak was to be expected.

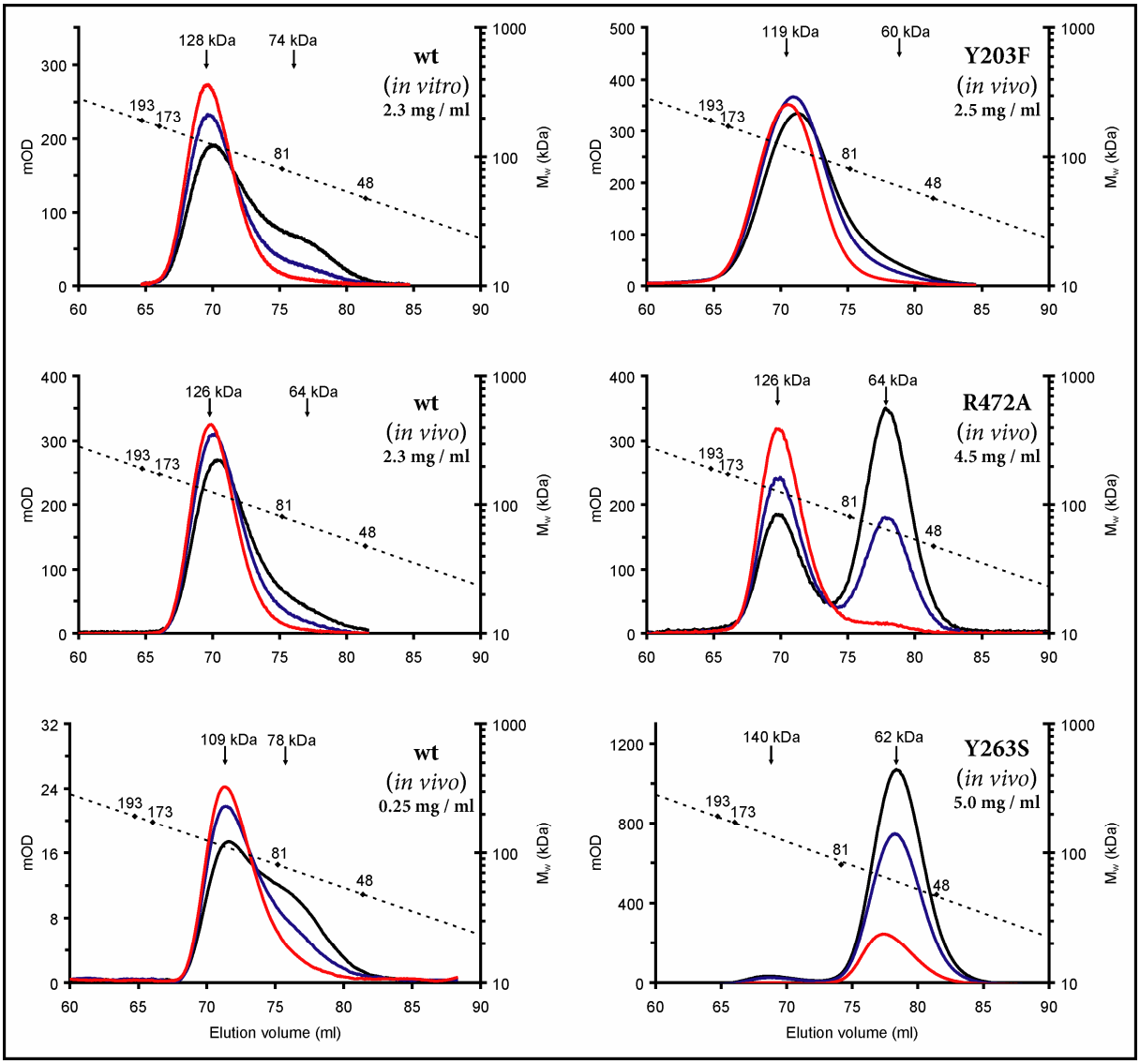

Figure 19: Analytical SEC of Cph1Δ2 and selected mutants.
Size exclusion chromatography after red irradiation of Cph1Δ2 wild type (*in vivo* and *in vitro* assembled), Y203F, R472A and Y263S at given concentrations. Size exclusion chromatography runs were monitored at the $\lambda_{max,\ red\ (Pr)}$ (black) and λ_{ibp} (blue) of the specific mutants as well as at 700 nm or the respective $\lambda_{max,\ red\ (Pfr)}$ (red) for Pfr. The dotted line indicates the calibration of the column with specific proteins (kDa).

Most of the investigated mutants displayed two separate peaks in the elution profile, resembling the situation of *in vivo* assembled Cph1Δ2 at low concentrations or *in vitro* assembled Cph1Δ2 at 2.5 mg / ml, where Pfr eluted mostly as a dimer and Pr preferentially as a monomer. Unlike *in vitro* Cph1Δ2, where the dimer and monomer peaks partially overlapped and no $\chi_{Pfr,\ max}$ could be deduced based on the chromatogram, NTLΔ (1-20), L201Q, S251A, R254A (*in vivo* and *in vitro* assembled), R254K, Y263F, S272A, T274A, W450A, G452A, Y458A, Y458S, R472A, F475H and F475Y showed two clearly distinct peaks without any shifts at the three monitored wavelengths, their $\chi_{Pfr,\ max}$ similar to the one

determined by spectral subtraction (Table 6 and Table 7 in appendix 11.2 and 11.3, respectively). These mutants all showed normal photochromicity. R222A and R222K showed a single, but broadened elution peak, making it difficult to distinguish between dimer and monomer. This could be partially due to the fact, that upon R irradiation, the appearing Pfr shoulder was very weak and thus the absorbance at $\lambda_{max,\ Pr}$, λ_{ibp} and $\lambda_{max,\ Pfr}$ was very similar. This could be observed in the beginning of the elution profile of R222A (~ 72 ml) and R222K (~ 70 ml) and hence, the shoulder and the first peak in the case of R222A and R222K respectively corresponded to the Pfr, which would be a dimer. The following peak around 76 ml and the shoulder around 74 ml of R222A and R222K respectively, where absorbance at $\lambda_{max,\ Pr}$ was significantly higher than absorbance at λ_{ibp} and 700 nm, corresponded to Pr and hence a monomer. Mutants, bleaching upon R irradiation without formation of a distinct Pfr peak / shoulder (Y203H, Y203N, D207C, D207N, D297R / R472D, D207S, R213S, H260Y, Y263H, Y263S, P471G, S474A, F475A and tongueΔ (462-480)) displayed a single peak around the apparent M_w of 60 kDa corresponding to the monomer of the sensor module of phytochrome. Interestingly, several of these mutants had an increased dark reversion rate, most notably all D207 mutations. Mutants eluting as a monomer did not show any significant shifts of the peak at the three monitored wavelengths, implying that differences between "Pfr" and Pr either did not affect the structure of the monomer in the case of these mutants or that structural changes could not be triggered due to the mutation.

3.4. X-Ray structure analysis

3.4.1. Crystallisation and structural characterisation of Cph1Δ2

Blue-green tetragonal crystals of *in vivo* assembled Cph1Δ2 in the Pr state at a concentration of 10 mg / ml appeared in 2.5 M sodium acetate / 0.1 M sodium acetate pH 4.6 (final pH 6.7) (Anions suite, Qiagen) after one week of incubation at 18 °C in darkness, and reached full size after 3 weeks (Figure 20). Further optimization was done in 96-well Greiner plates and/or 24-well Nunc plates using hanging-drop vapour diffusion as described in 2.2.12. Optimal diffraction (~ 2.45 Å) was achieved with a 200 x 100 µm tetragonal crystal ($P4_32_12$) picked from 2 M sodium acetate / 0.1 M magnesium acetate pH 5.0 (overall pH 6.7) (61).

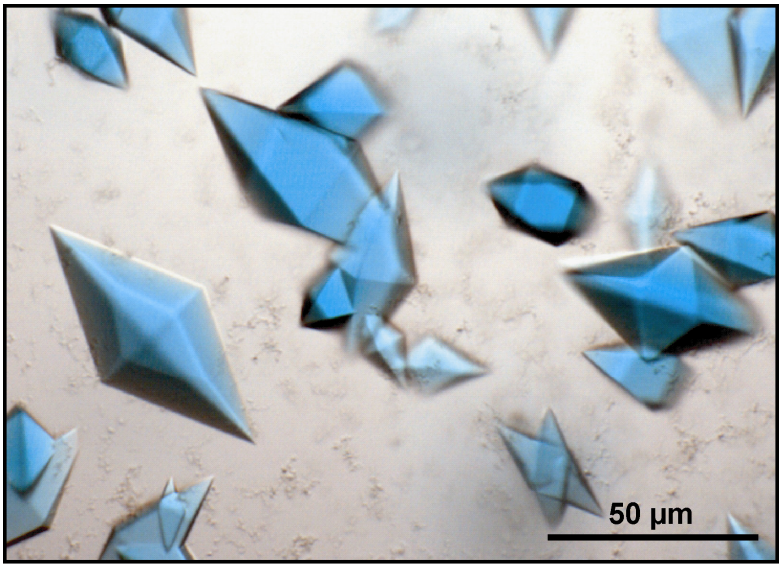

Figure 20: Crystals of the Cph1 sensory module in the Pr state.

Crystallisation procedures and crystal observations were initially done under blue-green safe light conditions and later using the IR setup described in (62). Cryo-protection of Cph1Δ2 crystals under white light with 20 % glycerol resulted in poor crystal diffraction (4-6 Å resolution, Table 4 and Figure 21) and systematic formation of ice-rings. The quality of diffraction did not improve even when the percentage of glycerol was increased to 40 %. Only when crystals were thawed and partly dried in air for ~15-30 seconds before refreezing was an improvement of diffraction observed (best native crystal showed anisotropic diffraction of 2.8 x 2.8 x 3.45 Å). Further improvement of diffraction consisted in optimizing the original crystallisation condition by using acetate salts at various concentrations (overall pH 6.6 – 7.2) in darkness. Crystals grown with 0.1 M ammonium or calcium acetate did not improve diffraction whereas 0.1 M magnesium acetate together with 2 M sodium acetate (overall pH 6.7) yielded the best diffracting crystals (61). Thus, for cryo-protection the crystallization buffer was supplemented with 25% $Mg(OAc)_2$ (68) instead of glycerol, but the previously observed anisotropy remained (maximal resolution: 2.7 x 2.7 x 2.2 Å) (Figure 21) (62).

Table 4: Data collection for Cph1Δ2 using different crystal freezing conditions.

Data collection for Cph1Δ2 crystals		
Data processing	**blue light & glycerol**	**IR & cryo salts**
Beamline	X-13, EMBL, Hamburg	ID14-3, ESRF, Grenoble
Wavelength (Å)	0.8015	0.933
Detector	MAR CCD 165 mm	ADSC Q4 CCD
Space group	$P\,4_32\,1$	$P\,4_32\,1$
***a*, b, c (Å)**	75.69, 75.69, 246.58	77.18, 77.18, 249.00
Maximal resolution (Å)	3.15 x 3.15 x 2.8	2.70 x 2.70 x 2.20
Total reflections	76347	183551
Unique reflections	14707	26369
Completeness [a]	0.789 (0.166); 0.976	0.672 (0.067); 0.985
$\langle I \rangle / \sigma\langle I \rangle$ [a]	16.5 (3.8)	23.0 (3.5)
R_{merge} [b]	0.072 (0.324)	0.049 (0.361)
Mosaicity (°)	0.42	0.35
Wilson *B* -factor (Å^2)	56.6	17.3

[a] values in parentheses correspond to the highest resolution shell; 2nd completeness corresponds to range 25-3.15 Å and 25-2.70 Å, respectively

[b] $R_{merge} = \Sigma_{hkl} \Sigma_i \; (I_i(hkl) - \langle I(hkl) \rangle) \; / \Sigma_{hkl} \Sigma_i I_i(hkl)$

Due to the strong anisotropy, the diffraction data needed to be rescaled to successfully solve the structure of the Cph1 sensory module. Rescaling was performed by Prof. Lars-Oliver Essen using the Diffraction Anisotropy Server (www.doe-mbi.ucla.edu/~sawaya/anisoscale). Anisotropic corrections of 35.88, 35.88 and 17.94 Å^2 for the native Cph1Δ2 dataset and 41.56, 41.56 and 20.78 Å^2 for the SeMet-Cph1Δ2 MAD dataset were applied (b_{11}, b_{22} and b_{33}, respectively). The effective, calculated resolution for the anisotropic native dataset (2.7 Å, 2.7 Å and 2.2 Å) corresponds to 2.45 Å assuming a theoretical completeness of 100 % at that resolution. The completeness of the native Cph1 dataset at 2.7 Å resolution was 98.5 % overall (2.8-2.7 Å: 100 %). Initial MAD-phasing with the AUTO-RICKSHAW suite (85) followed by refinement of the selenium sites using the SHARP package (86) was done by Prof. Lars-Oliver Essen. Further automated and manual refinement with REFMAC5 (87) and COOT (88) finally yielded a model of the sensory module defined for residues L4-H520 (PDB code: 2VEA) omitting disordered loop regions Q73-R80, G100-D101, R148-Q150 and E463-G465 (Table 8 in appendix 11.4.1) (61).

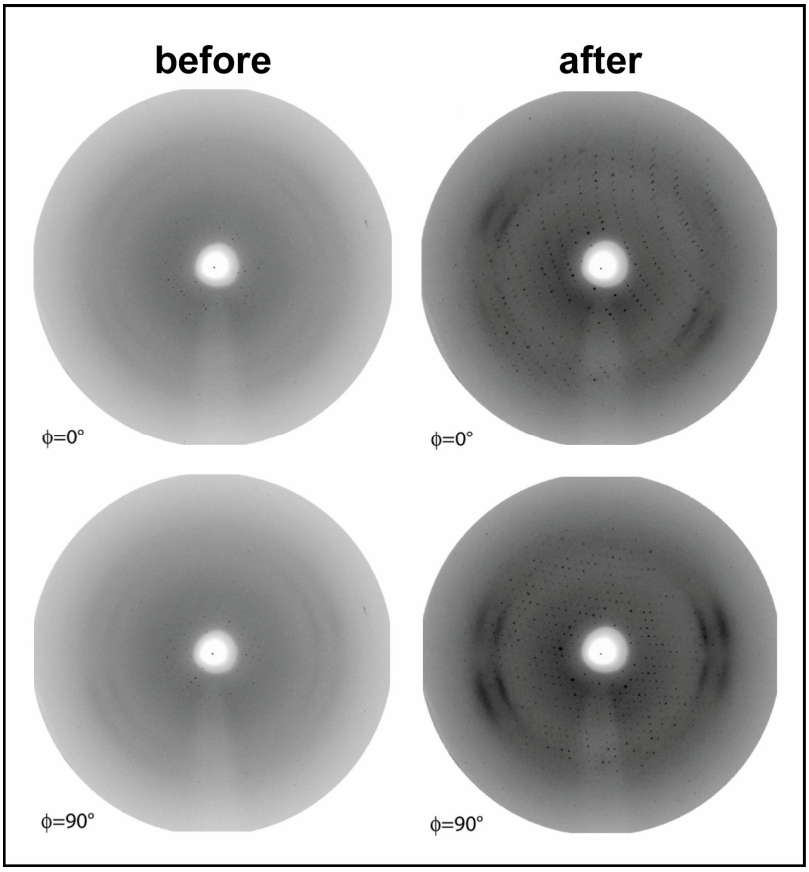

Figure 21: Diffraction patterns prior to and after cryo-annealing.
Figure taken from (62).

The stereochemistry at the $C3^1$ atom for the PCB-C259 adduct in the sensory module of Cph1 could not be solved based on the available data, hence stereochemical restrains were used (89). Analysis of the electron density around the chromophore and the thioether bond specifically did not reveal any anomalies. Analysis of difference Fourier syntheses of datasets collected from the same crystal exposed to different doses of X-ray radiation did not show any damage in contrast to the observations of PAS-GAF bidomain bacteriophytochromes (30, 32), where radiation damage severed the thioether linkage between the chromophore BV and the respective cysteine. Whether this severance results from the fact that BV binds to a cysteine at the extreme N-terminus, from the formation of the thioether bond at the $C3^2$ atom or from incomplete sealing of the chromophore pocket remains to be investigated.

In contrast to all published bacteriophytochrome structures to date (30-32, 72, 90, 91), *in vivo* assembled Cph1Δ2 crystallised as an antiparallel dimer (Figure 22) along the α9 helix (61). The surface area of this extensive dimer is 2545 $Å^2$ per monomer and the C-termini of the two monomers are separated by 110 Å. The 2VEA structure comprises the PAS-GAF bidomain,

which forms the larger lobe and is already known from the bidomains of the bacteriophytochrome structures (30, 32) and the PHY domain (Thr-324 - Glu-514) which forms the smaller lobe. The PAS and GAF domains are tightly packed together by forming a figure-of-eight knot between the N-terminus and a protrusion from the GAF domain, like bacteriophytochrome bidomain structures (30, 32) (Figure 23B and Figure 24B), although the chromophore is linked to a cysteine within the GAF domain negating the close proximity of the N-terminus to the chromophore. Nevertheless, the knotted PAS-GAF bidomain might play an additional role in the stabilisation of the chromophore cavity.

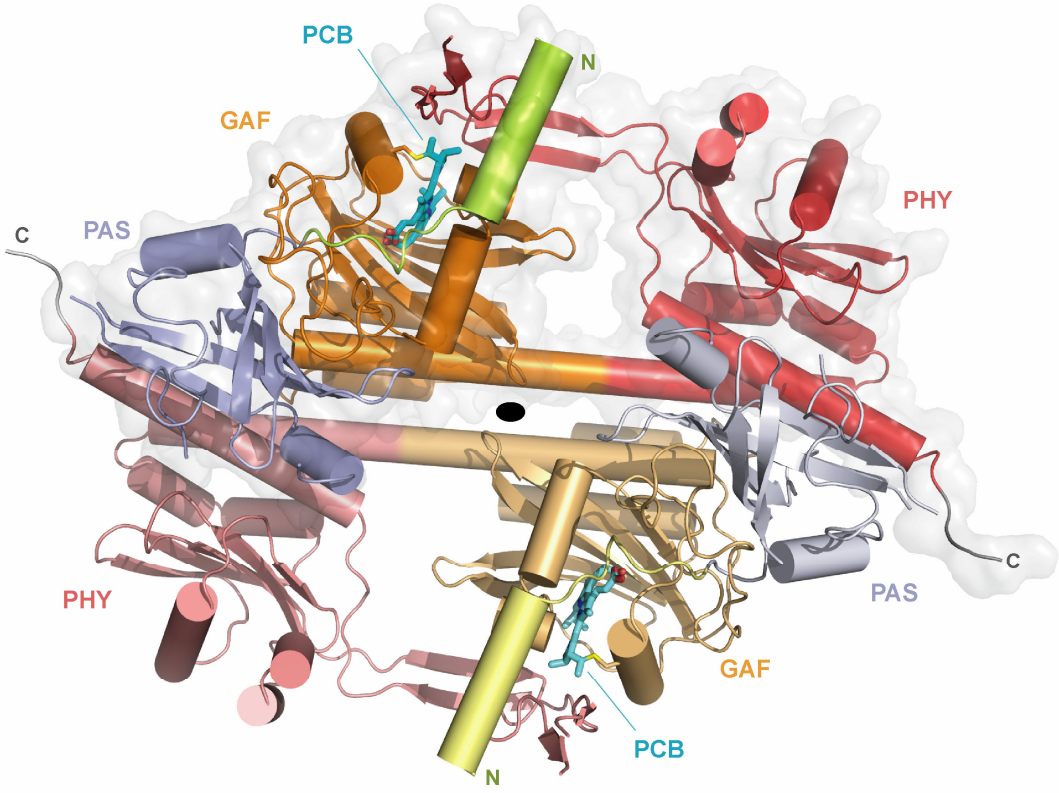

Figure 22: Cph1 sensory module antiparallel dimer as defined by crystal symmetry.
Figure taken from (61).

The PAS-GAF bidomain covalently connects to the PHY domain via a 66 Å α-helix (Phe-299 – Ala-345) which also forms the dimer interface mentioned above (61). A second interaction comprises hydrogen bonds and salt bridges involving a tongue-like protrusion from the PHY domain which seals the chromophore pocket formed by the N-terminal α1 helix and the PCB-containing GAF domain. The phytochrome-specific PHY domain displays a similar architecture as the GAF domain and has previously been proposed to be structurally related to the latter (18, 19), although the sequence similarity is low (<15% identity at the amino acid level). DALI comparisons clearly show that PHY belongs to the GAF domain family (Figure

24C) (61). A structure-based alignment with related domains and the secondary structure of Cph1Δ2 is shown in the appendix 11.4.2.

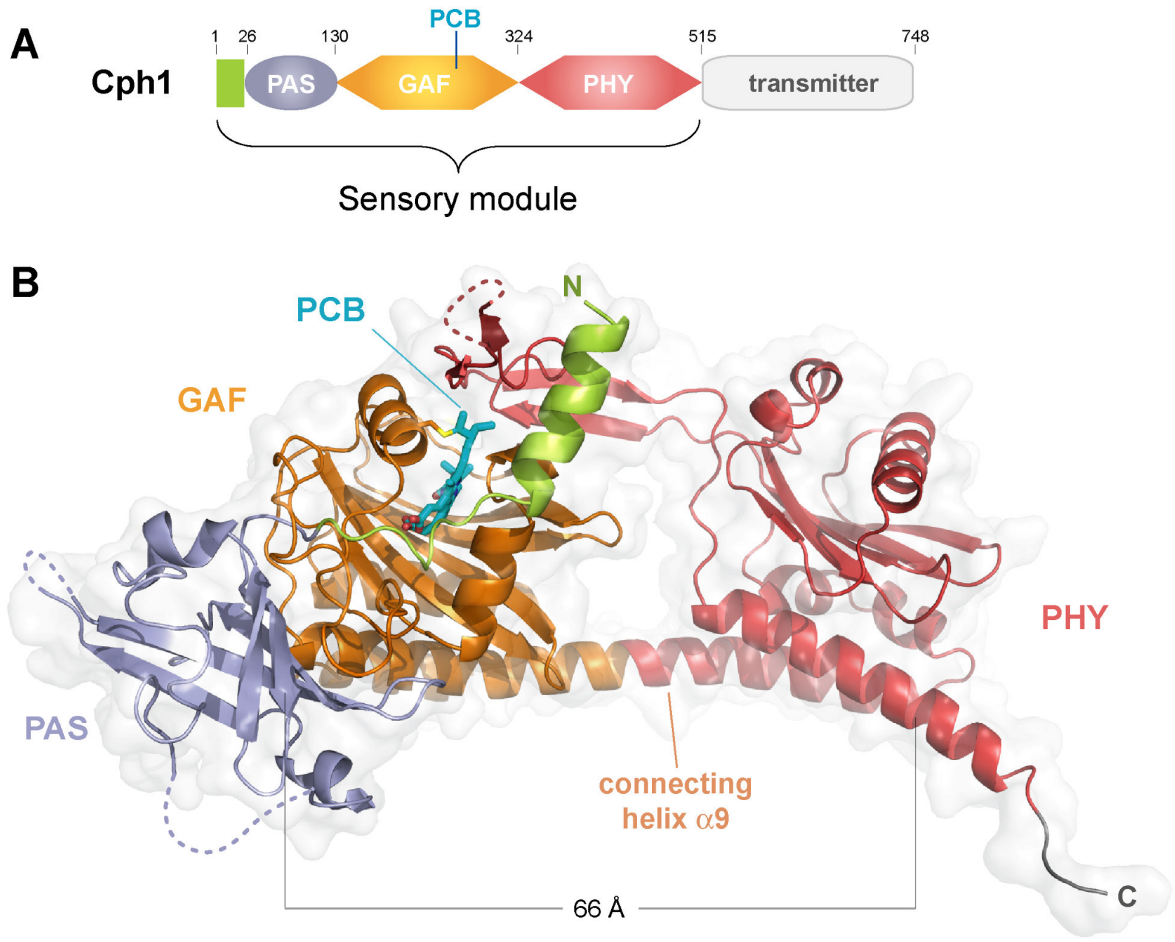

Figure 23: Structure of the Cph1 phytochrome sensory module.
(A) Domain boundaries of Cph1 phytochrome. In the recombinant Cph1 sensory module described, the C-terminal histidine kinase transmitter (Leu-515 - Asn-748) is replaced by a $(His)_6$ tag. (B) Ribbon representation of the sensory module structure showing the N-terminal α-helix (green) and PAS (blue), GAF (orange) and PHY (red) domains. The phycocyanobilin chromophore (cyan) is covalently attached to Cys-259. Disordered loop regions (Gln-73 – Arg-80, Gly-100 – Asp-101, Arg-148 – Gln-150, Glu-463 – Gly-465) are indicated as dotted lines. (Taken from (61))

Obvious structural differences between the GAF and PHY domains affect the respective protrusions from the β-sheet / α-helix sandwich: the loop protruding between the β9 and β10 sheets of the GAF domain forms the knot whereas the protrusion from sheet β11 forms the connecting helix α9 (appendix 11.4.2). The protruding loop between β14 and β15 sheets of the PHY domain is much smaller and thus unable to form a potential knot. The protrusion from sheet β16 comprises a long loop with four β-sheets (Pro-442 - Gln-490), however, and thus is able to connect to the GAF domain. The long α9 helix extending from the GAF domain and

the tongue-like protrusion from the PHY domain not only connect both lobes intricately but also keep them apart and leave a pseudo-hole in the sensory module. Whether this hole plays a major role in the binding of a potential response regulator or whether the dumbbell-like structure constitutes a sort of lever in the signalling mechanism cannot be concluded from the current data.

A similar structural arrangement of two consecutive GAF domains, missing the respective protrusions, is observed in the regulatory module of cyclic nucleotide phosphodiesterases (92, 93) and eubacterial adenylyl cyclases (94, 95) (PDE and AC, respectively). These tandem-GAF domains are able to bind small nucleotides and either synthesize or hydrolyse CNMPs. Like the sensory module of Cph1, the GAF domains in PDEs and ACs are separated by a 50 – 60 Å connecting α-helix (Figure 24A) (93, 95).

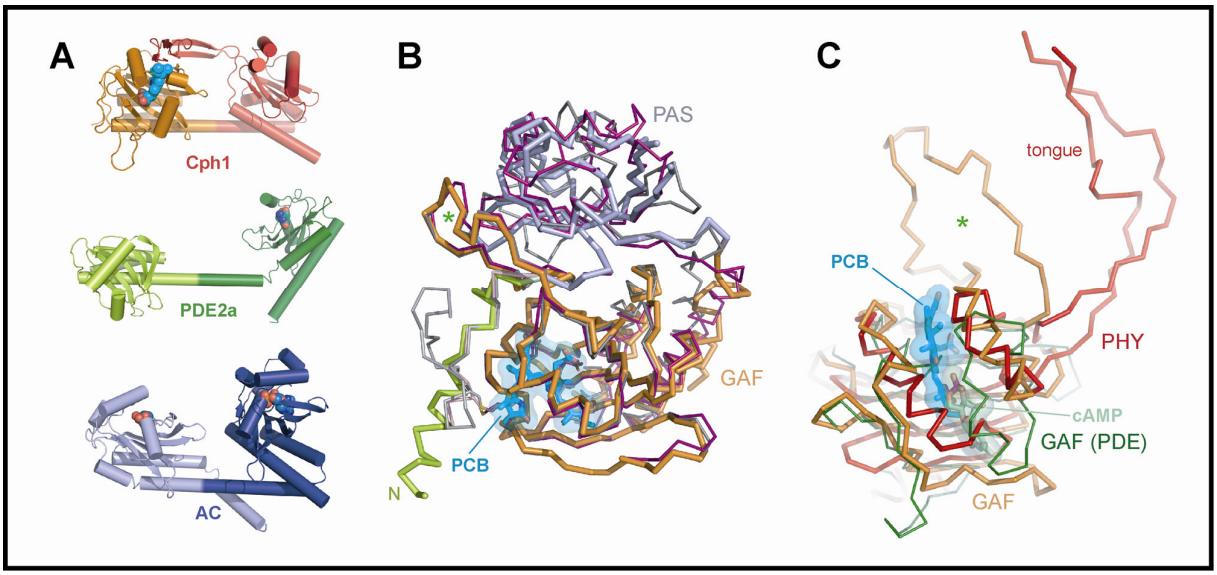

Figure 24: Structural comparisons of sensory module domains.
(A) Tandem-GAF domain arrangements as observed in Cph1 (orange / red), a murine phosphodiesterase (93) (green) and a cyanobacterial adenylyl cyclase (95) (blue). (B) The PAS/GAF bidomain. The PCB chromophore (cyan), N-terminal α-helix (green), PAS (light blue) and GAF (orange) domains of Cph1 are superimposed upon corresponding elements of the bacteriophytochrome bidomains of *Deinococcus radiodurans* (31) (grey, r.m.s.d. 1.08 Å for 235 C -positions) and *Rhodopseudomonas palustris* (32) (purple, r.m.s.d. 1.10 Å for 252 C) which bind biliverdin IX (BV). (C) Superposition of the Cph1 PHY (red) and GAF (orange) domains and the N-terminal GAF domain of phosphodiesterase 2a (93) (green). Superposition of PHY and its closest homolog, the Cph1 GAF domain, gives an r.m.s.d. of 1.77 Å for 94 equivalent C positions. The green asterisk marks the loop of the GAF domain through which the N-terminus passes to form the knot. The cyclic nucleotides (green) and the PCB chromophore (cyan) bound within the respective GAF domains are shown with their molecular surfaces thus indicating the partial overlap of their binding sites. (Taken from (61))

Although cGMP is thought to be implicated in plant phytochrome signalling (96, 97), the structure of the PHY domain in 2VEA and most likely also plant phytochromes does not

present any space to bind small nucleotides (Figure 24C) (61). Crystallisation with cyclic nucleotides yielded crystals of the same shape and form in identical conditions as wild type Cph1Δ2, but no surplus electron density could be observed within the PHY domain after diffraction analysis of these crystals.

Despite earlier structures of PAS-GAF bidomains displaying a chromophore cavity within the GAF domain, where the chromophore was accessible to the outside solvent, sequence alignments showed that the residues forming the chromophore pocket were highly conserved whereas residues presented on the surface of the bidomains showed low sequence identity within the phytochrome family, indicating that additional residues might be involved in the formation of a complete chromophore pocket (Figure 3). The now resolved complete structure of the sensory module indeed shows that the PHY domain seals the cavity within the GAF domain with its protruding tongue, thus shielding the chromophore from outside solvent (Figure 25) (61).

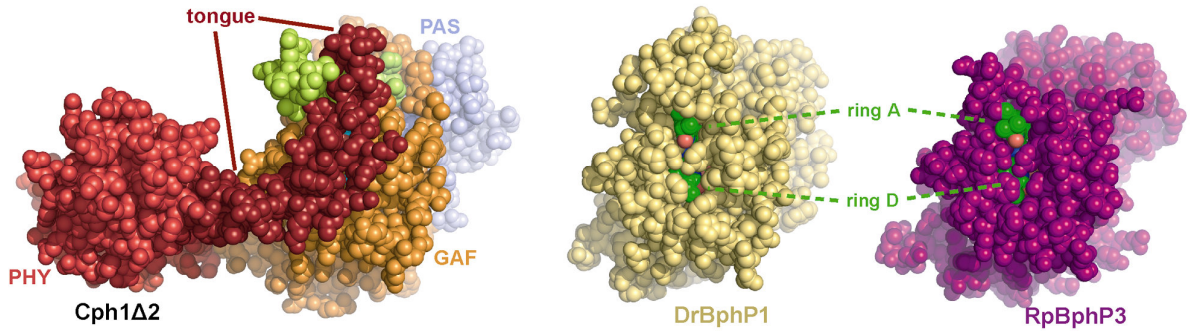

Figure 25: Space filling models of phytochrome structures
Space-filling model of Cph1Δ2 (left) in comparison to known bacteriophytochrome structures (31, 32). The PCB chromophore (cyan) is completely sealed from solvent access by the tongue (dark red) in contrast to the exposed biliverdin (green) in the incomplete bidomains (modified from (61)).

The tongue-like protrusion from the PHY domain of the Cph1 sensory module not only covers the chromophore cavity in the GAF domain, but also interacts with the N-terminal α-helix (Thr-4 – Leu-18) via a hydrogen bond between Tyr-458 and Ser-11 (Figure 26A). The structure-based alignment of the PHY domains of various phytochromes across all kingdoms shows that the tongue is present in all canonical phytochrome classes and that its respective length varies (appendix 11.4.2). This is not surprising considering that the tip of the tongue is disordered and partly unresolved in 2VEA probably due to its high mobility and its lack of interactions with nearby residues. Furthermore, three motifs could be identified based on the

structural alignment: the PRxSF motif (Pro-471 – Phe-475) specifically interacts with residues within the GAF domain whereas the WGG and WxE motifs (Trp-450 – Gly-452 and Trp-478 – Glu-480, respectively) are probably responsible for the kink of the tongue (Figure 26 and Figure 27) (61).

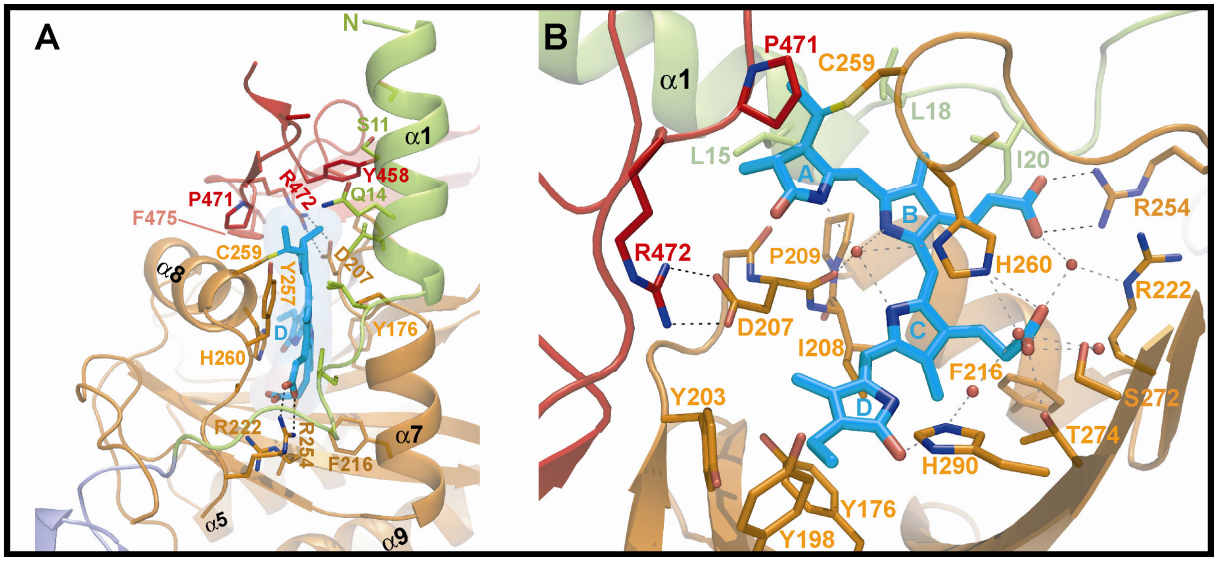

Figure 26: Tripartite binding pocket of 2VEA.
The tripartite PCB-binding pocket of Cph1 comprising the GAF-domain (orange), the tongue-like protrusion from the PHY domain (red) and the N-terminal helix α1 (green). Waters are shown as red spheres. (A) Edge-on view of the pocket highlighting the collinear arrangement of the N-terminal helix α1 and helix α7 of the GAF domain and their interaction with the chromophore and the tongue. (B) The conformation of the phycocyanobilin chromophore (cyan) within the PCB-binding site adopts a ZZZssa configuration similar to that of BV in bacteriophytochromes (31, 32). For clarity, helix α8 of the GAF domain as well as Tyr-263 and Phe-475 have been omitted. (Modified from (61))

The now completely sealed chromophore pocket thus comprises the N-terminal α1 helix, the GAF domain with the chromophore binding Cys-259 and the tongue protrusion from the PHY domain (Figure 26) (61). The helical structure of the extreme N-terminus in 2VEA was not observed in earlier bacteriophytochrome structures (30-32, 72). This could either be due to the conformational restraints arising from the binding of the chromophore to an N-terminal cysteine (98), due to crystal contacts between symmetry mates in 2VEA or due to the interaction between the N-terminal α1 helix and the tongue of the PHY domain, which is missing in the bacteriophytochrome bidomain structures. Crystallisation of Cph1Δ2 in different conditions might shed light on the true nature of the N-terminal α-helix formation.

Like plant phytochromes, Cph1 binds its chromophore to a conserved cysteine within the GAF domain (57, 89). Electron density within the chromophore pocket of 2VEA clearly shows the thioether link between the $C3^1$ carbon of PCB and the sulphur of Cys-259 (Figure 28) (61).

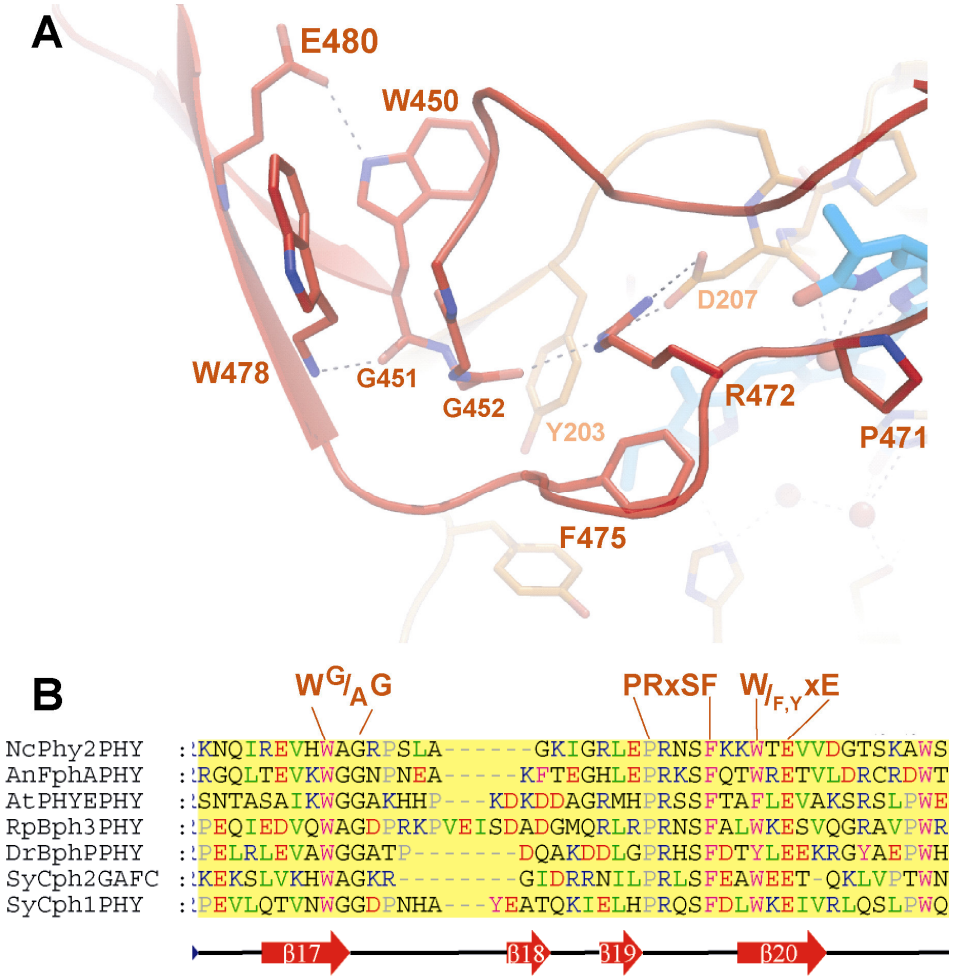

Figure 27: The tongue of Cph1Δ2 in the structure 2VEA.
(A) The kink communicates with Arg-472 within the chromophore binding pocket via hydrogen bonding to the main chain oxygen between Gly-451 and Gly-452. Another interaction between conserved tongue residues in its kink region involves Trp-450 and Glu-480. (B) The tongue sequences and the signature motifs therein. (Taken from (61))

The well resolved structure of the GAF domain and the chromophore as well as the lack of radiation damage in the pocket proves that the electron density at the chromophore attachment site indeed represents the thioether bond. Furthermore, as seen in bacteriophytochrome structures, a *ZZZssa* configuration of the chromophore is observed in 2VEA (Figure 26 and Figure 28), contradicting vibrational spectroscopy data (99) predicting a more linear *ZZZasa* conformer maybe due to *in vacuo* calculations (61).

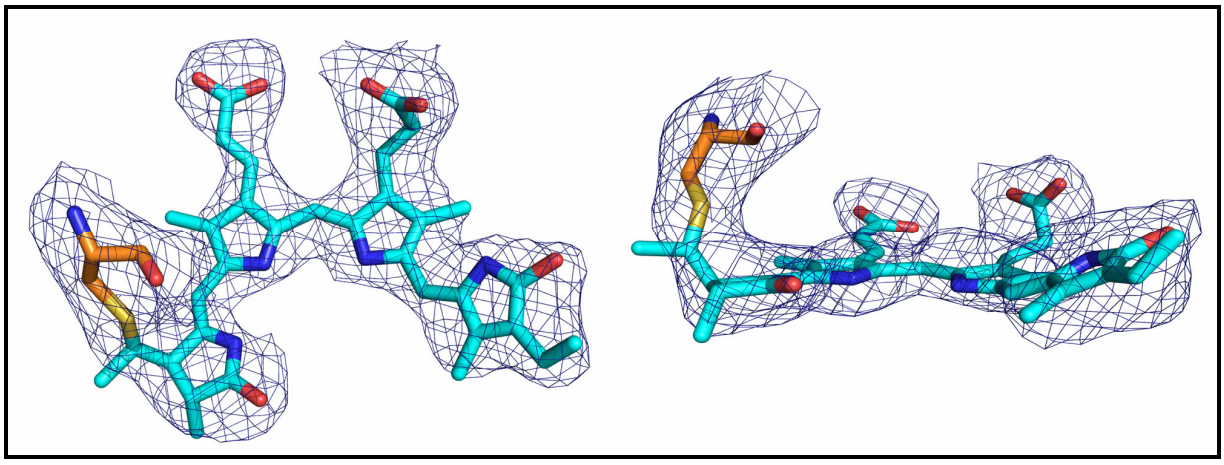

Figure 28: Omit electron density at 2σ of the adduct between the PCB chromophore and Cys-259.

As mentioned above the most prominent new structural feature of the fully resolved sensory module of Cph1 is the tongue protruding from the PHY domain which covers the chromophore pocket and contacts the N-terminal α1 helix (Figure 27). Whereas Pro-471 and Phe-475 of the conserved PRxSF motif contribute to the sealing of the chromophore pocket from outside solvent, Arg-472 interacts with Asp-207 of the GAF domain via a salt bridge (Figure 26B) (61). Asp-207 forms several hydrogen bonds to the nitrogens of the chromophore rings and also indirectly interacts with PCB through a water molecule, also seen in earlier phytochrome structures (30-32, 72).

The residues Met-174, Tyr-176, Val-186, Tyr-203, Pro-204, Tyr-263 and Met-267 surround ring D and form a subpocket, similar to bacteriophytochromes. However, the chromophore in Cph1 is less twisted than in earlier bacteriophytochrome structures perhaps due to the now sealed pocket. The tilts amount to 9.8°, 1.4° and 26.3° between rings A-B, B-C and C-D, respectively (61). Specifically ring D has a much lower inclination than reported for the bidomain structures (Figure 29B and C) that are missing the PHY domain. Stabilisation of ring D in its current configuration is ensured by H-bond formation between the carbonyl group of the chromophore and the imidazole moiety of His-290 already seen in previously published phytochrome structures. Furthermore the position of Tyr-263 seems to hinder spontaneous rotation of ring D implying that a certain amount of energy is necessary for C15=C16 isomerisation of the chromophore. In the bidomain structures of bacteriophytochromes, the hydroxyl group of Tyr-263 is closer to the carboxyl moiety of Asp-

207 due to the lack of the PHY domain and thus leaving more space in the chromophore pocket for ring D to rotate which would explain the 40 – 50 ° inclination of the latter (Figure 29C). In 2VEA, Asp-207 forms a salt bridge with Arg-472 of the tongue, resulting in Tyr-263 moving closer to the ring D of the chromophore (Figure 29B) (61).

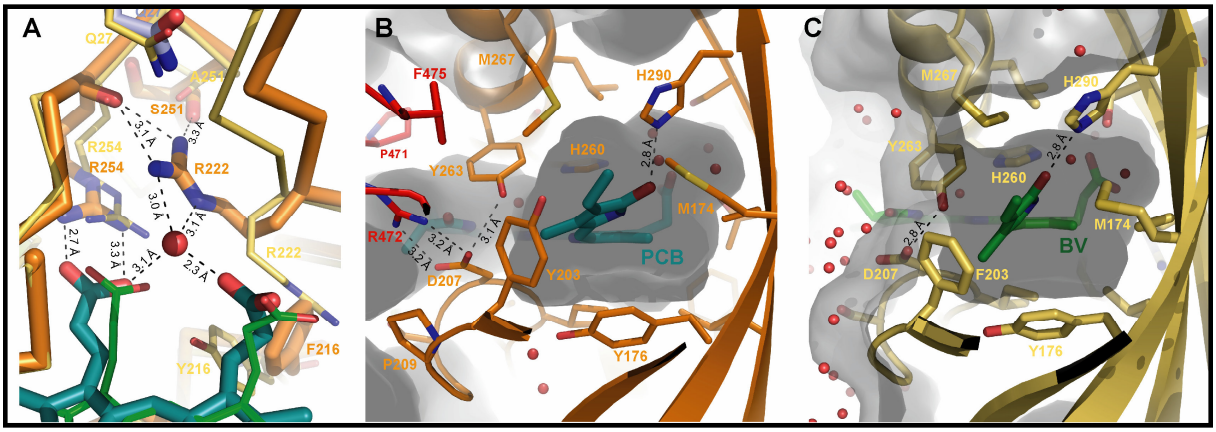

Figure 29: Comparisons of the chromophore pocket in Cph1Δ2 and bacteriophytochrome
Comparisons of the chromophore pocket in Cph1 (orange) and bacteriophytochrome (yellow) (31) with their respective chromophores PCB (cyan) and biliverdin (green). Waters are shown as red spheres. (A) The subsite for interactions between the bilin propionate groups and the GAF domain, showing the different conformations adopted by Arg-222 and Phe/Tyr-216 in Cph1 and bacteriophytochrome. (B) and (C) The ring D microenvironment in Cph1 and bacteriophytochrome, respectively. The molecular surfaces of the proteins (grey) show similar cavities with a triangular cross section providing space for the Z→E photoflip. The chromophore is sealed off from the solvent in the case of the Cph1 complete sensory module, while the bacteriophytochrome bidomain pocket is open to the solvent (note the numerous waters). (Taken from (61))

Another notable difference between the bidomain structures and 2VEA concerns the relocation of Arg-222 and Phe-216 in the vicinity of the ring C propionate side chain (Figure 29A). Whereas Arg-222 points away from the propionate side chains in 1ZTU, the guanidinium moiety interacts via a water molecule with both carboxylate groups in 2VEA. Phe-216 takes up the space in Cph1, which Arg-222 occupies in DrBphP1. This difference might result from the hydroxyl group of Tyr-216, conserved among biliverdin binding phytochromes, whereas in plant-like phytochromes and Cph1 a phenylalanine is found at this position. The salt bridge between Arg-254 and the ring B propionate side chain is conserved among all current phytochrome structures in their Pr state, implying that this interaction might not only constitute an anchor for the stabilisation of the chromophore in the pocket, but might very well contribute to the signalling route of phytochromes from the chromophore to the protein and finally to the transmitter module (61). The photoisomerisation of the D-

ring from Pr to Pfr might trigger a rearrangement of the propionate side chains which then interact with different partners thus changing the overall protein structure. In the case of the Cph1 sensory module the propionate side chain of ring B might reorient its interaction from Arg-254 to Arg-222 similar to a proposed mechanism in oxygen sensors (100). The position of the C ring propionate in 2VEA is slightly different as seen in the bidomain structures of bacteriophytochromes and interacts via hydrogen bonds and waters with Ser-272 and Thr-274. Like in the case of the propionate side chain of ring B, this interaction might also be involved in the signalling mechanism.

The complete sensory module of Cph1, as seen in the crystal structure, is able to photoconvert from Pr to Pfr unlike bacteriophytochrome bidomains which are not able to form stable Pfr states (30, 36). Cryo-protected crystals mounted under IR light showed a similar absorbance spectrum at 100 K to Cph1Δ2 in solution at 298 K (Figure 30A) (61, 62).

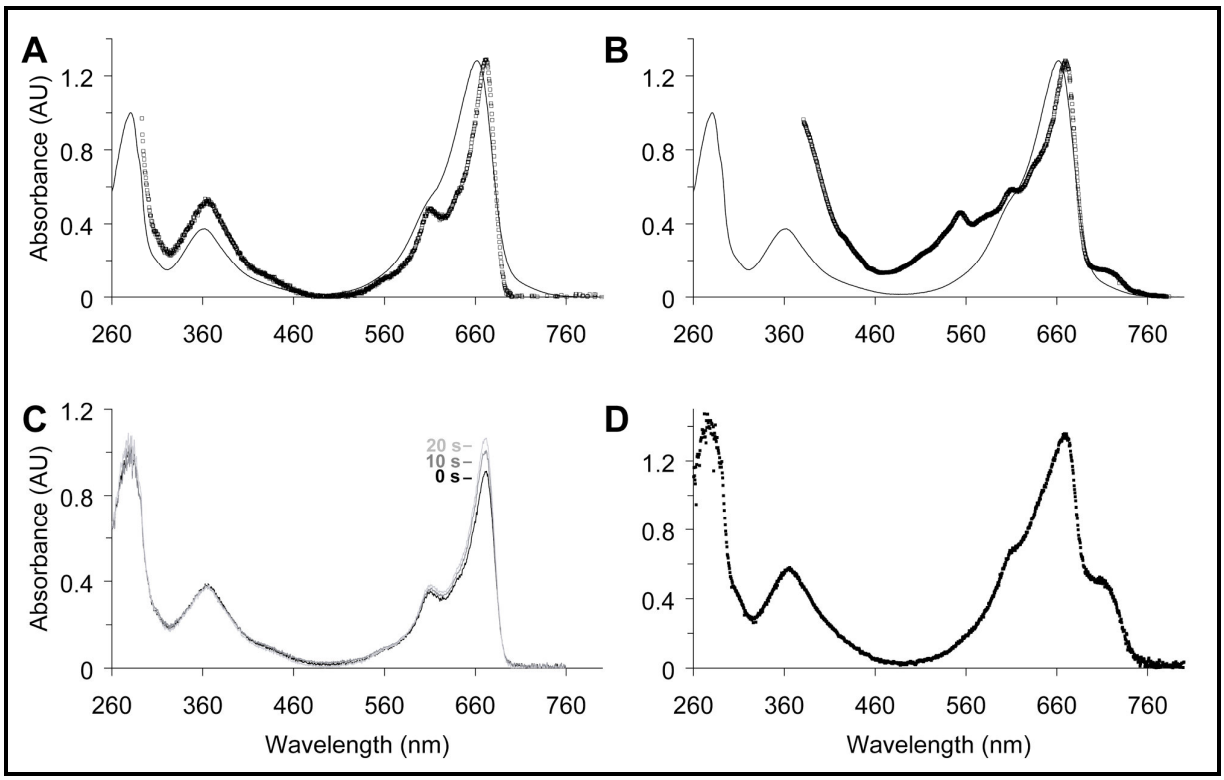

Figure 30: Absorbance spectra of the Pr state of Cph1Δ2 in solution and crystalline form.
Absorbance spectra of the Pr state of Cph1Δ2 in solution (-) and crystalline form (□) and X-ray diffraction patterns. (A) Spectrum of crystals harvested from 1.8 M sodium acetate and 0.1 M sodium acetate pH 4.6 (overall pH 6.5) recorded before X-ray irradiation. (B) Spectrum of crystals harvested from 2.3 M sodium acetate and 0.1 M sodium acetate pH 4.4 (overall pH 6.5) recorded after 18 hours X-ray irradiation at beamline X-13 (EMBL Hamburg). (C) Spectrum of crystals prior to, after 10 s and after 20 s cryo-annealing in darkness. (D) Absorbance spectrum of Cph1Δ2 crystals exposed to white light prior to freezing. (Taken from (62))

The main differences are the 10 nm bathochromic shift of the red λ_{max} band as well as formation of distinct peaks from the shoulder at 600 nm due to a narrowing of the peaks. The absorbance spectrum of the crystal used for data collection, after 18 hours continuous X-ray irradiation (flux: $3.16 \cdot 10^{11}$ photons $\cdot s^{-1}$), displayed the same red shifted Pr peak albeit a minor Pfr-like peak is observed at 715 nm (Figure 30B). This small peak might result from slight movements of the chromophore due to prolonged exposure to X-rays inducing radiation damage, which is also reflected in the aberrant shoulder of the Pr peak resulting in. Flash cryo-annealing in darkness to improve the diffraction of the Cph1 crystals did not shift the absorbance spectra (Figure 30C). Irradiating the crystals with white light before freezing them in liquid nitrogen led to partial Pfr photoconversion, which could also be obtained by irradiation of the crystals at 20 °C with an intense red laser (Figure 30D and Figure 31). Both treatments resulted in a complete loss of diffraction, thus structural data of the Pfr state could not be obtained with these crystals (61, 62).

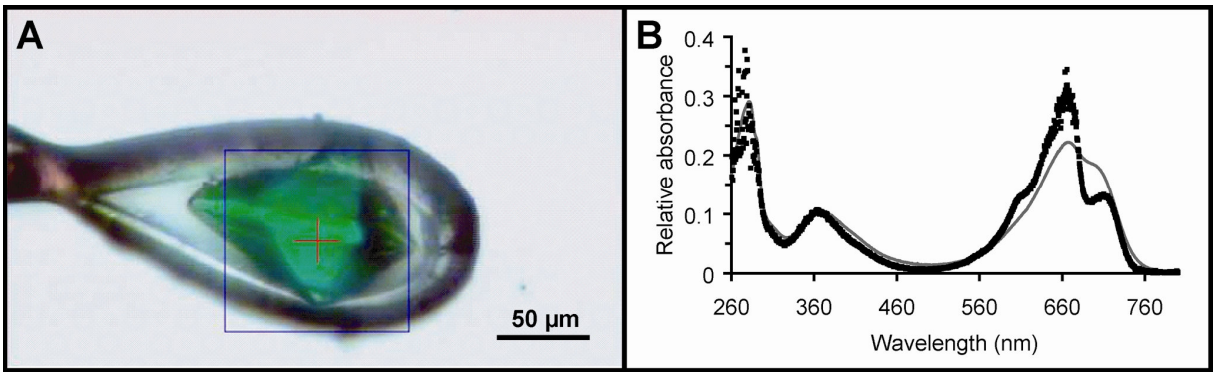

Figure 31: Cph1Δ2 crystal (A) and spectrum (B) after irradiation with red light.
(A) The Cph1Δ2 crystal was fixed in a cryo-loop and rotated during irradiation. (B) Absorbance spectra of the Pr state of Cph1Δ2 in solution (-) and crystalline form (□). (Based on (61))

3.4.2. Crystallisation and structural characterisation of Y263F

Initial crystals appeared in a condition containing 200 nl of 10 mg / ml Y263F Pr and 200 nl reservoir solution (2.5 M sodium acetate and 0.1 M MES, pH 6.5) (Anions suite, Qiagen) (Figure 32) (79). Further optimisation was done by hanging-drop vapour diffusion using 1 µl of 10 mg / ml Y263F Pr and 1µl reservoir solution to increase the size of the crystals. Optimally-diffracting crystals were obtained in a condition containing 1.9 M sodium acetate

and 0.4 M MES pH 7.2. 30 % glycerol was added as a cryo-protectant and crystals were frozen in liquid nitrogen using 1.75 M sodium acetate, 0.2 M MES, pH 7.2, and 30% glycerol.

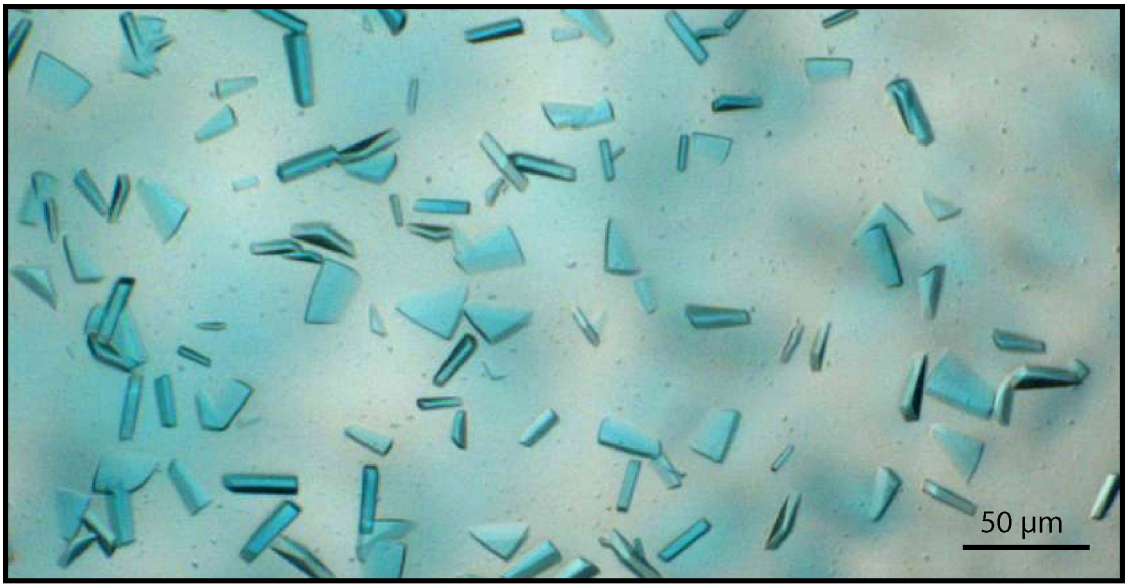

Figure 32: Crystals of Y263F in the Pr state.

Datasets were collected at beamline ID14-2, ESRF, Grenoble. The completeness of the 1.95 Å dataset was 99.8 % and revealed the monoclinic space group C2 (a=107.57 Å, b=95.15 Å, c=73.58 Å, β=99.67°) with one molecule per asymmetric symmetry unit. Molecular replacement by PHASER (101) was performed with the photosensory module of wild type Cph1 (PDB code 2VEA) for the PAS-GAF bidomain and the PHY domain independently, followed by alternating cycles of automated and manual refinement using REFMAC5 (87, 102) and COOT (88) in collaboration with Prof. Lars-Oliver Essen. The final model of Cph1-Y263F photosensory module converged at R-factor / R-free of 18.4 % / 22.3 % (Table 9 in appendix 11.4.3) and is structurally defined from Ala-2 to His-518 (79).

Y263F did not crystallise under the same conditions as wild type Cph1Δ2, but instead needed MES buffer at the same pH to crystallise. The new, monoclinic crystal form found for Y263F has one molecule per asymmetric unit and diffracted isotropically to 1.95 Å resolution (Figure 33A). The improved diffraction characteristics of Y263F might derive from either packing differences resulting from slight changes in the quaternary structure or improved homogeneity of the material (61). At 1.95 Å resolution, acetate and glycerol molecules as well as sodium ions could be identified in the crystal structure with an acetate and a phosphate close to the chromophore pocket. A possible effect of these molecules on the photoconversion

mechanism is improbable as they were not found in other phytochrome crystal structures. The refined structure of Y263F (PDB code 3ZQ5) has a significantly lowered overall temperature factor (28 Å²) than the wild type (66 Å²) (79).

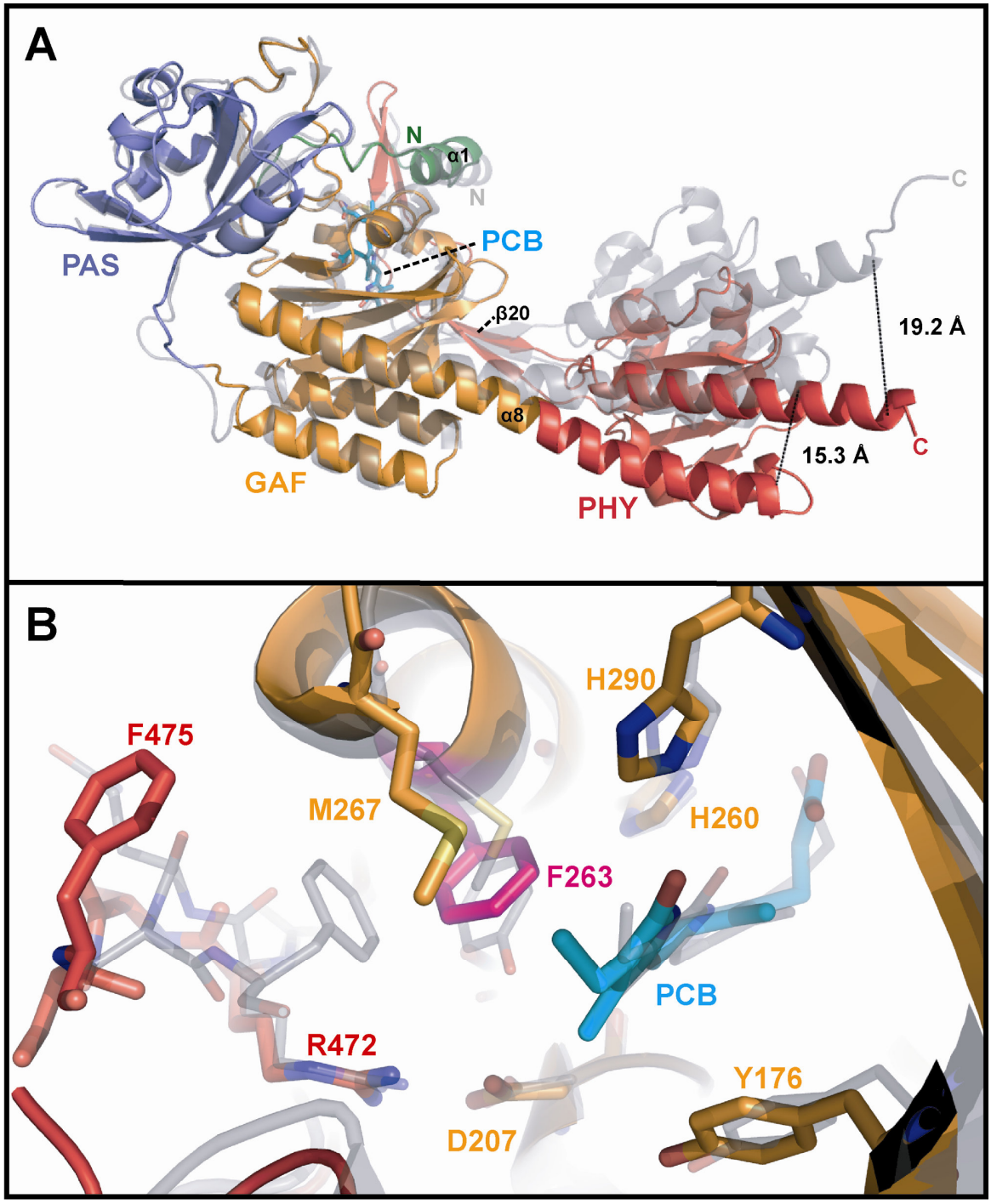

Figure 33: Superimposition of the Y263F mutant and the Cph1 wild type in their Pr states.
Superimposition of the overall structure (A) and the chromophore pocket (B) of the Y263F mutant (coloured) and the Cph1 wild type (grey) in their Pr states. In the Y263F structure the PHY domain is shifted by 17° in relation to the PAS-GAF bidomain. Due to the Y263F substitution, the D-ring of the chromophore is inclined further, which in turn requires a rearrangement of conserved residues (Met-267 and Phe-475) in its vicinity.

The improved electron density not only allowed allocation of almost all residues in the structure thus closing the gaps (Gln-73–Glu-80 and Gly-100–Asp-101 in the PAS domain, Arg-148–Gln-150 in the GAF domain and Ala-460–Lys-466 at the tip of the tongue of the PHY domain) unresolved in the wild type structure, but also led to the identification of alternative side chain conformations (Figure 33B) and several water molecules close to the protein. The overall structure of the photosensory module Y263F is similar to that of the wild type (Figure 33A), showing an N-terminal PAS-GAF lobe separated from the C-terminal PHY domain by the long linker helix α9 (Pro-298–Thr-344). Y263F crystallised as an antiparallel dimer with the same dimerisation surface as seen for wild type Cph1 (Figure 34). 2VEA and 3ZQ5 are the only structures published to date, that do not crystallise as parallel dimers (79).

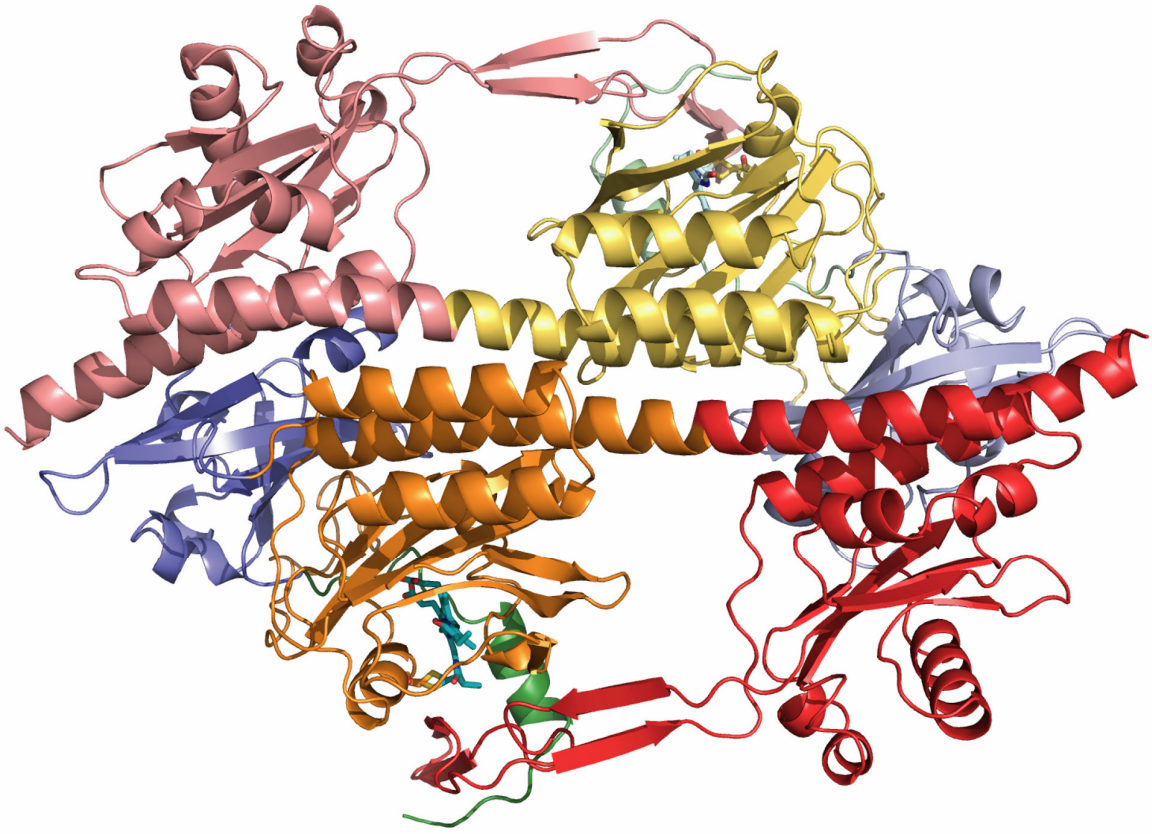

Figure 34: Y263F antiparallel dimer as defined by crystal symmetry.

The structures of the individual lobes are very similar, yielding low r.m.s.d. values following superimposition of 0.36 Å and 0.32 Å for the PAS-GAF (231 Cα positions) and PHY (133 Cα positions) lobes, respectively (79). The Y263F dimer interface along the linker helix α9 and the accompanying helix α4 from the PAS domain overall resembles that of the wild type

(differences are detailed in Figure 35 and Table 5) with interface areas of 1205 and 1239 Å^2 for the wild type and Y263F, respectively.

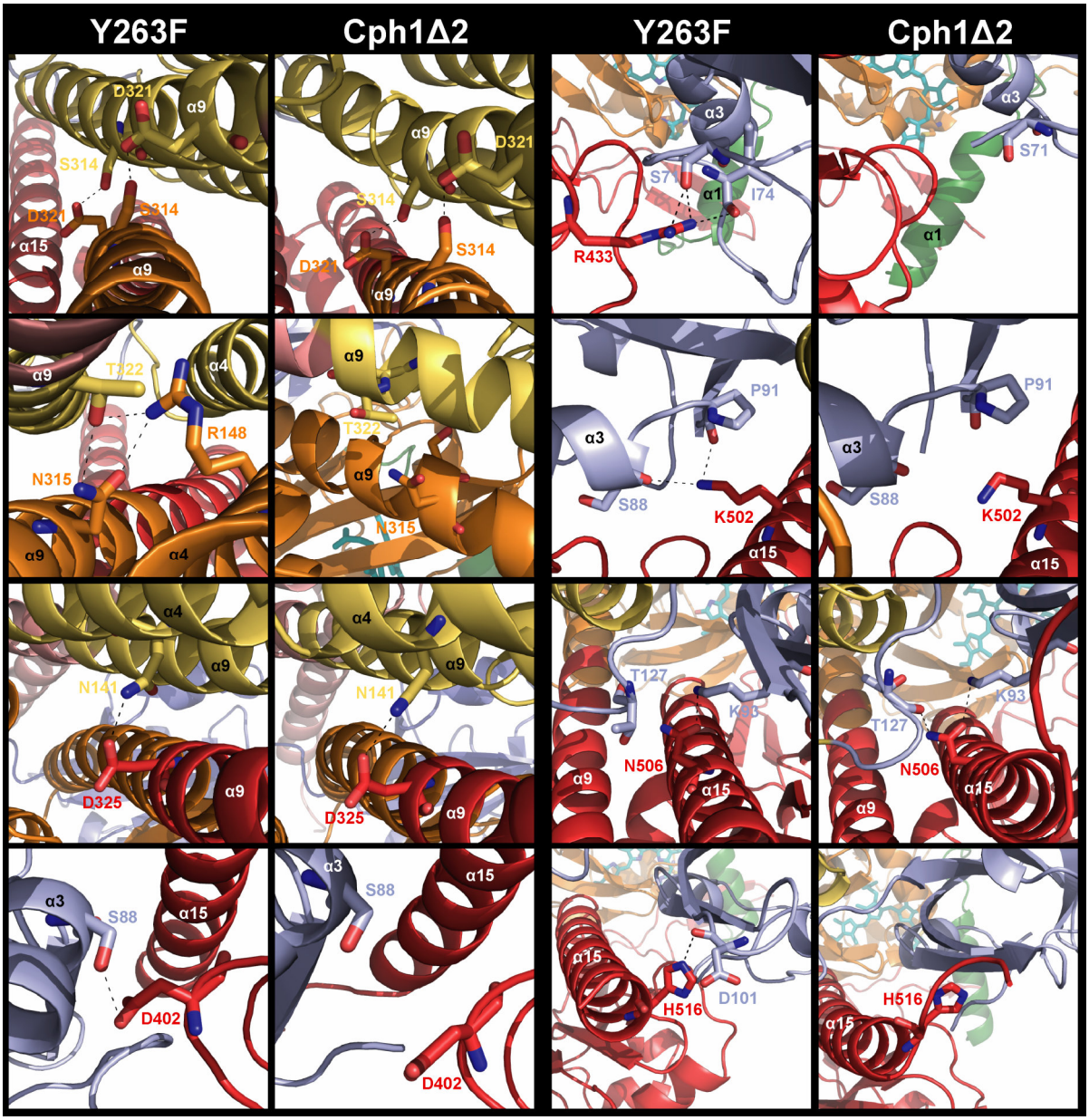

Figure 35: Interactions between the crystallographic dimer subunits of Cph1Δ2 and Y263F.
Direct (residue-residue) interactions (Table 5) between the crystallographic dimer subunits of Cph1Δ2 wild type and Y263F within 3.5 Å (dashed lines).

As expected, the overall structure of Y263F does not deviate considerably from the wild type - neither the PAS-GAF interface nor the light-sensing knot is affected by the Y263F substitution. Considerable changes in residue – residue interactions are almost exclusively found at the surface of the protein, the side chains within the chromophore pocket only display minor variations, probably due to the improved electron density and not resulting from the Y263F substitution. By comparing the almost identical structures (2VEA and 3ZQ5),

two hinge regions within the α9 helix could be identified; Ile-316–Ser-317 and Val-329–Gln-330, located close to the domain surfaces of the GAF and PHY domain, respectively (Figure 36A and C) (79). Slight differences at the Ile-316–Ser-317 hinge induce a straightening of the α9 helix in the Y263F structure, thus resulting in a 17° offset for the PHY domain. Due to this straightening, molecular replacement with the complete photosensory module of wild type Cph1 was not possible at first, but by removing the α9 helix and separating 2VEA in its respective PAS-GAF and PHY domains, molecular replacement with independent domains proved to be successful.

Table 5: Interactions between the crystallographic dimer subunits of Cph1Δ2 and Y263F.

wt Cph1Δ2 (2VEA)			
Subunit 1	**Subunit 2**	**Distance (Å)**	**Bond type**
Arg-97	Ala-512	3.81	H
Asp-102	His-518	2.80	H / S
Thr-127	Asn-506	2.62	H
Ser-128	Glu-513	3.57	H
Asn-141	Asp-326	3.33	H
Asp-280	Arg-310	3.64	H / S
Arg-310	Asp-280	3.64	H / S
Ser-314	Asp-321	2.62	H
Asp-321	Ser-314	2.62	H
Asp-326	Asn-141	3.33	H
Asn-506	Thr-127	2.62	H
Ala-512	Arg-97	3.81	H
Glu-513	Ser-128	3.57	H
His-518	Asp-102	2.80	H / S

Y263F (3ZQ5)			
Subunit 1	**Subunit 2**	**Distance (Å)**	**Bond type**
Ser-71	Arg-433	2.79	H
Phe-72	Arg-433	2.97	H
Ile-74	Arg-433	3.41	H
Ser-88	Lys-502	3.37	H
Lys-93	Asn-506	2.53	H
Asp-101	His-516	2.65	H
Ala-125	Arg-510	3.74	H
Asn-141	Asp-326	2.82	H
Arg-148	Gln-319	2.34	H
Arg-148	Thr-322	3.45	H
Ser-314	Asp-321	2.59	H
Asn-315	Thr-322	3.00	H
Gln-319	Arg-148	2.34	H
Asp-321	Ser-314	2.59	H
Thr-322	Arg-148	3.45	H
Thr-322	Asn-315	3.00	H
Asp-326	Asn-141	2.82	H
Arg-433	Ser-71	2.79	H
Arg-433	Phe-72	2.97	H
Arg-433	Ile-74	3.41	H
Lys-502	Ser-88	3.37	H
Asn-506	Lys-93	2.53	H
Arg-510	Ala-125	3.74	H
His-516	Asp-101	2.65	H

Although the PHY domain is shifted in relation to the larger lobe comprising the PAS and GAF domains, the protruding tongue still effectively seals the chromophore pocket. Two

hinges, Gly-451–Gly-452 and Trp-478–Lys-479, make sure that the tongue still interacts with the GAF domain and the N-terminal extension by adopting different main chain conformations (Figure 36B). The hinges correspond to the highly conserved WGG and WxE motifs, implying that they might play a role in the photoconversion mechanism (79).

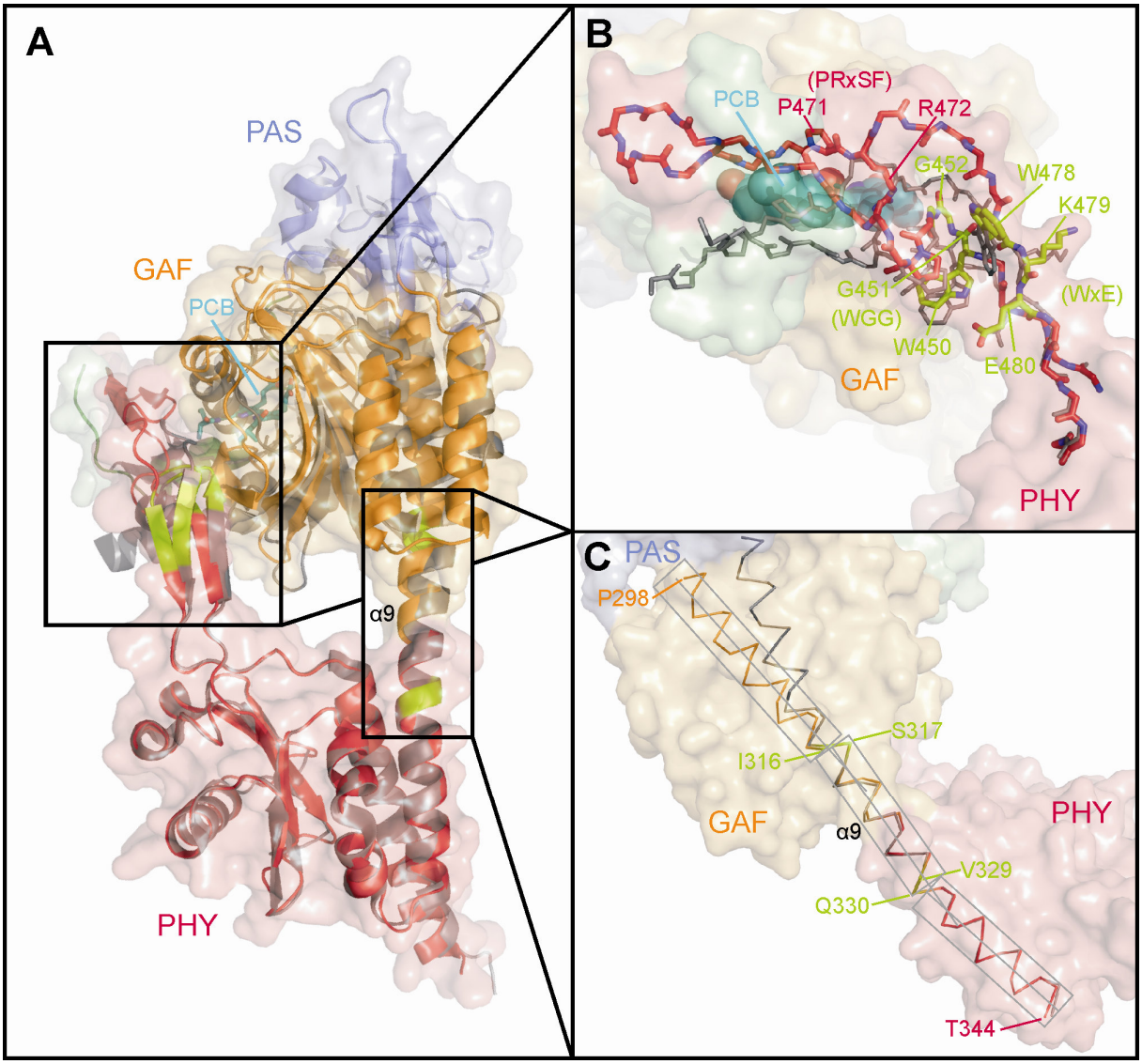

Figure 36: Superposition of the PHY domains of 3ZQ5 and 2VEA, respectively.
(A) Conformational differences between the wild type (2VEA, grey) and Y263F (3ZQ5, coloured) structures by superposition of the respective PHY domains highlighting hinges (green) in the tongue and α9 helix. (B) The tongue, complete in 3ZQ5, and its hinges at W478-K479 and G451-G452. (C) The linker helix kinks are 8° and 12° at the I316-S317 and V329-Q330 hinges, respectively.

A similar heterogeneous alignment of the α9 helix is observed in the structures (3C2W, 2G6O) of the photosensory module of bacteriophytochrome PaBphP (72, 90), implying that the flexibility of the α9 helix is not restricted to mutations within a single phytochrome

species; indeed a shift of the PHY domain might be connected to the signalling mechanism of phytochromes.

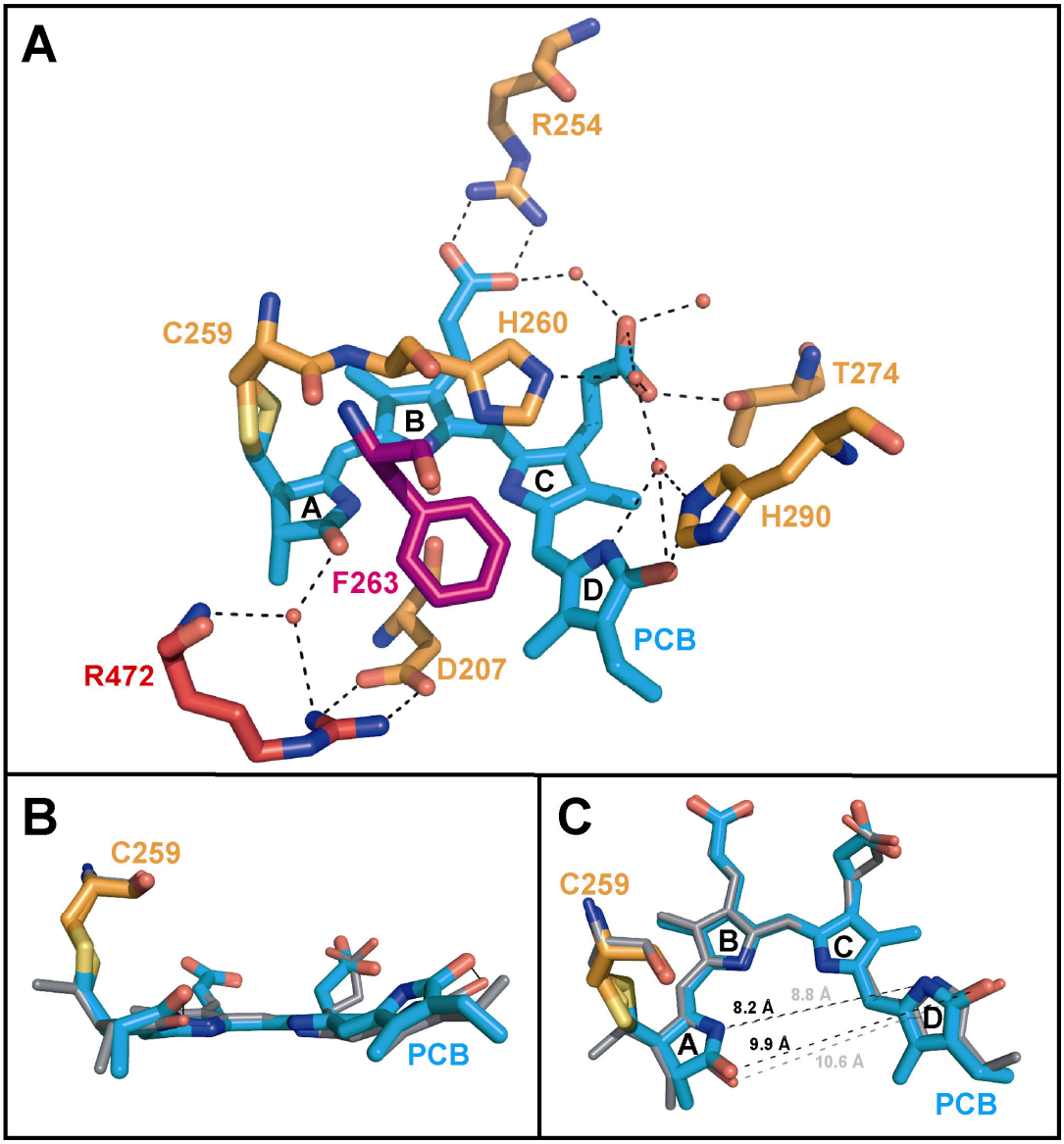

Figure 37: 3D structure of PCB and its interacting residues in the Y263F structure.
(A) High resolution 3D structure of the PCB chromophore (cyan) and its interacting residues. The substituted residue Y263F is shown in magenta. (B and C) Conformational differences between the Y263F (cyan) and wild type (grey transparent) structures lead to a 1 Å constriction of the chromophore.

The loss of the hydroxyl group in Y263F induces only small changes in the chromophore configuration (Figure 37). Overall, the PCB chromophore is slightly more twisted than in the wild type. The D ring is more inclined (37° vs. 26°) but still interacts via hydrogen bonds to His-290 and the water network between ring C and D (79).

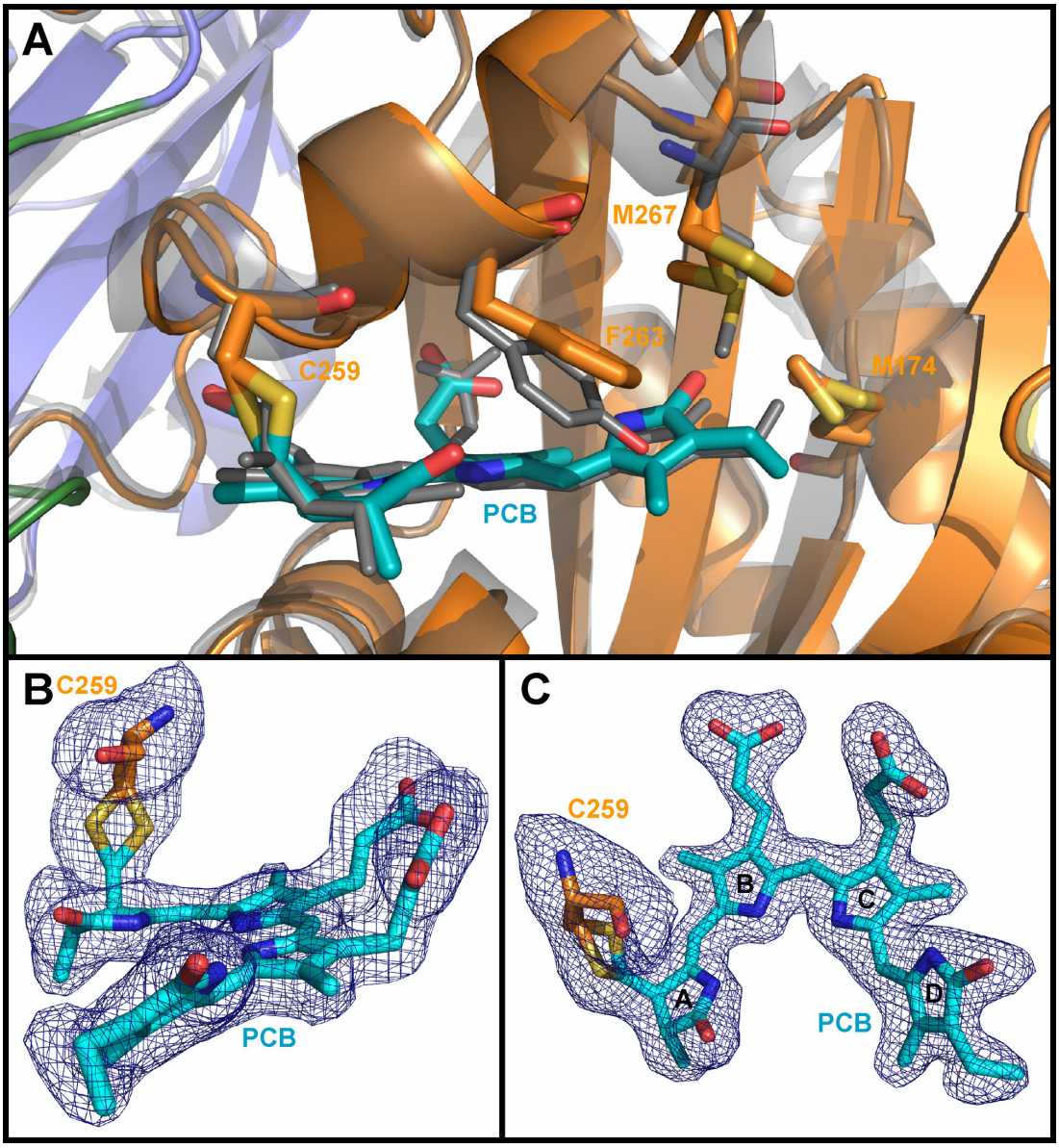

Figure 38: View of the chromophore pocket detailing the variability of the thioether link.
(A) Superimposition of the chromophore pocket of the Y263F mutant (coloured) and the Cph1 wild type (grey) in their Pr states with the thioether linkage between Cys-259 and the chromophore, Met-174 and Met-267 showing two different conformations. Side (B) and top (C) view of the omit electron density of the adduct between the PCB chromophore and Cys-259 contoured at 2σ showing the two possible conformations of the linkage.

The angles between rings B and C are slightly larger (5.8° vs. 1.5°) compared to the chromophore in 2VEA. Interestingly, the side chain of the C ring propionate points towards Thr-274, thereby losing its direct polar contacts with His-260, which is the same situation as in the 1ZTU bidomain structure of the bacteriophytochrome DrBphP1 (Figure 29A, Figure 37 and Figure 38). On the other hand, the C ring propionate still retains its salt bridge with Arg-254, reinforcing the assumption that this interaction might play a major role in the signalling mechanism. The inclination of the A ring is also steeper (16° vs. 10°) with its carbonyl group

pointing upwards and hydrogen-bonding to the guanidinium moiety of Arg-472 via a water, not apparent in previously published structures of Cph1 and other bacteriophytochromes (79). The Cys-259 thioether connecting the chromophore to the peptide chain shows two distinct conformations in the high resolution structure. Furthermore, two methionines Met-174 and Met-267 located near the D ring of the chromophore show two alternative rotamers (Figure 38).

The main peak of the UV-Vis absorbance spectra of Y263F Pr crystals kept at 100 K was red-shifted relative to the spectra in solution at room temperature and the red band shoulder displayed distinct minor peaks, which were already apparent in wild type crystals (Figure 30A and Figure 39) (79). *In situ* photoconversion to the Pfr state was possible for small crystals (Figure 39), but resulted in a loss of diffraction, as observed for the wild type (61, 62).

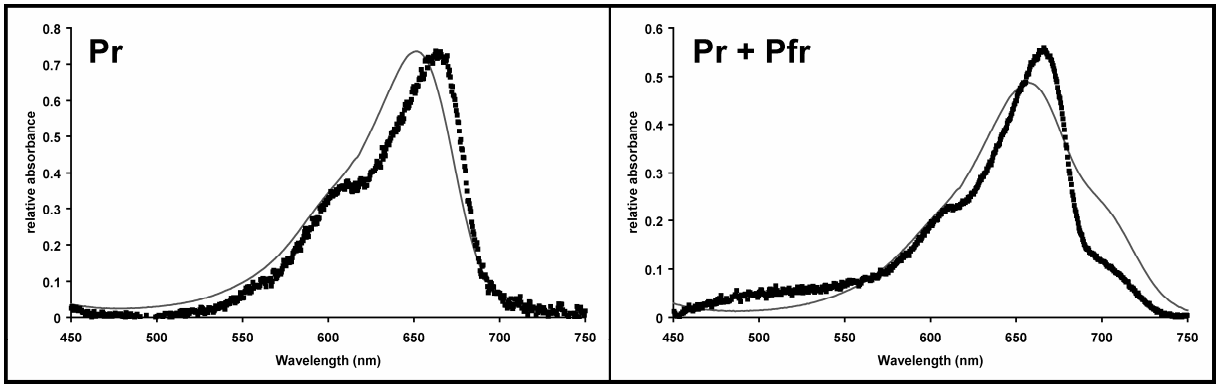

Figure 39: Absorbance spectra of Y263F in solution and in crystalline form.
UV/Vis spectra of Y263F in solution at room temperature (grey line) and in crystalline form at 100 K (▪) in the Pr ground state (left) and after red irradiation (right). In solution, the mole fraction of Pfr at photoequilibrium is ~50 % whereas <20 % is converted to the Pfr state in the crystal.

3.4.3. Crystallisation and structural characterisation of Y176H

Blue rod-shaped crystals appeared in a condition containing 200 nl of 10 mg / ml Y176H Pr and 200 nl reservoir solution (1.0 M ammonium sulphate, 0.1 M HEPES sodium salt, pH 7.5 and 1 % (v/v) PEG 400) (Classics suite, Qiagen) after 6 – 8 weeks (Figure 40). Further optimisation by hanging drop vapour diffusion method proved difficult due to slow crystal growth. 30 % glycerol was added as a cryo-protectant and crystals were frozen in liquid nitrogen using 0.7 M ammonium sulphate, 0.07 M HEPES sodium salt, pH 7.5 and 0.7 % (v/v) PEG 400 and 30% (v/v) glycerol. Datasets were collected at beamline ID23-2, ESRF, Grenoble.

Two datasets diffracting to 3.5 Å with 100 images each were collected, but prolonged X-ray radiation had a severe impact on the crystals and diffraction deteriorated quickly. The completeness of the first dataset was 81.2 % and revealed the tetragonal space group P4 (a = b = 137.94 Å, c= 357.94 Å, α = β = γ = 90°) with twelve molecules per asymmetric symmetry unit. The completeness of the second dataset was even lower with 64.1 % due to the degradation of the crystal. Due to the low quality of the integrated dataset, molecular replacement was neither possible with the Cph1Δ2 nor the Y263F structure. Data collection statistics are detailed in Table 10 in the appendix 11.4.4. Further crystallisation conditions were found in the basic screens, but the crystals could not be reproduced (Figure 40C and D).

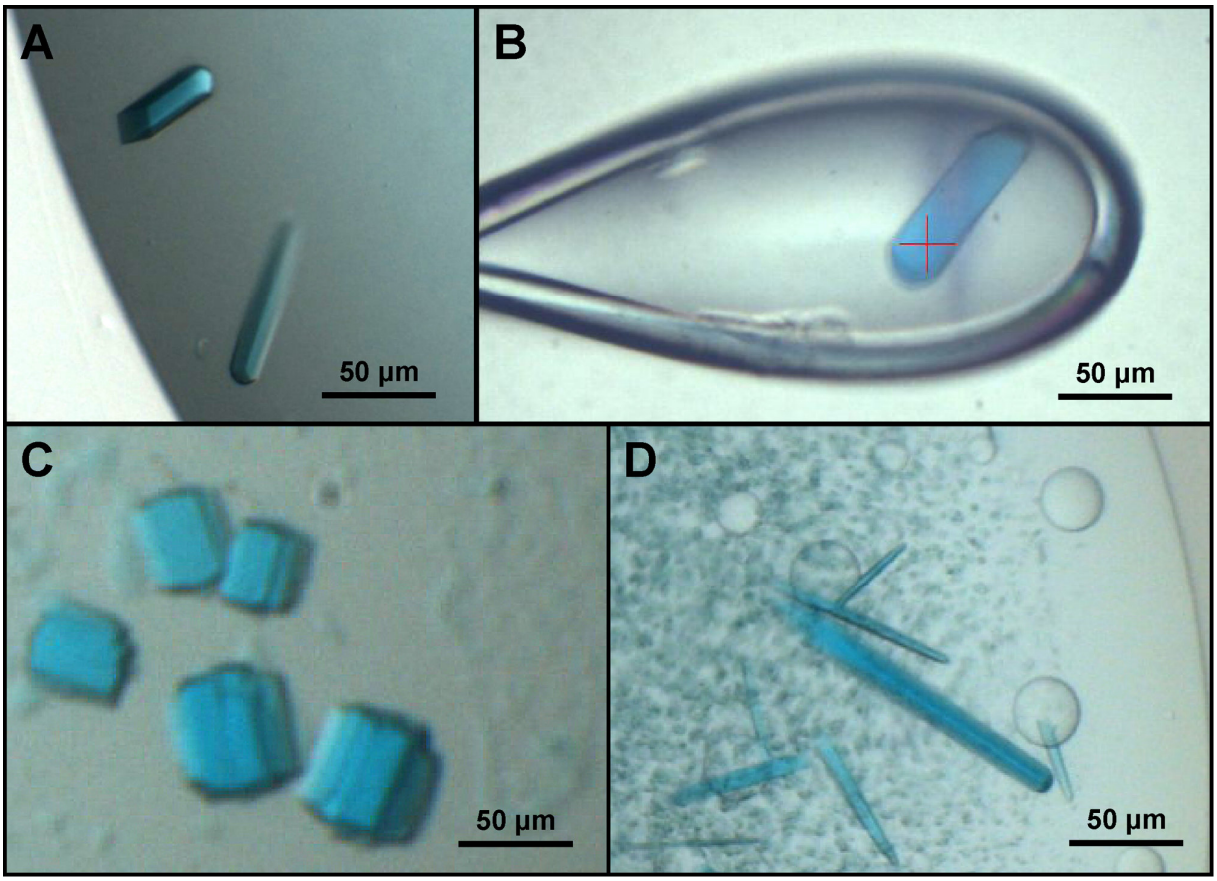

Figure 40: Crystals of Y176H in their locked Pr state.
Y176H crystals from (A) were optimized and subjected to X-Ray diffraction analysis (B). Crystals from (C) and (D) could not be reproduced.

3.4.4. Further crystallisation efforts

In vitro assembled Cph1Δ2 failed to crystallise in the same conditions as *in vivo* assembled phytochrome, implying structural differences present on the surface of the protein. Blue-green rhombohedral crystals in a condition containing 1 µl of 10 mg / ml *in vitro* assembled Cph1Δ2 in its Pr state and 1 µl reservoir solution (1.0 M ammonium dihydrogenphosphate and 0.1 M sodium citrate, pH 5.6) (Basic kit, Sigma-Aldrich) (Figure 41A). Reproduction of the crystals in the same condition was not possible and obtained crystals dissolved upon cryo-protection in a variety of buffers.

On the other hand S11A crystallised in identical conditions as *in vivo* assembled Cph1Δ2, implying that the mutation does not have any notable effect on the structure. Blue-green crystals having the same shape and form appeared within two weeks (Figure 41B), but structure solution of this mutant was not attempted as the structure is probably identical to 2VEA.

Pale-blue crystals of D207S appeared in a condition containing 1 µl of 10 mg / ml D207S in its Pr state and 1 µl reservoir solution (1.36 M ammonium sulphate, 8.5 % (v/v) dioxane, 15 % (v/v) glycerol and 0.085 M MES, pH 6.5) (Cryo suite, Qiagen) (Figure 41C). Crystals were too small to be characterised further and optimisation of the crystallisation conditions is still ongoing.

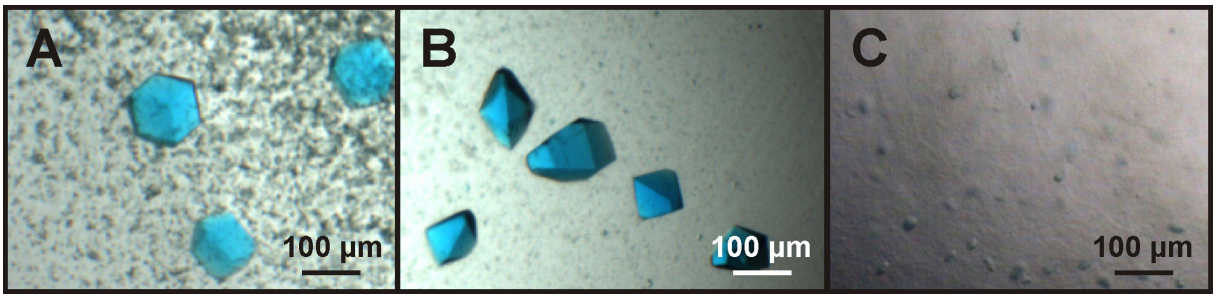

Figure 41: Crystals of in vitro assembled Cph1Δ2 (A), S11A (B) and D207S (C).

Crystallisation attempts with *in vitro* assembled R254A, *in vivo* assembled S251A and T274A in their respective Pr and Pfr states at almost 100 % occupancy, obtained by SEC, did not yield any crystals.

4. Discussion

The complete structure of the sensory module of Cph1 in the Pr state gives new insights into the residues involved in the photoconversion mechanism and the signalling pathway of phytochromes in general. Mutational analysis of conserved amino acids within the sensor module of canonical phytochromes helped to determine the role of these residues in the photochemistry of phytochromes. Four main issues will be elucidated and discussed: a) the photoconversion mechanism involving the isomerisation of the D-ring, b) the transmission of the signal from the chromophore to the protein, c) its implications on the structure of the photoreceptor and d) the heterogeneity of the Pr state.

4.1. Photoconversion mechanism

To be able to form a basis for a photoconversion mechanism, the configuration of the chromophore for both the Pr and Pfr states needs to be determined first. All crystallographic structures to date show that the Pr state of the chromophore is in a periplanar *ZZZssa* conformation (30-32, 61, 79, 91), which are confirmed by both the wild type Cph1Δ2 and Y263F structures, whereas the Pfr state of bathy-phytochromes shows a *ZZEssa* configuration (72, 90). Former vibrational spectroscopic analyses suggested a *ZZZasa* configuration for the Pr state of plant phytochromes (33, 99, 103, 104), but interpretation of these results were revised by QM/MM calculations (105). Furthermore, recent MAS-NMR studies (60) have reaffirmed *ZZZssa* and *ZZEssa* as the Pr and Pfr conformations, respectively. However, NMR studies of the isolated GAF domain of the PAS-less SyB (Figure 1) implied that Pr → Pfr photoconversion involved isomerisation of the A ring (106) instead of the D ring. Spectroscopic and structural analyses strongly suggest that the PHY domain and most importantly the tongue is necessary for efficient Pr → Pfr photoconversion of canonical phytochromes (30, 61), whereas the GAF construct of SyB-Cph1 seems to form stable Pfr without either PAS or PHY domains present (107). Furthermore RR studies showed that the GAF construct of SyB lacks a prominent Pfr peak around 810 cm^{-1}, corresponding to the C-H out-of-plane mode of the C-D methine bridge (33), seen in canonical phytochromes (108). It

should also be noted that the rotamers of several side chains near ring D are similar in the SyB-Cph1 (GAF) ensembles for Pr and Pfr, whereas the crystal structures of Cph1Δ2 and PaBphP (61, 72, 90) show consistent state-related differences. It would thus seem that SyB-Cph1 functions quite differently from canonical phytochromes.

After having established that the first photochemical event involves a C15=C16 isomerisation of the D ring of the chromophore from the *ZZZssa* Pr to the *ZZEssa* Pfr configuration the question now arises, which residues are involved in the photoconversion mechanism. Comparing the chromophore pockets surrounding the D-ring of 2VEA and 3C2W in their Pr and Pfr states, respectively, several changes in the interaction between the chromophore and conserved residues are displayed (Figure 42). In the Pr ground state of the cyanobacterial phytochrome Cph1, the D ring hydrogen bonds with the conserved His-290 via its carbonyl group, the three tyrosines Tyr-176, Tyr-203 and Tyr-263 surrounding and shielding the chromophore from outside solvent. In the Pfr ground state of the bathy-phytochrome PaBphP, the D ring is stabilised by several hydrogen bonds to Gln-188 (not conserved among phytochromes) and Asp-207 (from the conserved DIP motif). The hydrogen bond between Ser-459 (Ser-474 in Cph1) from the conserved PRxSF motif and Tyr-250 (Tyr-263 in Cph1) and its relocation within the chromophore pocket provides ample space for the D ring rotation. Furthermore Tyr-163 (Tyr-176 in Cph1) and Tyr-190 (Tyr-203 in Cph1) undergo a rotamer change with Tyr-163 stabilising the C ring propionate via a hydrogen bond to its hydroxyl group. Thus, it has been suggested that this tyrosine flipping mechanism is triggered by light-induced isomerisation of the D ring, providing additional stability in both Pr and Pfr states (72). Whether this proposed photoconversion mechanism can be applied to phytochromes in general is doubtful as it fails to explain two important observations: Firstly, Cph1 undergoes a CD signal switch upon photoisomerisation; whereas the Pr state of Cph1 exhibits a negative CD signal for the red absorbance band, Pfr displays a positive peak. On the other hand, bacteriophytochromes like DrBphP1 show a negative CD for the red absorbance band in both states, with the Pfr having a weaker signal. It has been suggested that these differences might reflect the facial disposition of the D ring relative to the co-planar B and C rings (17, 26).

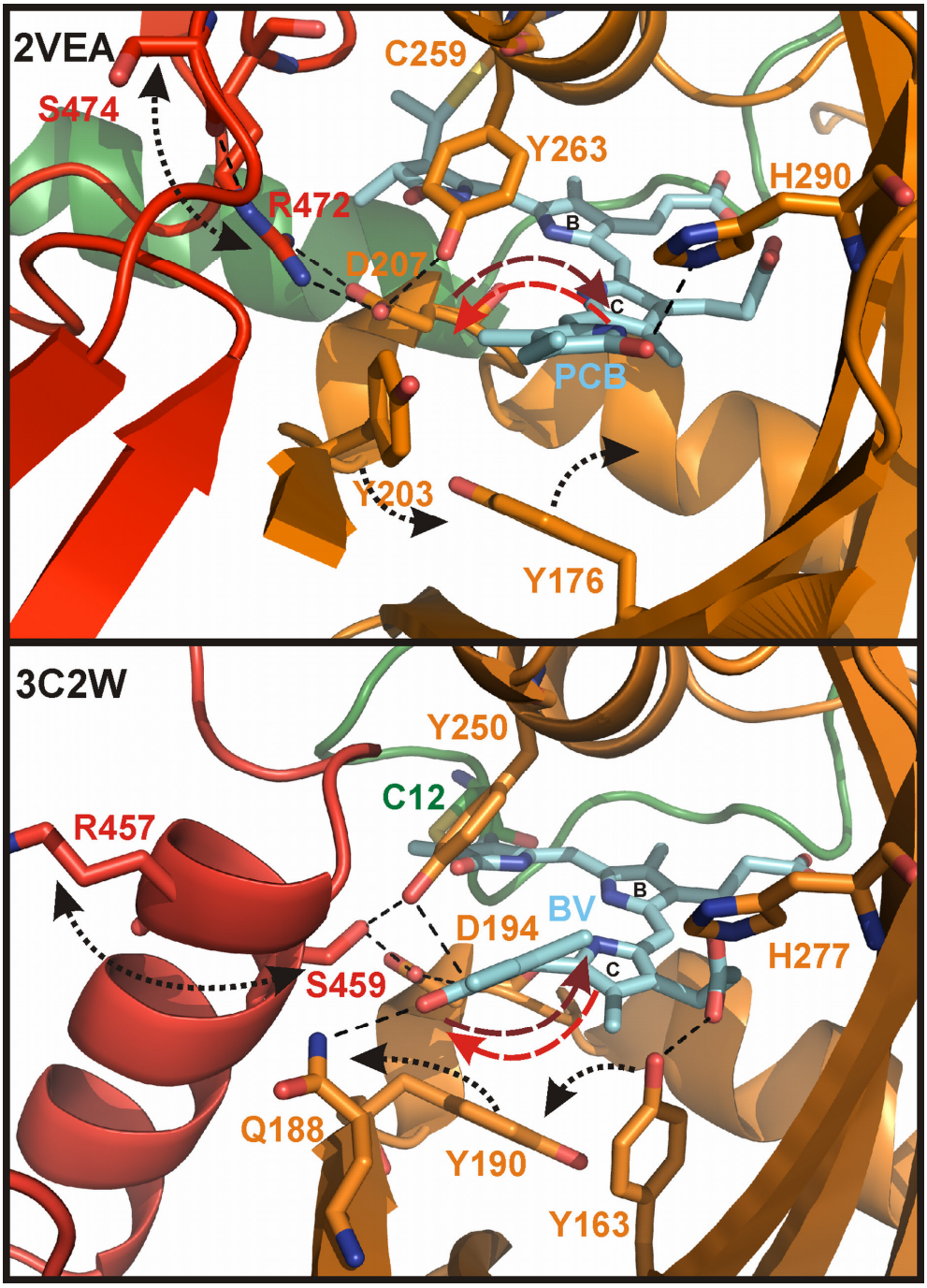

Figure 42: View on ring D in the chromophore pocket of 2VEA and 3C2W.
The dark red / red arrows (FR / R irradiation, respectively) indicate the proposed rotation of the D-ring upon photoconversion. The suggested movements of key residues during photoconversion are shown as black arrows. Dashed lines designate hydrogen bonds within 3.5 Å.

Secondly, the spectra of Y176H and Y203H show significant differences in Cph1 (Figure 46 in appendix 11.2.1) and DrBphP1 (39): Y176H is locked in the Pr state in the case of Cph1 (50, 78) whereas in DrBphP1 it can still undergo photoconversion. In Cph1, Y203H fails to display a typical phytochrome peak, instead shows a weak red absorbance and is unable to

photoconvert (Figure 46 in appendix 11.2.1). In DrBphP1, Y203H forms an intermediate upon R irradiation and exhibits a proper Pr-like peak upon FR irradiation (39).

Nevertheless, mutation of the conserved Tyr-203 to either a phenylalanine or tryptophan leads to normal photochromicity in Cph1 and DrBphP1, although the Y203W mutant displays a slightly weaker Pfr peak. Based on these observations it can be assumed that the D ring in cyanobacterial / plant phytochromes and in bacteriophytochromes might adopt a different tilt, which in turn might lead to a different photoconversion mechanism, as it has been suggested by Rockwell *et al.* (17, 26). Indeed, the Y263H mutation might position this residue closer to the D ring and hence enhance the stability of the Pr state by developing another hydrogen bond to the carbonyl group the chromophore, thus refraining from undergoing C15=C16 isomerisation. The minor change in the red absorbance peak, which shows almost instant reversion, might originate from a weak rotation of the D-ring towards Y176H. Thus the suggested counterclockwise rotation of the D ring in cyanobacterial and plant phytochromes upon photoconversion from Pr to Pfr is supported by mutational analysis presented here and in contrast to the clockwise rotation in bacteriophytochromes. The mutation of Tyr-203 to either a histidine or an asparagine could lead to its relocation to the space the D ring normally occupies in Pr as well as Pfr, thus leading to an abrupt abrogation of red absorbance due to a different conformation of the chromophore. The mutational analysis of Tyr-203 shows that a residue with a phenyl group is necessary for effective photoconversion, its bigger size maybe preventing it from occupying the space, the D-ring would adopt upon photoisomerisation. Nevertheless, the flip mechanism of Tyr-176 and Tyr-203 cannot be excluded for cyanobacterial and plant phytochromes although they might occupy a different position than is described in the Pfr ground state of PaBphP (72).

The stability of the Pfr state in PaBphP is ensured by hydrogen bonds from Gln-188 (Leu-201 in Cph1), Asp-194 (Asp-207) and Tyr-250 (Tyr-263), mutation of these residues reducing dark reversion significantly (72). Furthermore, Gln-188 is conserved among all bathy-phytochromes perhaps explaining the dark adapted Pfr state in these photosensors. The homologous L201Q mutation in Cph1Δ2 does not increase Pfr formation or lead to a dark-adaptation of the Pfr state. However, a slight increase of the Pfr fraction is observed when the

red-irradiated sample is left in darkness for several seconds. The increase of $\chi_{Pfr, max}$ in darkness might result from a rearrangement of the facial disposition of the D ring perhaps forming hydrogen bonds with the glutamine at position 201. This observation is further evidence for a different photoconversion mechanism between Cph1 / plant-like phytochromes and bacteriophytochromes with probably different residues involved in the stabilisation of the Pfr state than shown in the PaBphP structure.

The significance of Tyr-263 in the photoconversion mechanism was examined in more detail, since it was suggested to play a major role in the phototransformation and stability of the Pfr state (30, 39, 61, 72, 79). Although the subtle mutation Y263F resulted in a blue-shifted λ_{max}, neither the oscillator ratio nor the Pr extinction coefficient is significantly affected, implying that the conformation of the chromophore and its protonation are unchanged in relation to the wild type (79). Apart from Y263F, only few mutants studied in this work showed a similar spectroscopic behaviour (Table 6); most of which were not close to the chromophore. The hypsochromic shift of the red peak might be explained by the stronger tilt of the D ring relative to the C-D ring plain, as angles > 40° rapidly lead to an electronic decoupling from the delocalised π orbitals of the rest of the chromophore. Indeed, in 3ZQ5 ring D of the chromophore adopts a steeper inclination (Figure 37B) (79). However, the formation of a Pfr peak and the photoconversion quantum efficiency (Φ_P) from Pr → Pfr is considerably reduced, whereas that of the Pfr → Pr back reaction is unchanged. The lower Φ_P is mirrored as an increase in fluorescence quantum yield (Φ_F), indicating that the changes associated with the mutation affect the system prior to lumi-R formation. Indeed low-temperature fluorescence measurements show that the primary photoreaction from Pr to pre-lumi-R is not as efficient in the Tyr-263 mutants with a ~ four times lower rate constant (k_P) and a ~ 20 % reduction in the quantum yield (Φ_P (pre-Lumi-R)). Mutating Tyr-263 to either a histidine or a serine had a much bigger impact on the absorbance spectra and the Pfr formation (79). Y263H has a considerably reduced ε of ca. 47 mM^{-1} cm^{-1} for Pr at λ_{max} (as seen in the homologous mutant of DrBphP1 (39)). Although Pr bleaching and Pfr formation show only minor but symmetrical variations upon R irradiation, the quantum efficiency of the forward photoreaction is slightly higher than in Y263F (reflected in reduced fluorescence yield),

whereas that of the back reaction is unchanged. The fluorescence emission spectrum of this mutant is broadened, implying that the chromophore might be able to adopt various energetically-favourable conformations in the Pr state, many of which might be unable to photoconvert. Y263S, on the other hand, shows an asymmetrical difference spectrum, implying that the mutant is able to photoconvert, but unable to form Pfr, thus remaining in a meta-R state. The formation of Pfr necessitates a de- and reprotonation of the chromophore and in both Y263H and Y263S, reprotonation might be defective thus implying that an aromatic side chain is important for stabilising the Pfr state (79). Contrary studies of the non-canonical phytochrome SyB-Cph1 which assigned a key role to the hydroxyl group of Y263 (106), the results show that this hydroxyl group is not essential for Pfr formation in Cph1 (79). The Y263F mutant showed a much more subtle phenotype in which the quantum energy requirements for excitation to S1 were increased slightly (hypsochromic shifts of λ_{max} for Pr and Pfr) while the quantum efficiency of Pr → Pfr photoconversion was substantially reduced. This implies that the hydroxyl group promotes efficient C14=C15 isomerisation around ring D during photoconversion from Pr to Pfr (79).

Asp-207 from the DIP motif, conserved among all phytochromes known to date, plays a critical role in the formation of the Pfr state. Mutation of this residue leads to a bleaching of the Pr peak after R irradiation without formation of Pfr, forming an intermediate (Figure 46). This intermediate quickly reverts back to Pr in darkness, confirming earlier studies on Cph1Δ2 (57). These results were also observed for DrBphP1 (39) and PaBphP (72). Its position is below the chromophore within the pocket and the backbone carbonyl group stabilises a water molecule poised between the nitrogens of rings A, B and C and His-260 (Figure 26). This so-called pyrrole water has been present in all phytochrome structures to date (30-32, 61, 72), hence suggesting an important role in the chromophore stability. Indeed, Resonance Raman spectroscopy (RR) of D207A in DrBphP1 (39) and D197A in Agp1 (109) show that the chromophore is not fully protonated and that the mutant is thus unable to convert from the intermediate meta-R_c to the Pfr state and Asp-207 might be involved in the de- and reprotonation of the chromophore. His-260 has been hypothesized to be involved in the protonation of the chromophore in earlier studies (40, 110). Indeed, pH (57) as well as RR

(109) studies show that His-260 acts as a buffer in the protonation mechanism of the chromophore and the formation of Pfr. Mutation to a tyrosine leads to a complete loss of photochromicity and red absorbance in both Pr and Pfr probably due to the bulky size of the mutated residue (Figure 47 in appendix 11.2.1). H260Y seems to restrain the chromophore from positioning itself properly in the chromophore pocket, similarly to pea and oat phytochrome, where the analogous histidine was mutated to various residues including phenylalanine and resulted in the loss of photochromicity (111-113). NMR studies show that the chromophore is fully protonated in both Pr and Pfr states (55, 56, 60, 114). Furthermore, the chromophore gets deprotonated upon meta-R_c formation and reprotonated upon transformation into Pfr (40, 110). Isomerisation of the D ring might induce a structural rearrangement and breaking of the Asp-207–Arg-472 salt bridge thus triggering the deprotonation, the released proton being recovered by His-260 upon formation of the meta-R_c intermediate. The deprotonation of the chromophore and the subsequent formation of a hydrogen bond between the carboxyl group of Asp-207 and the ring D nitrogen then might lead to a reprotonation of the chromophore by His-260 and finally the transformation into Pfr. This model would explain why Asp-207 is important during the Pr → Pfr photoprocess, as the backbone carbonyl group is necessary for the stabilisation of the pyrrole water and the nitrogens of rings A, B and C and the carboxylate group is essential for Pfr stabilisation, as observed in PaBphP (72). The model would also explain why the imidazole moiety of His-260 is required for the uptake and release of a proton. Such an intricate protonation mechanism would require a defined microenvironment, in which protons are not freely available, but instead transferred from the chromophore to the surrounding residues and *vice versa*. Such a microenvironment is rendered possible through a closed chromophore cavity.

The structures of Cph1Δ2 and Y263F show that the chromophore pocket is completely sealed from outside solvent access by the formation of intimate contacts of the GAF domain with the tongue of the PHY domain and the N-terminal α1 helix (Figure 26A and Figure 43). As the spectra of crystallised PAS-GAF bidomains of DrBphP1 and RpBphP3 showed, phytochrome is unable to photoconvert properly and form stable Pfr without the presence of the PHY domain (30-32).

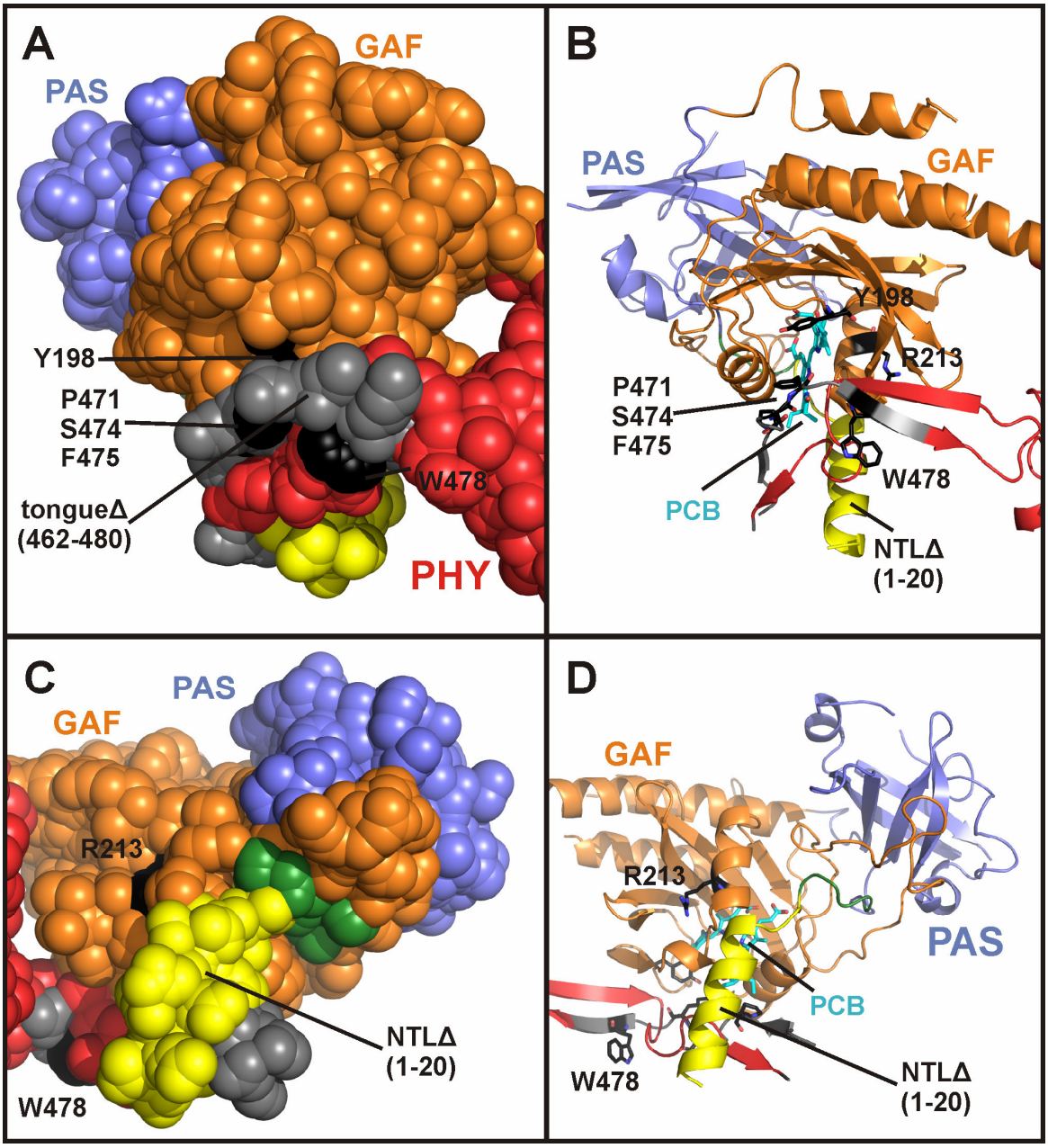

Figure 43: Solvent accessible surface of 2VEA shown as spheres or in cartoon representation.
The knotted PAS-GAF interface as sphere representation (A and C) and cartoon representation (B and D) shows conserved residues (black), which upon mutation were unable to form Pfr probably due to solvent access to the chromophore. The tongue deletion (grey) results in a dramatic shortening of the tongue, leaving the chromophore pocket open to solvent from outside. Interestingly, the N-terminal deletion (yellow) of the first 20 amino acids is still able to form Pfr.

Absence of the tongue to seal the chromophore pocket these bidomains cannot create the microenvironment around their respective chromophore needed for the protonation. This is also corroborated by some of the mutants, analysed in this work. By removing 18 residues from the tongue and thus shortening it enough to potentially allow access of solvent into the chromophore pocket the tongueΔ (462-480) mutant converts into the meta-R intermediate

upon R irradiation, unable to form Pfr. The same effect can be observed when mutating Pro-471, Ser-474 and Phe-475 of the PRxSF tongue motif covering the A- and D-ring of the chromophore to glycine or alanine, respectively. Mutation of Phe-475 to either histidine or tyrosine and thus retaining its aromatic character and size did not compromise the photoconversion from Pr to Pfr. Interestingly the N-terminal deletion construct NTLΔ (1-20), sealing the chromophore cavity around rings A and B, was still able to form normal Pfr. This observation suggests that photoconversion is mostly affected by solvent access into the microenvironment of ring D. Further mutations like R213S (below the chromophore), Y198S, Y263S and W478F (close to ring D) resulting in abnormal photoconversion support this hypothesis.

4.2. Signalling mechanism

The conformational change of the chromophore upon R irradiation from *ZZZssa* to *ZZEssa* leads to a structural change within the photosensory module of the phytochrome which then transmits the signal to the C-terminal transmitter module. The two structurally resolved sensory modules of Cph1 (2VEA and 3ZQ5) and mutational analysis of the photosensory module provide new information about the residues involved in this intramolecular signalling mechanism.

Apart from the thioether bond to Cys-259, the chromophore is also anchored in its pocket by forming a salt bridge with Arg-254 with its ring B propionate side chain and by hydrogen-bonding to Thr-274 and His-260 with its ring C propionate. Mutation of Arg-254 to either a lysine or an alanine merely affects the absorbance properties but does not compromise photoconversion of phytochrome. However, both mutants are unable to dimerise in the Pr state as observed in analytical SEC implying significant structural changes in the Pr state of the mutants. Preliminary data show that phosphotransfer is active independent of the light quality in R254A (60, 115). The analogous mutation in phyB (R352K) leads to an abrogation of PIF3 binding in the Pfr state (116, 117). Interestingly, recent NMR studies of Cph1 (60) show that the ring B propionate side chain swaps its salt bridge partner Arg-254 with Arg-222 due to a shift of the B and C rings upon photoisomerisation from Pr to Pfr, which might result

in a structural change leading to an interruption of the autophosphorylation and the phosphotransfer. Taken together, these observations suggest that the salt bridge itself is not responsible for the signalling, since the R254A mutant, disrupting the aforementioned salt bridge, is always active but instead that Arg-254 is directly involved in the signalling mechanism. Upon photoisomerisation, the guanidinium moiety of Arg-254 might be rearranged within the chromophore pocket and form hydrogen bonds and / or a salt bridge with a conserved residue in close vicinity, like Ser-251 or Thr-249, thus leading to a structural change and a termination of signalling (Figure 44).

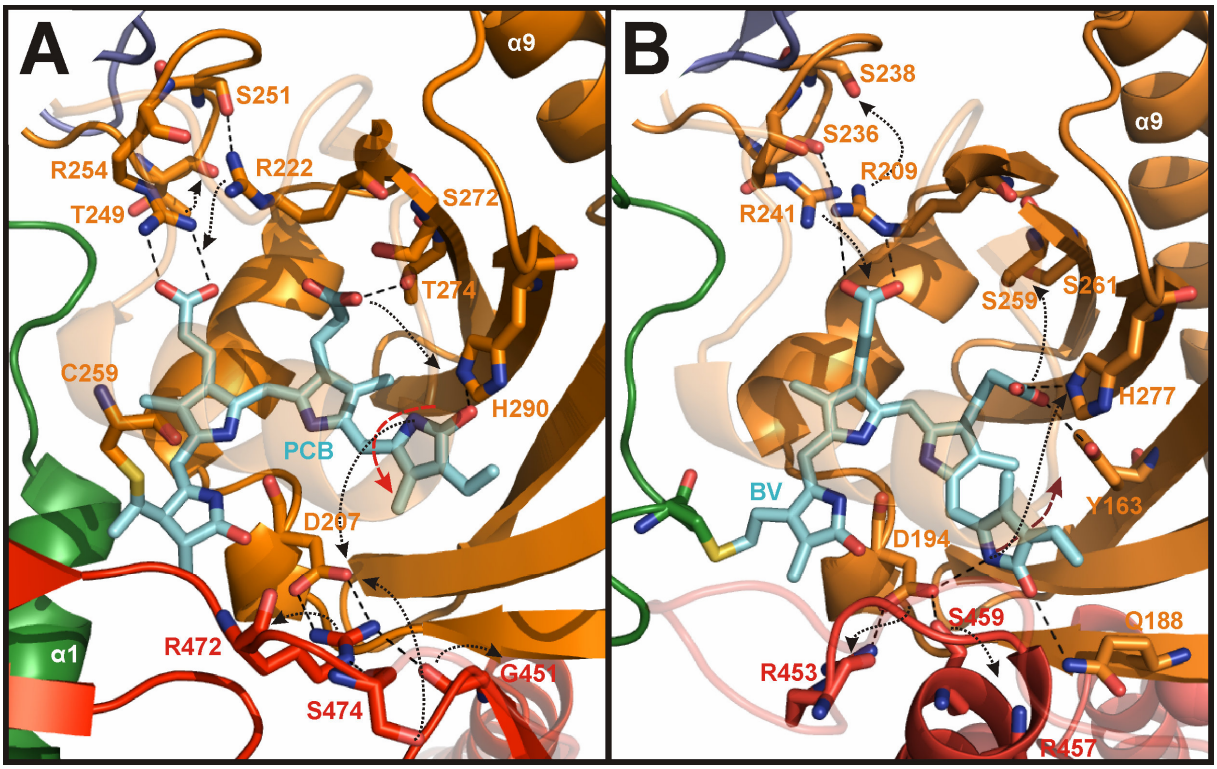

Figure 44: Proposed signalling mechanisms in bacterial phytochromes.
Proposed signalling mechanisms of Cph1 (A, 2VEA) upon R irradiation and PaBphP (B, 3C2W) upon FR irradation with black dashed lines indicating hydrogen bonds and salt bridges within 3.5 Å, black dashed arrows showing the movements of the interacting side chains and the red / dark red arrows showing the rotation of ring D upon photoisomerisation in the respective cases.

In the absence of the guanidinium moiety, these bonds cannot be formed which would explain why R254A is always active. In fact, S251A does not influence the photochromicity of Cph1 and shows state-dependent dimerisation, like R254A. In the bathyphytochrome structure 3C2W, Arg-241 (Arg-254 in Cph1) hydrogen bonds to Ser-236 (Thr-249) in the Pfr state while Arg-209 interacts with the C ring propionate side chain (72). The partner swapping and the formation of a salt bridge between the B ring propionate and Arg-222 is

essential for the stabilisation of the Pfr state, as mutations to either alanine or lysine lead to a severely impaired photochromicity. An analogous signalling system involving two conserved arginines and the propionate side chain of a heme has been proposed for the oxygen sensor FixL (100). Similarly to R254A, mutation of Thr-274 to an alanine results in a spectrally blue-shifted photoreceptor with normal photoconversion. Dimerisation of the Pr state in SEC is also affected. Furthermore, chemical shifts between Thr-274 and the propionate side chain of ring C are observed in NMR during photoconversion from Pr to Pfr implying a similar swapping mechanism as in the case of the propionate of ring B. In fact Ser-272 is close enough to and able to interact with the chromophore via a hydrogen bond to the ring C propionate in the Pfr state, as indicated by NMR data (60). S272A also shows state-dependent dimerisation in SEC. These observations suggest that Thr-274, like Arg-254, might be involved in the signalling pathway via a similar swapping mechanism (Figure 44). Nevertheless, phosphorylation assays are necessary to confirm the importance of Thr-274 in the signalling mechanism.

Earlier NMR studies suggest an implication of His-290 in the signalling route as photoconversion from Pr to Pfr mostly affects rings C and D (114, 118). His-290 seems to play a critical role in the stabilisation of the ring D tilt in the Pr state by formation of a hydrogen bond via its imidazole moiety with the carbonyl group of the ring. Mutating His-290 to an alanine leads to weak absorbance in the Pfr state upon R irradiation, similar to Y263S, which may be the result of a less inclined D ring tilt and would thus lead to a lower quantum yield of photoconversion also observed in the Y263S mutant (79). Upon photoconversion, His-290 forms a hydrogen bond with the ring C propionate side chain observed in the 3C2W structure of PaBphP (72) and might thereby be able to transmit a signal to the surface (Figure 44), as suggested by Rohmer *et al.* (114, 118). On the other hand, it is not known whether the Pfr ground state of bathyphytochromes is the active form. Since Arg-254 undergoes a structural rearrangement in 3C2W and Arg-222 connects to the C ring propionate via a salt bridge (which would be the case in the Pfr state of Cph1 too), it could be assumed that the Pr state is the signalling state, which would then imply that the minor structural rearrangement of His-290 might also lead to a change in signalling. In any case, due to the low Pfr absorbance it

might prove difficult to determine the phosphorylation activity of His-290 mutations and thus implicate this residue in the signalling mechanism.

Another possible signalling route resides on the other side of the chromophore between the nitrogens of rings A, B and C, namely Asp-207 which interacts with the guanidinium moiety of Arg-472 via a salt bridge. Upon photoconversion from Pr to Pfr, this salt bridge is severed and Asp-207 hydrogen bonds to Ser-474 and the nitrogen of the D ring. The now freed side chain of Arg-472 can thereby undergo a structural rearrangement similar to Arg-254 (Figure 44) and forwarding of the signal to the transmitter module stops. Indeed, the spectral characteristics and behaviour in SEC of the R472A mutant are almost identical to R254A. Furthermore, autophosphorylation and transfer of the phosphate to Rcp1 is light-independent in R472A (60, 115). Arg-472 also interacts with Gly-451 of the WGG motif via its guanidinium moiety. This motif plays an important role in orienting the tongue to the chromophore pocket and might thus also be essential for the signalling mechanism. Mutating any of the side chains of the WGG motif to an alanine does not impede photochromicity of the phytochromes; the extent of photoconversion is close to the one observed for wild type Cph1. However, state-dependent dimerisation in SEC is observed for W450A and G452A, implying that they indeed might be involved in the signalling pathway. G451A dimerises in both the Pr and Pfr states, although the situation might be different at lower concentrations than the one used. In any case, since Arg-472 is interacting with the main chain oxygen of Gly-451 (Figure 44), an effect on the dimerisation of the sensor module of Cph1 is not expected. Thus, Arg-472 might transmit the signal, resulting from the structural change of Asp-207 upon photoconversion, by breaking the hydrogen bond with Gly-451 through rearrangement of the tongue. Gly-451, now having more degrees of freedom to move, might then induce a structural rearrangement of the PHY domain and ultimately influence the transmitter module.

In the bathyphytochrome PaBphP structure 3C2W, this rearrangement is only partially observed due to the strong differences of the architecture of the tongue. Ser-459 (Ser-474 in Cph1) indeed interacts with Asp-194 (Asp-207) and Arg-457 (Arg-472) is pointing outwards. However, Asp-194 also interacts with Arg-453, which is not conserved among phytochromes

and would correspond to Lys-466 located close to the tip of the tongue in Cph1. Hence, bathyphytochromes might employ different amino acids in the tongue to transmit the signal, due to the structural differences of the tongue. Nevertheless, the overall mechanism of swapping salt bridge partners in the tongue upon photoconversion inducing a rearrangement of the PHY domain is still possible.

Having considered all the differences and structural changes upon photoconversion, the question emerges how these interactions on opposite sides of the chromophore work together to result in a collective signalling transfer from the sensor to the transmitter module. The 3D structure determination of the wild type Cph1Δ2 and Y263F as well as the characterisation of several mutants involved in the signalling mechanism suggest that the photoisomerisation of ring D induces structural changes in the chromophore pocket in a sort of "pulling mechanism", where the reorientation of the chromophore upon R irradiation followed by a swapping of the propionate side chain partners and the replacement of Arg-472 with Ser-474 of the PRxSF motif to interact with Asp-207 triggers a subtle but significant conformational change of the GAF domain and the tongue sealing the chromophore pocket, which then leads to a shift of the PHY domain and the adherent transmitter module. Whether this shift is a rotational movement of the α-helix connecting the PHY domain and the transmitter module as described by Möglich *et al.* (119) or a change in the plasticity of this α-helix, similar to the α9 helix connecting the GAF and PHY domains, needs to be investigated in the future.

4.3. Structural characteristics of phytochromes

One of the most intriguing features of phytochrome structures is the figure-of-eight knot made possible by a protruding loop from the GAF domain through which the N-terminal extension of the PAS domain passes through. Knotted structures are quite uncommon and only few protein families like phytochromes (30) and carbonic anhydrases (120, 121) possess a knot, which is commonly located near the N- or C-terminus. Neither the folding mechanism nor the function of a knot is clearly understood, although evidence suggests that successful knot formation necessitates duplication of secondary structures (122). The design of an artificially knotted structure by connecting two monomers to an intertwined dimer further

suggests that the occurrence of knots in a protein structure is due to gene duplication of entire domains (123). Incidentally, the GAF and PHY domains of phytochromes belong to the PAS superfamily; hence gene duplication might not only have led to the first canonical phytochromes but also to the knotted interface. With the exception of PAS-less phytochromes (106, 107), all current phytochrome structures possess a figure-of-eight knot, thus it seems likely that this feature is conserved among all canonical phytochromes. Although phyB from *A. thaliana* and fungal phytochromes have an extended N-terminus and knot formation might present a challenge (Figure 1), a deeply-buried knot has been found previously in a plant acetohydroxy acid isomeroreductase (124).

Knotted interfaces generally promote more stability and might even be involved in the function of the protein itself (120, 125). Analysis of N-terminally deleted residues and mutations of conserved amino acids near the knot in DrBphP1 showed that the photoreceptor is still able to covalently bind BV in most cases, but that photoreversibility was compromised (126). However, the observed phenotype might be due to the fact that bacteriophytochromes bind BV close to the N-terminus, thus mutating residues close to the knot might lead to an unfavourable configuration of the chromophore in the pocket leading to aberrant photochromicity. Truncation of the first 20 amino acids in the photosensory module of Cph1 did not have any effect on the photoconversion and merely resulted in a minor blue-shift of the Pr λ_{max} as was observed for several single mutations in the chromophore pocket. However, Pr dimerisation was compromised implying that surface changes are considerable and that these might also affect signalling as in the case of R254A and R472A (60). Mutations of the conserved Gln-27, located in the middle of the knot and H-bonding to residues from the protruding GAF domain loop, did not have any effect on the absorbance spectrum in either DrBphP1 (126) or Cph1. This is not surprising, since the chromophore pocket is not directly affected by the mutation. On the other hand, the Pr state of Q27E eluted as a monomer in SEC. Based on these results, the knot does neither improve nor reduce the photoconversion of phytochromes, but rather enhances overall protein stability and might also even be involved in the signalling mechanism. Phosphorylation assays might give a clear insight on its function in bacterial phytochromes. Nevertheless, PAS-less phytochromes probably do not comprise a

knotted interface (25, 106, 107), which suggests that the knot might indeed not play a significant role in the function of non-canonical phytochromes. As Cph2-like phytochromes also lack the transmitter module, their mode of action might be different altogether.

In plants, the surface close to the potential knot in phyB has been identified as a possible docking interface for PIF3 (117). PIFs enhance the degradation of nuclear-localised phyB in the Pfr state by promoting the polyubiquitination of phyB by COP1 (127, 128). Incidentally, knots have been hypothesized to protect proteins against degradation (125). Based on these observations, PIF3 might not only be bound by phyB, but could also interfere with the knot interface thus facilitating degradation. This mechanism involving a knotted interface would also protect phytochrome from unwanted degradation.

A second characteristic feature identified in the 2VEA structure is the phytochrome-specific PHY domain being a GAF domain, thus classifying the photoreceptor as tandem GAF proteins. Although the sequence identity on an amino acid level is less than 15 % (18, 19), the PHY domain might indeed have come into existence by gene duplication. This might also explain why Cph2-like phytochromes have two subsequent GAF domains, with the latter incapable of binding a chromophore (129, 130). A third GAF domain of the same protein is also able to bind a bilin, however (130). The instability of the Pfr state might result from the second GAF domain not being able to effectively seal the chromophore pocket similar to the PAS-GAF bidomains of DrBphP1 (30, 131). Furthermore, Cph2 does not possess a histidine kinase, thus this phytochrome family does also not require a functional PHY domain for signal transmission.

The main difference between the GAF and PHY domains, apart from PHY not being able to covalently attach a chromophore, is the position and length of the protruding loop, which is probably due to their different structural function. Whereas the loop of the GAF domain forms the basis for the knot and thus should protrude from the middle of the β-sheet sandwich, the tongue-composing loop of the PHY domain is located to the C-terminal end. This not only enables the tongue to cover the chromophore pocket but also enhances the lever action it exerts on the complete PHY domain upon photoisomerisation by being directly connected to the C-terminal α-helix upon which the transmitter module follows. Evolutionary

pressure might have led to the removal of the chromophore binding capability as well as the relocation of the protruding loop in the PHY domain.

4.4. Heterogeneity of the Pr state

The heterogeneity of the Pr ground state was first discovered and described in plants by fluorescence studies (37). The two distinct Pr states, Pr' and Pr", were discriminated by their possibility to be trapped in the lumi-R state at low temperatures. This phenomenon was explained by different activation energy barriers, which needed to be overcome in order to reach the excited state and could originate from a) two different pools of phytochromes (i.e. membrane-bound and soluble) and / or b) different conformations of the chromophore. In Cph1, the lumi-R state could not be trapped at low temperatures, thus it was categorized as Pr" (81, 132). However, further low-temperature fluorescence studies conducted on Cph1 showed major differences in the emission spectra and hinted at the existence of a ground state heterogeneity within the same phytochrome molecule (82). Furthermore, ultrafast time-resolved transient absorption spectroscopy studies implied the existence of different conformational Pr states (133).

Low-temperature fluorescence studies of Cph1Δ2 confirmed the heterogeneity of the Pr state and two distinct Pr species with λ_{max} = 664 nm and 652 nm at 77 K could be identified. By subtracting the bathochromic shift of ~ 5 nm due to the low temperature, the absorbance maxima at room temperature would amount to 659 nm and 647 nm, respectively. The former corresponds to the absorbance λ_{max} of recently purified Pr at room temperature. Incidentally, a two years old sample of Cph1Δ2, kept at 4 °C to avoid degradation, shows a considerably blue-shifted λ_{max} of 649 nm, which would account for the second Pr species. This would mean that two distinct populations of Cph1Δ2 are present at the beginning with a major species absorbing at 660 nm and the minor absorbing at 649 nm. The major species might require less energy to photoconvert, but is also less stable and over time this Pr pool "transforms" into the minor species (by attenuation due to photoconversion for example), the latter increasing and shifting λ_{max} to the blue. These two species could be explained by different conformations of the D-ring of the chromophore in the pocket, one conformation able to undergo full

photoconversion whereas the other reverts back to Pr upon irradiation. This might also explain the low quantum yield of phototransformation of the Pr state. Heterogeneity of the Pr state could also be confirmed by magic-angle spinning NMR (60, 114). The two Pr isoforms, denominated Pr-I and Pr-II, are distinguished by the charge distribution and hydrogen bonds affecting the chromophore and the two conserved histidines His-260 and His-290, respectively. Although the first Pr structure of the complete sensory module of wild type Cph1Δ2 did not reveal any heterogeneity of the chromophore, the recent crystal structure of the Y263F mutant showed different conformations at the attachment site of PCB and residues in the pocket with two possible rotamers. Furthermore, the D-ring adopted a steeper inclination in 3ZQ5, which might explain the low quantum yield of phototransformation of the Y263F mutation (79). Based on these observations the high variability of the D-ring inclination seen in various phytochrome structures might account for the heterogeneity of the Pr state as well as the low Φ_P with only few conformations able to undergo efficient photoconversion.

In addition to the heterogeneity of the Pr state of Cph1, discrepancies between *in vivo* and *in vitro* assembled phytochrome are shown in this work. These differences not only comprise the absorbance properties, but also the quaternary structure of the Pr states. Whereas the Pr state of *in vitro* assembled Cph1Δ2 shows a tendency to elute as a monomer in SEC, *in vivo* assembled holoprotein preferentially elutes as a dimer at equal concentrations. Differences in the dimerisation interface might originate from minor structural variations of the protein surface probably due to the fact that *in vivo* and *in vitro* assembly follows different mechanisms of chromophore attachment. Although phytochromes possess lyase activity and are thus able to autocatalytically attach the respective chromophore, other lyases might be involved in the assembly of holoprotein *in vivo (134, 135)*. Furthermore, the structure of the complete sensory module of Cph1 revealed a completely sealed chromophore pocket, thus raising the question how the chromophore enters this pocket without disturbing the overall structure (61). Whether the chromophore is attached to the apoprotein during translation of the latter or whether the tongue seals the pocket after incorporation of the chromophore cannot be concluded at this point. In addition, the differences between *in vitro* and *in vivo*

assembled phytochrome might constitute an intrinsic function of phytochromes indicating a deficiency of chromophore to increase its synthesis for example. However, phosphorylation assays showed no major differences between *in vitro* and *in vivo* assembled Cph1, although the apoprotein was also capable of autophosphorylation (46). Unfortunately, crystallisation of *in vitro* assembled Cph1Δ2, which would at least reveal structural differences, was not yet possible. The 3D structure of *in vitro* assembled Cph1Δ2 might constitute a first step in deciphering the heterogeneity observed not only in Cph1 but in phytochromes in general.

5. Summary

The 3D structure solution of the photosensory module from the cyanobacterial phytochrome Cph1 forms the basis to elucidate the photoconversion and the signalling mechanism of canonical phytochromes.

The first crystal structure of the sensor module, comprising the PAS, GAF and PHY domains, from Cph1 in its Pr state was solved at 2.45 Å resolution. 2VEA confirmed the figure-of-eight knot, produced by an N-terminal extension from the PAS domain passing through a protruding loop of the GAF domain. Furthermore, the structure shows that the GAF and PHY domains are related thus placing phytochromes among tandem GAF proteins. Unlike previous structures of incomplete bidomains from bacteriophytochromes, 2VEA displays a completely closed chromophore pocket, sealing of the chromophore cavity being accomplished by a tongue-like protrusion from the PHY domain. Hence, 2VEA provides structural evidence for the necessity of the PHY domain to have a photochemically competent phytochrome.

Several key residues were identified and selected for site-directed mutagenesis based on 2VEA that might be involved in either the photoconversion or the signalling mechanism. 48 different mutants were expressed, purified and characterised by UV-Vis spectroscopy. Selected mutants underwent further investigation (fluorescence spectroscopy, SEC, kinetic studies and crystallisation) to determine their function in phytochromes.

Three tyrosines close to the D-ring (Tyr-176, Tyr-203 and Tyr-263) of the chromophore were identified to play a significant role in the photoconversion mechanism. This work confirmed the importance of Tyr-176 which was analysed in detail in previous studies. Furthermore Tyr-203 mutations showed that this residue is also essential for effective photoconversion. Studies on Tyr-263 mutants suggest that its aromatic character is essential for photoconversion, but that the hydroxyl group only improves the quantum yield of phototransformation. The 3D structure of Y263F solved at 1.95 Å resolution gave new insights into the heterogeneity of phytochrome structures; apart from the PHY domain shift in relation to the PAS-GAF lobe enabled by a straightening of the connecting α9 helix, the attachment site of the chromophore

as well as several residues in the pocket displayed two possible conformations. Based on the results obtained by UV-Vis as well as fluorescence spectroscopy, the primary step in the photoconversion mechanism is most likely the isomerisation of the D-ring.

This work also identified key residues interacting with the propionate side chains of the chromophore in either the Pr or Pfr states which might transfer the signal from the chromophore to the transmitter module. Furthermore, conserved residues belonging to the PRxSF motif within the tongue of the PHY domain may be involved in the signalling mechanism. This work suggests that both the tongue and the propionate side chains act in conjunction to transmit the signal from the sensor to the transmitter module by shifting the PHY domain.

The crystal structure of the sensor module in its Pr state and the characterisation of conserved residues within the GAF and PHY domains constitute a crucial step in the elucidation of the photoconversion and signalling mechanism. Solving the structure of either the Pfr state of a canonical phytochrome or the full length photoreceptor comprising both the sensor and the transmitter modules might not only confirm but also improve the proposed models of photoconversion and phytochrome signalling in this work.

Zusammenfassung

Die Strukturlösung des Sensormoduls des cyanobakteriellen Phytochroms Cph1 bildet die Grundlage für die Aufklärung des Photokonversionsmechanismus und der Signaltransduktion in kanonischen Phytochromen.

Die erste Kristallstruktur des kompletten sensorischen Moduls von Cph1 im Pr Zustand, das aus den PAS, GAF und PHY Domänen besteht, konnte bis zu einer Auflösung von 2.45 Å gelöst werden. 2VEA bestätigte den Achtknoten, der zwischen der N-terminalen Verlängerung der PAS Domäne und einer herausragenden Schleife der GAF Domäne gebildet wird. Des Weiteren zeigt die Struktur, dass GAF und PHY Domänen strukturell verwandt sind und Phytochrome somit zu den Tandem GAF Proteinen gehören. Im Gegensatz zu den zuvor veröffentlichten unvollständigen Bidomänstrukturen von bakteriellen Phytochromen, zeigt 2VEA, dass die Chromophortasche mit Hilfe einer zungenartigen Ausstülpung der PHY Domäne versiegelt ist. Daher beweist 2VEA die Notwendigkeit der PHY Domäne für eine effektive Photokonversion von Phytochrom.

Entscheidende Aminosäuren, die möglicherweise an der Photokonversion oder der Signaltransduktion beteiligt sind, wurden mit Hilfe der 2VEA Struktur identifiziert und für die ortsspezifische Mutagenese ausgewählt. 48 verschiedene Mutanten wurden exprimiert, aufgereinigt und über UV-Vis Spektroskopie charakterisiert. Einige ausgewählte Mutationen wurden zudem intensiver analysiert (Fluoreszenzspektroskopie, SEC, kinetische Studien und Proteinkristallisation) um deren Funktion in Phytochrom zu ermitteln.

Drei Tyrosine (Tyr-176, Tyr-203 and Tyr-263), die sich in der Nähe des D-Rings des Chromophors befinden, spielen eine signifikante Rolle im Photokonversionsmechanismus. Diese Arbeit bestätigt die Bedeutung von Tyr-176, die schon in vorherigen Studien analysiert wurde. Des Weiteren zeigen Tyr-203 Mutationen, dass diese Aminosäure essentiell für die Photokonversion ist. Studien an Tyr-263 Mutanten weisen darauf hin, dass die aromatische Eigenschaft dieses Restes unabdinglich für die Photokonversion ist. Allerdings verbessert die Hydroxylgruppe lediglich die Quanteneffizienz der Phototransformation. Die Kristallstruktur von Y263F wurde bis zu einer Auflösung von 1.95 Å gelöst und gab neue Einblicke in die

strukturelle Heterogenität von Phytochromen. Neben der Verschiebung der PHY Domäne in Relation zum PAS-GAF Teil, die durch eine gerade Ausrichtung der verbindenden α9 Helix bewerkstelligt wird, gibt es bei der Bindung zwischen dem Chromophor und Cys-259 sowie bei weiteren Aminosäuren in der Tasche zwei mögliche Konformere. Basierend auf den UV-Vis- sowie Fluoreszenzdaten kann davon ausgegangen werden, dass die Isomerisierung des D-Rings den ersten Schritt der Photokonversion darstellt.

Diese Arbeit hat außerdem entscheidende Aminosäuren identifiziert, die mit den Propionatseitenketten des Chromophors in beiden Zuständen interagieren und so das Signal vom Chromophor auf das Transmittermodul übertragen. Des Weiteren gibt es konservierte Aminosäurereste die dem PRxSF Motiv der Zunge aus der PHY Domäne zugeordnet werden und an der Signaltransduktion beteiligt sind. Die Ergebnisse dieser Arbeit legen nahe, dass die Zunge und die Propionatseitenketten gemeinsam dazu beitragen, das Signal durch eine strukturelle Umpositionierung der PHY Domäne vom Sensor zum Transmitter weiter zu leiten.

Die Kristallstruktur des Sensormoduls im Pr Zustand und die Charakterisierung von konservierten Aminosäuren, die sich in der GAF bzw. PHY Domäne befinden, bilden einen entscheidenden Schritt um den Mechanismus der Photokonversion sowie der Signaltransduktion zu entziffern. Die Strukturlösung des Pfr Zustands eines kanonischen Phytochroms und des kompletten Photorezeptors könnten dazu beitragen, das in dieser Arbeit vorgestellte Modell der Photokonversion und der Signaltransduktion zu bestätigen und zu verbessern.

6. Reference list

1. Tong, H., Leasure, C. D., Hou, X., Yuen, G., Briggs, W., & He, Z. H. (2008) Role of root UV-B sensing in Arabidopsis early seedling development *Proc. Natl. Acad. Sci. U. S. A* 105: 21039-21044.

2. Gardner, G., Lin, C., Tobin, E. M., Loehrer, H., & Brinkman, D. (2009) Photobiological properties of the inhibition of etiolated Arabidopsis seedling growth by ultraviolet-B irradiation *Plant Cell Environ.* 32: 1573-1583.

3. Rizzini, L., Favory, J. J., Cloix, C., Faggionato, D., O'Hara, A., Kaiserli, E., Baumeister, R., Schafer, E., Nagy, F., Jenkins, G. I. *et al.* (2011) Perception of UV-B by the Arabidopsis UVR8 protein *Science* 332: 103-106.

4. Briggs, W. R. & Christie, J. M. (2002) Phototropins 1 and 2: versatile plant blue-light receptors *Trends Plant Sci* 7: 204-210.

5. Li, Q. H. & Yang, H. Q. (2007) Cryptochrome signaling in plants *Photochem. Photobiol.* 83: 94-101.

6. Banerjee, R. & Batschauer, A. (2005) Plant blue-light receptors *Planta* 220: 498-502.

7. Kim, W. Y., Fujiwara, S., Suh, S. S., Kim, J., Kim, Y., Han, L., David, K., Putterill, J., Nam, H. G., & Somers, D. E. (2007) ZEITLUPE is a circadian photoreceptor stabilized by GIGANTEA in blue light *Nature* 449: 356-360.

8. Butler, W. L., Norris, K. H., Siegelman, H. W., & Hendricks, S. B. (1959) Detection, assay, and preliminary purification of the pigment controlling photoresponsive development of plants *Proc. Natl. Acad. Sci. USA* 45: 1703-1708.

9. Franklin, K. A. & Quail, P. H. (2010) Phytochrome functions in Arabidopsis development *J. Exp. Bot.* 61: 11-24.

10. Hughes, J., Lamparter, T., Mittmann, F., Hartmann, E., Gärtner, W., Wilde, A., & Börner, T. (1997) A prokaryotic phytochrome *Nature* 386: 663.

11. Yeh, K. C., Wu, S. H., Murphy, J. T., & Lagarias, J. C. (1997) A cyanobacterial phytochrome two-component light sensory system *Science* 277: 1505-1508.

12. Wilde, A., Fiedler, B., & Börner, T. (2002) The cyanobacterial phytochrome Cph2 inhibits phototaxis towards blue light *Mol. Microbiol.* 44: 981-988.

13. Davis, S. J., Vener, A. V., & Vierstra, R. D. (1999) Bacteriophytochromes: Phytochrome-Like Photoreceptors from Nonphotosynthetic Eubacteria *Science* 286: 2517-2520.

14. Griffith, G. W., Jenkins, G. I., Milner-White, E. J., & Clutterbuck, A. J. (1994) Homology at the amino acid level between plant phytochromes and a regulator of sexual sporulation in Emericella (=Aspergillus) nidulans *Photochem. Photobiol.* 59: 252-256.

15. Blumenstein, A., Vienken, K., Tasler, R., Purschwitz, J., Veith, D., Frankenberg-Dinkel, N., & Fischer, R. (2005) The *Aspergillus nidulans* phytochrome FphA represses sexual development in red light *Curr. Biol.* 15: 1833-1838.

16. De, R., V, Raniello, R., Maumus, F., Rogato, A., Bowler, C., & Falciatore, A. (2009) Gene silencing in the marine diatom Phaeodactylum tricornutum *Nucleic Acids Res.* 37: e96.

17. Rockwell, N. C. & Lagarias, J. C. (2010) A brief history of phytochromes *Chemphyschem.* 11: 1172-1180.

18. Montgomery, B. L. & Lagarias, J. C. (2002) Phytochrome ancestry: sensors of bilins and light *Trends Plant Sci.* 7: 357-366.

19. Rockwell, N. C., Su, Y. S., & Lagarias, J. C. (2006) Phytochrome structure and signaling mechanisms *Annu. Rev. Plant Biol.* 57: 837-858.

20. Yeh, K. C. & Lagarias, J. C. (1998) Eukaryotic phytochromes: light-regulated serine/threonine protein kinases with histidine kinase ancestry *Proc. Natl. Acad. Sci. USA* 95: 13976-13981.

21. Han, Y. J., Kim, H. S., Song, P. S., & Kim, J. I. (2010) Autophosphorylation desensitizes phytochrome signal transduction *Plant Signal. Behav.* 5.

22. Han, Y. J., Kim, H. S., Kim, Y. M., Shin, A. Y., Lee, S. S., Bhoo, S. H., Song, P. S., & Kim, J. I. (2010) Functional characterization of phytochrome autophosphorylation in plant light signaling *Plant Cell Physiol* 51: 596-609.

23. Schmidt, A. J., Ryjenkov, D. A., & Gomelsky, M. (2005) The ubiquitous protein domain EAL is a cyclic diguanylate-specific phosphodiesterase: enzymatically active and inactive EAL domains *J. Bacteriol.* 187: 4774-4781.

24. Schirmer, T. & Jenal, U. (2009) Structural and mechanistic determinants of c-di-GMP signalling *Nat. Rev. Microbiol.* 7: 724-735.

25. Fiedler, B., Börner, T., & Wilde, A. (2005) Phototaxis in the cyanobacterium *Synechocystis* sp. PCC 6803: role of different photoreceptors *Photochem Photobiol* 81: 1481-1488.

26. Rockwell, N. C., Shang, L., Martin, S. S., & Lagarias, J. C. (2009) Distinct classes of red/far-red photochemistry within the phytochrome superfamily *Proc. Natl. Acad. Sci. USA* 106: 6123-6127.

27. Hirose, Y., Shimada, T., Narikawa, R., Katayama, M., & Ikeuchi, M. (2008) Cyanobacteriochrome CcaS is the green light receptor that induces the expression of phycobilisome linker protein *Proc. Natl. Acad. Sci. U. S. A* 105: 9528-9533.

28. Narikawa, R., Fukushima, Y., Ishizuka, T., Itoh, S., & Ikeuchi, M. (2008) A novel photoactive GAF domain of cyanobacteriochrome AnPixJ that shows reversible green/red photoconversion *J. Mol. Biol.* 380: 844-855.

29. Rockwell, N. C., Njuguna, S. L., Roberts, L., Castillo, E., Parson, V. L., Dwojak, S., Lagarias, J. C., & Spiller, S. C. (2008) A second conserved GAF domain cysteine is required for the blue/green photoreversibility of cyanobacteriochrome Tlr0924 from Thermosynechococcus elongatus *Biochemistry* 47: 7304-7316.

30. Wagner, J. R., Brunzelle, J. S., Forest, K. T., & Vierstra, R. D. (2005) A light-sensing knot revealed by the structure of the chromophore-binding domain of phytochrome *Nature* 438: 325-331.

31. Wagner, J. R., Zhang, J., Brunzelle, J. S., Vierstra, R. D., & Forest, K. T. (2007) High resolution structure of deinococcus bacteriophytochrome yields new insights into phytochrome architecture and evolution *J Biol. Chem.* 282: 12298-12309.

32. Yang, X., Stojkovic, E. A., Kuk, J., & Moffat, K. (2007) Crystal structure of the chromophore binding domain of an unusual bacteriophytochrome, RpBphP3, reveals residues that modulate photoconversion *Proc. Natl. Acad. Sci. USA* 104: 12571-12576.

33. Kneip, C., Hildebrandt, P., Schlamann, W., Braslavsky, S. E., Mark, F., & Schaffner, K. (1999) Protonation state and structural changes of the tetrapyrrole chromophore during the Pr --> Pfr phototransformation of phytochrome: a resonance Raman spectroscopic study *Biochemistry* 38: 15185-15192.

34. Inomata, K., Hammam, M. A., Kinoshita, H., Murata, Y., Khawn, H., Noack, S., Michael, N., & Lamparter, T. (2005) Sterically locked synthetic bilin derivatives and phytochrome Agp1 from Agrobacterium tumefaciens form photoinsensitive Pr- and Pfr-like adducts *J Biol. Chem.* 280: 24491-24497.

35. Fodor, S. P., Lagarias, J. C., & Mathies, R. A. (1990) Resonance Raman analysis of the Pr and Pfr forms of phytochrome *Biochemistry* 29: 11141-11146.

36. Rüdiger, W., Thümmler, F., Cmiel, E., & Schneider, S. (1983) Chromophore structure of the physiologically active form Pfr of phytochrome *Proc. Natl. Acad. Sci. USA* 80: 6244-6248.

37. Sineshchekov, V. A. (1995) Photobiophysics and photobiochemistry of the heterogeneous phytochrome system *Biochimica. et Biophysica. Acta (BBA.) - Bioenergetics.* 1228: 125-164.

38. Savikhin, S., Wells, T., Song, P. S., & Struve, W. S. (1993) Ultrafast pump-probe spectroscopy of native etiolated oat phytochrome *Biochemistry* 32: 7512-7518.

39. Wagner, J. R., Zhang, J., von Stetten, D., Gunther, M., Murgida, D. H., Mroginski, M. A., Walker, J. M., Forest, K. T., Hildebrandt, P., & Vierstra, R. D. (2008) Mutational analysis of *Deinococcus radiodurans* bacteriophytochrome reveals key amino acids necessary for the photochromicity and proton exchange cycle of phytochromes *J. Biol. Chem.* 283: 12212-12226.

40. van Thor, J. J., Borucki, B., Crielaard, W., Otto, H., Lamparter, T., Hughes, J., Hellingwerf, K. J., & Heyn, M. P. (2001) Light-induced proton release and proton uptake reactions in the cyanobacterial phytochrome Cph1 *Biochemistry* 40: 11460-11471.

41. Braslavsky, S. E., Gartner, W., & Schaffner, K. (1997) Phytochrome photoconversion *Plant, Cell Environ.* 20: 700-706.

42. Chen, E., Lapko, V. N., Lewis, J. W., Song, P. S., & Kliger, D. S. (1996) Mechanism of native oat phytochrome photoreversion: a time- resolved absorption investigation *Biochemistry* 35: 843-850.

43. Butler, W. L., Lane, H. C., & Siegelman, H. W. (1963) Nonphotochemical Transformations of Phytochrome in Vivo *Plant Physiol* 38: 514-519.

44. Butler, W. L. & Lane, H. C. (1965) Dark Transformations of Phytochrome in vivo. II *Plant Physiol* 40: 13-17.

45. Sineshchekov, V. A. & Sineshchekov, A. V. (1990) Different photoactive states of the red phytochrome form in the cells of etiolated pea and oat seedlings *Journal of Photochemistry. and Photobiology. B: Biology.* 5: 197-217.

46. Psakis, G., Mailliet, J., Lang, C., Teufel, L., Essen, L. O., & Hughes, J. (2011) Signalling kinetics of cyanobacterial phytochrome Cph1, a light regulated histidine kinase *Biochemistry* 50: 6178-6188.

47. Butler, W. L., Hendricks, S. B., & Siegelman, H. W. (1964) Action spectra of phytochrome in vitro *Photochem. Photobiol.* 3: 521-528.

48. Gambetta, G. A. & Lagarias, J. C. (2001) Genetic engineering of phytochrome biosynthesis in bacteria *Proc. Natl. Acad. Sci. USA* 98: 10566-10571.

49. Landgraf, F. T., Forreiter, C., Hurtado, P. A., Lamparter, T., & Hughes, J. (2001) Recombinant holophytochrome in *Escherichia coli FEBS Lett.* 508: 459-462.

50. Fischer, A. J. & Lagarias, J. C. (2004) Harnessing phytochrome's glowing potential *Proc. Natl. Acad. Sci. USA* 101: 17334-17339.

51. Shu, X., Royant, A., Lin, M. Z., Aguilera, T. A., Lev-Ram, V., Steinbach, P. A., & Tsien, R. Y. (2009) Mammalian Expression of Infrared Fluorescent Proteins Engineered from a Bacterial Phytochrome *Science* 324: 804-807.

52. Fischer, A. J., Rockwell, N. C., Jang, A. Y., Ernst, L. A., Waggoner, A. S., Duan, Y., Lei, H., & Lagarias, J. C. (2005) Multiple roles of a conserved GAF domain tyrosine residue in cyanobacterial and plant phytochromes *Biochemistry* 44: 15203-15215.

53. Su, Y. S. & Lagarias, J. C. (2007) Light-Independent phytochrome signaling mediated by dominant GAF domain tyrosine mutants of Arabidopsis phytochromes in transgenic plants *Plant Cell* 19: 2124-2139.

54. Hunt, R. E. & Pratt, L. H. (1981) Physicochemical differences between the red- and the far-red- absorbing forms of phytochrome *Biochemistry* 20: 941-945.

55. Rohmer, T., Strauss, H., Hughes, J., de Groot, H., Gartner, W., Schmieder, P., & Matysik, J. (2006) 15N MAS NMR studies of cph1 phytochrome: Chromophore dynamics and intramolecular signal transduction *J Phys. Chem. B* 110: 20580-20585.

56. Strauss, H. M., Hughes, J., & Schmieder, P. (2005) Heteronuclear solution-state NMR studies of the chromophore in cyanobacterial phytochrome cph1 *Biochemistry* 44: 8244-8250.

57. Hahn, J., Strauss, H. M., Landgraf, F. T., Gimenez, H. F., Lochnit, G., Schmieder, P., & Hughes, J. (2006) Probing protein-chromophore interactions in Cph1 phytochrome by mutagenesis *FEBS J* 273: 1415-1429.

58. Bussow, K., Cahill, D., Nietfeld, W., Bancroft, D., Scherzinger, E., Lehrach, H., & Walter, G. (1998) A method for global protein expression and antibody screening on high-density filters of an arrayed cDNA library *Nucleic Acids Res.* 26: 5007-5008.

59. Hemsley, A., Arnheim, N., Toney, M. D., Cortopassi, G., & Galas, D. J. (1989) A simple method for site-directed mutagenesis using the polymerase chain reaction *Nucleic Acids Res.* 17: 6545-6551.

60. Song, C., Psakis, G., Lang, C., Mailliet, J., Gartner, W., Hughes, J., & Matysik, J. (2011) Two ground state isoforms and a chromophore D-ring photoflip triggering extensive intramolecular changes in a canonical phytochrome *Proc. Natl. Acad. Sci. U. S. A* 108: 3842-3847.

61. Essen, L.-O., Mailliet, J., & Hughes, J. (2008) The structure of a complete phytochrome sensory module in the Pr ground state *Proc. Natl. Acad. Sci. USA* 105: 14709-14714.

62. Mailliet, J., Psakis, G., Schroeder, C., Kaltofen, S., Durrwang, U., Hughes, J., & Essen, L. O. (2009) Dwelling in the dark: procedures for the crystallography of phytochromes and other photochromic proteins *Acta Crystallographica Section D* 65: 1232-1235.

63. Berkelman, T. R. & Lagarias, J. C. (1986) Visualization of bilin-linked peptides and proteins in polyacrylamide gels *Anal. Biochem* 156: 194-201.

64. Pratt, L. H. (1975) Photochemistry of high molecular weight phytochrome in vitro *Photochem. Photobiol.* 22: 33-36.

65. Glazer, A. N. & Fang, S. (1973) Chromophore content of blue-green algal phycobiliproteins *J. Biol. Chem.* 248: 659-662.

66. Latimer, P., Banister, T. T., & Rabinowitch, E. (1956) Quantum Yields of Fluorescence of Plant Pigments *Science* 124: 585-586.

67. Nicholas J.Turro (1991) in *Modern molecular photochemistry* (University Science Books, pp. 85-87.

68. Rubinson, K. A., Ladner, J. E., Tordova, M., & Gilliland, G. L. (2000) Cryosalts: suppression of ice formation in macromolecular crystallography *Acta Crystallographica Section D* 56: 996-1001.

69. Yeh, J. I. & Hol, W. G. J. (1998) A flash-annealing technique to improve diffraction limits and lower mosaicity in crystals of glycerol kinase *Acta Crystallographica Section D* 54: 479-480.

70. Bourgeois, D., Vernede, X., Adam, V., Fioravanti, E., & Ursby, T. (2002) A microspectrophotometer for UV-visible absorption and fluorescence studies of protein crystals *J. Appl. Cryst.* 35: 319-326.

71. Lamparter, T., Mittmann, F., Gärtner, W., Börner, T., Hartmann, E., & Hughes, J. (1997) Characterization of recombinant phytochrome from the cyanobacterium *Synechocystis Proc. Natl. Acad. Sci. USA* 94: 11792-11797.

72. Yang, X., Kuk, J., & Moffat, K. (2008) Crystal structure of Pseudomonas aeruginosa bacteriophytochrome: photoconversion and signal transduction *Proc. Natl. Acad. Sci. USA* 105: 14715-14720.

73. Giraud, E., Zappa, S., Vuillet, L., Adriano, J. M., Hannibal, L., Fardoux, J., Berthomieu, C., Bouyer, P., Pignol, D., & Vermeglio, A. (2005) A new type of bacteriophytochrome acts in tandem with a classical bacteriophytochrome to control the antennae synthesis in Rhodopseudomonas palustris *J Biol. Chem.* 280: 32389-32397.

74. Tasler, R., Moises, T., & Frankenberg-Dinkel, N. (2005) Biochemical and spectroscopic characterization of the bacterial phytochrome of Pseudomonas aeruginosa *FEBS J.* 272: 1927-1936.

75. Karniol, B. & Vierstra, R. D. (2003) The pair of bacteriophytochromes from Agrobacterium tumefaciens are histidine kinases with opposing photobiological properties *Proc. Natl. Acad. Sci. USA* 100: 2807-2812.

76. Lamparter, T., Michael, N., Mittmann, F., & Esteban, B. (2002) Phytochrome from *Agrobacterium tumefaciens* has unusual spectral properties and reveals an N-terminal chromophore attachment site *Proc. Natl. Acad. Sci. USA* 99: 11628-11633.

77. Giraud, E., Fardoux, J., Fourrier, N., Hannibal, L., Genty, B., Bouyer, P., Dreyfus, B., & Vermeglio, A. (2002) Bacteriophytochrome controls photosystem synthesis in anoxygenic bacteria *Nature* 417: 202-205.

78. Fischer, A. J., Rockwell, N. C., Jang, A. Y., Ernst, L. A., Waggoner, A. S., Duan, Y., Lei, H., & Lagarias, J. C. (2005) Multiple roles of a conserved GAF domain tyrosine residue in cyanobacterial and plant phytochromes *Biochemistry* 44: 15203-15215.

79. Mailliet, J., Psakis, G., Sineshchekov, V., Essen, L.-O., & Hughes, J. (2011) Spectroscopy and a high-resolution crystal structure of Tyr-263 mutants of cyanobacterial phytochrome Cph1 *J. Mol. Biol.* accepted.

80. Lamparter, T., Esteban, B., & Hughes, J. (2001) Phytochrome Cph1 from the cyanobacterium Synechocystis PCC6803. Purification, assembly, and quaternary structure *Eur. J. Biochem.* 268: 4720-4730.

81. Sineshchekov, V., Hughes, J., & Lamparter, T. (1998) Fluorescence and photochemistry of recombinant phytochrome from the cyanobacterium *Synechocystis*. *Photochem. Photobiol.* 67: 263-267.

82. Sineshchekov, V., Koppel, L., Esteban, B., Hughes, J., & Lamparter, T. (2002) Fluorescence investigation of the recombinant cyanobacterial phytochrome (Cph1) and its C-terminally truncated monomeric species (Cph1Delta2): implication for holoprotein assembly, chromophore-apoprotein interaction and photochemistry *J. Photochem. Photobiol. B* 67: 39-50.

83. Strauss, H. M., Schmieder, P., & Hughes, J. (2005) Light-dependent dimerisation in the N-terminal sensory module of cyanobacterial phytochrome 1 *FEBS Lett.* 18: 3970-3974.

84. Feilke, Kathleen (2010) Untersuchungen zur Quartärstruktur des cyanobakteriellen Phytochroms Cph1.

85. Panjikar, S., Parthasarathy, V., Lamzin, V. S., Weiss, M. S., & Tucker, P. A. (2005) Auto-Rickshaw: an automated crystal structure determination platform as an efficient tool for the validation of an X-ray diffraction experiment *Acta Crystallogr. D Biol. Crystallogr.* 61: 449-457.

86. Bricogne, G., Vonrhein, C., Flensburg, C., Schiltz, M., & Paciorek, W. (2003) Generation, representation and flow of phase information in structure determination: recent developments in and around SHARP 2.0 *Acta Crystallogr. D Biol. Crystallogr.* 59: 2023-2030.

87. (1994) The CCP4 suite: programs for protein crystallography *Acta Crystallogr. D Biol. Crystallogr.* 50: 760-763.

88. Emsley, P. & Cowtan, K. (2004) Coot: model-building tools for molecular graphics *Acta Crystallographica Section D* 60: 2126-2132.

89. Lagarias, J. C. & Rapoport, H. (1980) Chromopeptides from phytochrome. The structure and linkage of the Pr form of the phytochrome chromophore *J Am. Chem. Soc.* 102: 4821-4828.

90. Yang, X., Kuk, J., & Moffat, K. (2009) Conformational differences between the Pfr and Pr states in Pseudomonas aeruginosa bacteriophytochrome *Proc. Natl. Acad. Sci. USA* 106: 15639-15644.

91. Scheerer, P., Michael, N., Park, J. H., Nagano, S., Choe, H. W., Inomata, K., Borucki, B., Krauss, N., & Lamparter, T. (2010) Light-induced conformational changes of the chromophore and the protein in phytochromes: bacterial phytochromes as model systems *Chemphyschem.* 11: 1090-1105.

92. Bender, A. T. & Beavo, J. A. (2006) Cyclic nucleotide phosphodiesterases: molecular regulation to clinical use *Pharmacol. Rev.* 58: 488-520.

93. Martinez, S. E., Wu, A. Y., Glavas, N. A., Tang, X. B., Turley, S., Hol, W. G., & Beavo, J. A. (2002) The two GAF domains in phosphodiesterase 2A have distinct roles in dimerization and in cGMP binding *Proc. Natl. Acad. Sci. USA* 99: 13260-13265.

94. Bruder, S., Linder, J. U., Martinez, S. E., Zheng, N., Beavo, J. A., & Schultz, J. E. (2005) The cyanobacterial tandem GAF domains from the cyaB2 adenylyl cyclase signal via both cAMP-binding sites *Proc. Natl. Acad. Sci. U. S. A* 102: 3088-3092.

95. Martinez, S. E., Bruder, S., Schultz, A., Zheng, N., Schultz, J. E., Beavo, J. A., & Linder, J. U. (2005) Crystal structure of the tandem GAF domains from a cyanobacterial adenylyl cyclase: modes of ligand binding and dimerization *Proc. Natl. Acad. Sci. U. S. A* 102: 3082-3087.

96. Neuhaus, G., Bowler, C., Hiratsuka, K., Yamagata, H., & Chua, N.-H. (1997) Phytochrome-regulated repression of gene expression requires calcium and cGMP *EMBO J.* 16: 2554-2564.

97. Bowler, C., Neuhaus, G., Yamagata, H., & Chua, N.-H. (1994) Cyclic GMP and calcium mediate phytochrome phototransduction *Cell* 77: 73-81.

98. Lamparter, T., Carrascal, M., Michael, N., Martinez, E., Rottwinkel, G., & Abian, J. (2004) The biliverdin chromophore binds covalently to a conserved cysteine residue in the N-terminus of Agrobacterium phytochrome Agp1 *Biochemistry* 43: 3659-3669.

99. Mroginski, M. A., Murgida, D. H., & Hildebrandt, P. (2006) Calculation of vibrational spectra of linear tetrapyrroles. 4. Methine bridge C-H out-of-plane modes *J Phys. Chem. A Mol. Spectrosc. Kinet. Environ. Gen. Theory.* 110: 10564-10574.

100. Gong, W., Hao, B., & Chan, M. K. (2000) New mechanistic insights from structural studies of the oxygen-sensing domain of *Bradyrhizobium japonicum* FixL *Biochemistry* 39: 3955-3962.

101. Vagin, A. & Teplyakov, A. (1997) MOLREP: an Automated Program for Molecular Replacement *J. Appl. Cryst.* 30: 1022-1025.

102. Schomaker, T. *CCP4 Program Suite : refmac*.

103. Mroginski, M. A., Murgida, D. H., von, S. D., Kneip, C., Mark, F., & Hildebrandt, P. (2004) Determination of the chromophore structures in the photoinduced reaction cycle of phytochrome *J. Am. Chem. Soc.* 126: 16734-16735.

104. Mroginski, M. A., Murgida, D. H., & Hildebrandt, P. (2007) The chromophore structural changes during the photocycle of phytochrome: a combined resonance Raman and quantum chemical approach *Acc. Chem. Res.* 40: 258-266.

105. Mroginski, M. A., von Stetten, D., Escobar, F. V., Strauss, H. M., Kaminski, S., Scheerer, P., Gunther, M., Murgida, D. H., Schmieder, P., Bongards, C. *et al.* (2009) Chromophore structure of cyanobacterial phytochrome Cph1 in the Pr state: Reconciling structural and spectroscopic data by QM/MM calculations *Biophys. J.* 96: 4153-4163.

106. Ulijasz, A. T., Cornilescu, G., Cornilescu, C. C., Zhang, J., Rivera, M., Markley, J. L., & Vierstra, R. D. (2010) Structural basis for the photoconversion of a phytochrome to the activated Pfr form *Nature* 463: 250-254.

107. Cornilescu, G., Ulijasz, A. T., Cornilescu, C. C., Markley, J. L., & Vierstra, R. D. (2008) Solution structure of a cyanobacterial phytochrome GAF domain in the red-light-absorbing ground state *J. Mol. Biol.* 383: 403-413.

108. Ulijasz, A. T., Cornilescu, G., von, S. D., Kaminski, S., Mroginski, M. A., Zhang, J., Bhaya, D., Hildebrandt, P., & Vierstra, R. D. (2008) Characterization of two thermostable cyanobacterial phytochromes reveals global movements in the chromophore-binding domain during photoconversion *J. Biol. Chem.* 283: 21251-21266.

109. von Stetten, D., Seibeck, S., Michael, N., Scheerer, P., Mroginski, M. A., Murgida, D. H., Krauss, N., Heyn, M. P., Hildebrandt, P., Borucki, B. *et al.* (2007) Highly conserved residues Asp-197 and His-250 in Agp1 phytochrome control the proton affinity of the chromophore and Pfr formation *J Biol. Chem.* 282: 2116-2123.

110. Borucki, B., von Stetten, D., Seibeck, S., Lamparter, T., Michael, N., Mroginski, M. A., Otto, H., Murgida, D. H., Heyn, M. P., & Hildebrandt, P. (2005) Light-induced proton release of phytochrome is coupled to the transient deprotonation of the tetrapyrrole chromophore *J Biol. Chem.* 280: 34358-34364.

111. Bhoo, S. H., Hirano, T., Jeong, H.-Y., Lee, J.-G., Furuya, M., & Song, P. S. (1997) Phytochrome photochromism probed by site-directed mutations and chromophore esterification *JACS* 119: 11717-11718.

112. Deforce, L., Furuya, M., & Song, P. S. (1993) Mutational analysis of the pea phytochrome A chromophore pocket: chromophore assembly with apophytochrome A and photoreversibility *Biochemistry* 32: 14165-14172.

113. Remberg, A., Schmidt, P., Braslavsky, S. E., Gartner, W., & Schaffner, K. (1999) Differential effects of mutations in the chromophore pocket of recombinant phytochrome on chromoprotein assembly and Pr-to-Pfr photoconversion *Eur J Biochem* 266: 201-208.

114. Rohmer, T., Lang, C., Hughes, J., Essen, L. O., Gartner, W., & Matysik, J. (2008) Light-induced chromophore activity and signal transduction in phytochromes observed by 13C and 15N magic-angle spinning NMR *Proc. Natl. Acad. Sci. USA* 105: 15229-15234.

115. Teufel, Lotte (2010) Biochemische und biophysikalische Charakterisierung von Cph1 Mutanten.

116. Oka, Y., Matsushita, T., Mochizuki, N., Quail, P. H., & Nagatani, A. (2008) Mutant screen distinguishes between residues necessary for light-signal perception and signal transfer by phytochrome B *PLoS Genet* 4: e1000158.

117. Kikis, E. A., Oka, Y., Hudson, M. E., Nagatani, A., & Quail, P. H. (2009) Residues clustered in the light-sensing knot of phytochrome B are necessary for conformer-specific binding to signaling partner PIF3 *PLoS. Genet.* 5: e1000352.

118. Rohmer, T., Lang, C., Bongards, C., Gupta, K. B., Neugebauer, J., Hughes, J., Gartner, W., & Matysik, J. (2010) Phytochrome as molecular machine: revealing chromophore action during the Pfr --> Pr photoconversion by magic-angle spinning NMR spectroscopy *J Am. Chem. Soc.* 132: 4431-4437.

119. Möglich, A., Ayers, R. A., & Moffat, K. (2009) Design and signaling mechanism of light-regulated histidine kinases *J. Mol. Biol.* 385: 1433-1444.

120. Alam, M. T., Yamada, T., Carlsson, U., & Ikai, A. (2002) The importance of being knotted: effects of the C-terminal knot structure on enzymatic and mechanical properties of bovine carbonic anhydrase II *FEBS Lett.* 519: 35-40.

121. Saito, R., Sato, T., Ikai, A., & Tanaka, N. (2004) Structure of bovine carbonic anhydrase II at 1.95 A resolution *Acta Crystallogr. D Biol. Crystallogr.* 60: 792-795.

122. Taylor, W. R. (2000) A deeply knotted protein structure and how it might fold *Nature* 406: 916-919.

123. King, N. P., Jacobitz, A. W., Sawaya, M. R., Goldschmidt, L., & Yeates, T. O. (2010) Structure and folding of a designed knotted protein *Proc. Natl. Acad. Sci. U. S. A* 107: 20732-20737.

124. Biou, V., Dumas, R., Cohen-Addad, C., Douce, R., Job, D., & Pebay-Peyroula, E. (1997) The crystal structure of plant acetohydroxy acid isomeroreductase complexed with NADPH, two magnesium ions and a herbicidal transition state analog determined at 1.65 A resolution *EMBO J.* 16: 3405-3415.

125. Virnau, P., Mirny, L. A., & Kardar, M. (2006) Intricate knots in proteins: Function and evolution *PLoS. Comput. Biol.* 2: e122.

126. Wagner, J. R., Zhang, J., von, S. D., Gunther, M., Murgida, D. H., Mroginski, M. A., Walker, J. M., Forest, K. T., Hildebrandt, P., & Vierstra, R. D. (2008) Mutational analysis of Deinococcus radiodurans bacteriophytochrome reveals key amino acids necessary for the photochromicity and proton exchange cycle of phytochromes *J. Biol. Chem.* 283: 12212-12226.

127. Jang, I. C., Henriques, R., Seo, H. S., Nagatani, A., & Chua, N. H. (2010) Arabidopsis PHYTOCHROME INTERACTING FACTOR proteins promote phytochrome B polyubiquitination by COP1 E3 ligase in the nucleus *Plant Cell* 22: 2370-2383.

128. Al Sady, B., Ni, W., Kircher, S., Schafer, E., & Quail, P. H. (2006) Photoactivated phytochrome induces rapid PIF3 phosphorylation prior to proteasome-mediated degradation *Mol. Cell* 23: 439-446.

129. Anders, K., von, S. D., Mailliet, J., Kiontke, S., Sineshchekov, V. A., Hildebrandt, P., Hughes, J., & Essen, L. O. (2011) Spectroscopic and photochemical characterization of the red-light sensitive photosensory module of Cph2 from Synechocystis PCC 6803 *Photochem. Photobiol.* 87: 160-173.

130. Park, C. M., Kim, J. I., Yang, S. S., Kang, J. G., Kang, J. H., Shim, J. Y., Chung, Y. H., Park, Y. M., & Song, P. S. (2000) A second photochromic bacteriophytochrome from Synechocystis sp. PCC 6803: spectral analysis and down-regulation by light *Biochemistry* 39: 10840-10847.

131. Yoon, J. M., Hahn, T. R., Cho, M. H., Jeon, J. S., Bhoo, S. H., & Kwon, Y. K. (2008) The PHY domain is required for conformational stability and spectral integrity of the bacteriophytochrome from Deinococcus radiodurans *Biochem. Biophys. Res. Commun.* 369: 1120-1124.

132. Foerstendorf, H., Lamparter, T., Hughes, J., Gartner, W., & Siebert, F. (2000) The photoreactions of recombinant phytochrome from the cyanobacterium Synechocystis: a low-temperature UV-Vis and FT-IR spectroscopic study *Photochem. Photobiol.* 71: 655-661.

133. Heyne, K., Herbst, J., Stehlik, D., Esteban, B., Lamparter, T., Hughes, J., & Diller, R. (2002) Ultrafast dynamics of phytochrome from the cyanobacterium synechocystis, reconstituted with phycocyanobilin and phycoerythrobilin *Biophys. J* 82: 1004-1016.

134. Lagarias, J. C. & Lagarias, D. M. (1989) Self-assembly of synthetic phytochrome holoprotein *in vitro Proc. Natl. Acad. Sci. USA* 86: 5778-5780.

135. Wu, S. H. & Lagarias, J. C. (2000) Defining the bilin lyase domain: lessons from the extended phytochrome superfamily *Biochemistry* 39: 13487-13495.

7. Publications

Mailliet, J., Psakis, G., Sineshchekov, V., Essen, L. O. & Hughes, J. (2011) Spectroscopy and a high-resolution crystal structure of Tyr-263 mutants of cyanobacterial phytochrome Cph1 *JMB*: accepted

Song, C., Lang, C., **Mailliet, J.**, Gärtner, W., Hughes, J., & Matysik, J. (2011) Exploring chromophore-binding pocket: High-resolution solid-state ^{1}H-^{13}C intrafacial correlation spectra with windowed PMLG scheme *Appl. Magn. Reson.*: online

Psakis, G., **Mailliet, J.**, Lang, C., Teufel, L., Essen, L. O., & Hughes, J. (2011) Signalling kinetics of cyanobacterial phytochrome Cph1, a light regulated histidine kinase *Biochemistry* 50: 6178-6188.

Song, C., Psakis, G., Lang, C., **Mailliet, J.**, Gartner, W., Hughes, J., & Matysik, J. (2011) Two ground state isoforms and a chromophore D-ring photoflip triggering extensive intramolecular changes in a canonical phytochrome *Proc. Natl. Acad. Sci. U. S. A* 108: 3842-3847.

Anders, K., von, S. D., **Mailliet, J.**, Kiontke, S., Sineshchekov, V. A., Hildebrandt, P., Hughes, J., & Essen, L. O. (2011) Spectroscopic and photochemical characterization of the red-light sensitive photosensory module of Cph2 from Synechocystis PCC 6803 *Photochem. Photobiol.* 87: 160-173.

Mailliet, J., Psakis, G., Schroeder, C., Kaltofen, S., Durrwang, U., Hughes, J., & Essen, L. O. (2009) Dwelling in the dark: procedures for the crystallography of phytochromes and other photochromic proteins *Acta Crystallographica Section D* 65: 1232-1235.

Mroginski, M. A., von Stetten, D., Escobar, F. V., Strauss, H. M., Kaminski, S., Scheerer, P., Günther, M., Murgida, D. H., Schmieder, P., Bongards, C., Gärtner, W., **Mailliet, J.**, Hughes, J., Essen, L. O., Hildebrandt, P. (2009) Chromophore structure of cyanobacterial phytochrome Cph1 in the Pr state: Reconciling structural and spectroscopic data by QM/MM calculations *Biophys. J.* 96: 4153-4163.

Essen, L.-O., **Mailliet, J.**, & Hughes, J. (2008) The structure of a complete phytochrome sensory module in the Pr ground state *Proc. Natl. Acad. Sci. USA* 105: 14709-14714.

8. Table of figures

9. List of tables

10. Abbreviations

Å	Angstrom (= 0.1 nm)
Abs.	Absorbance
AC	Adenylyl cyclase
AMS	Ammonium sulfate
APS	Ammonium persulfate
AUC	Analytical ultracentrifugation
Bp	Breaking point
BV	Biliverdin
Chla	Chlorophyll a
cv	Column volume
EDTA	Ethylenediaminetetraacetic acid
Exc.	Excitation
FR	Far-red light (λ_{max} = 730 ± 20 nm)
FWHM	Full width at half maximum
GAF	cGMP phosphodiesterase/adenylyl cyclase/FhlA domain
H-bond	Hydrogen bond
HO	Heme oxygenase
IDA	Iminodiacetic acid
IR	Infra-red light (λ_{max} = 940 ± 45 nm)
k_d	Temperature-independent degradation of excitation
k_F	Rate constant of fluorescence (radiative rate constant)
k_P	Primary photoreaction (Pr → pre-lumi-R)
λ_{em}	Emission wavelength
λ_{exc}	Excitation wavelength
$\lambda_{max, abs}$	Red maximum of the absorbance spectrum
$\lambda_{max, em}$	Maximum of the emission spectrum
$\lambda_{max, exc}$	Maximum of the excitation spectrum

LB	Lysogeny broth
Milli-Q	Deionized and purified water (18.2 MΩ · cm)
min	Minute
Φ_F	Fluorescence quantum yield
Φ_P	Quantum yield of phototransformation
PAS	Period/Arnt/Singleminded domain
PCB	Phycocyanobilin
PcyA	Ferredoxin oxidoreductase
PDE	Phosphodiesterase
PHY	Phytochrome-specific domain
QM/MM	Quantum mechanics (QM) / molecular mechanics (MM)
R	Red light (λ_{max} = 660 ± 20 nm)
SAR	Specific absorbance ratio
SDS	Sodium dodecyl sulphate
T_{77K}	Temperature of liquid nitrogen (77 K)
T_a	Ambient temperature (295 – 298 K)
TEMED	Tetramethylethylenediamine

11. Appendix

11.1. SDS-PAGE analysis

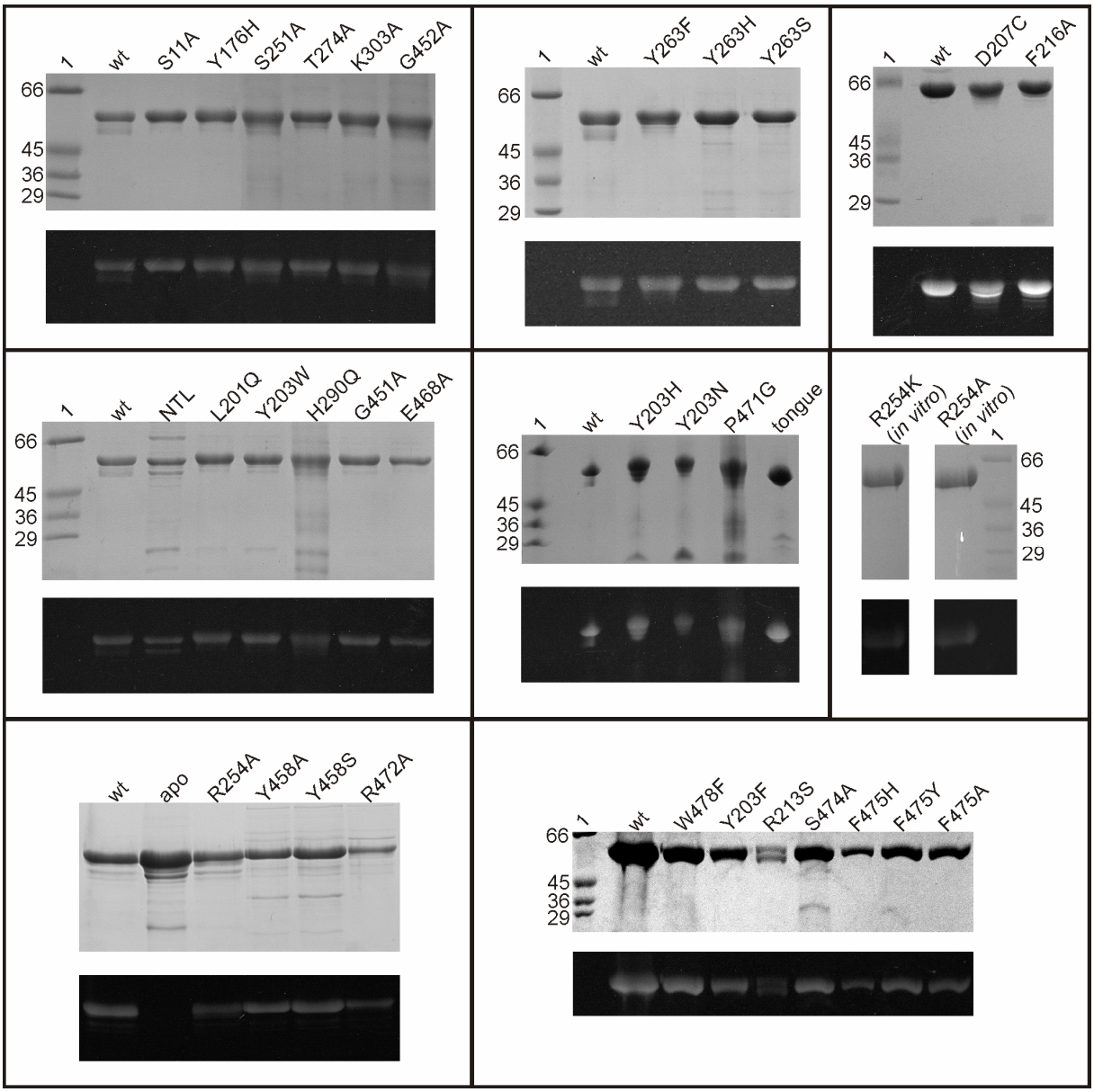

Figure 45: SDS-PAGE gels of Cph1Δ2 and investigated mutants.
SDS-gel showing Coomassie-stained proteins and PCB-assembled Cph1Δ2 and the respective mutants by zinc acetate fluorescence (above and below, respectively) after SEC. Molecular weight markers (kDa) are indicated in (1).

11.2. Spectroscopy data

11.2.1. Absorbance spectra of Cph1Δ2 and its mutants

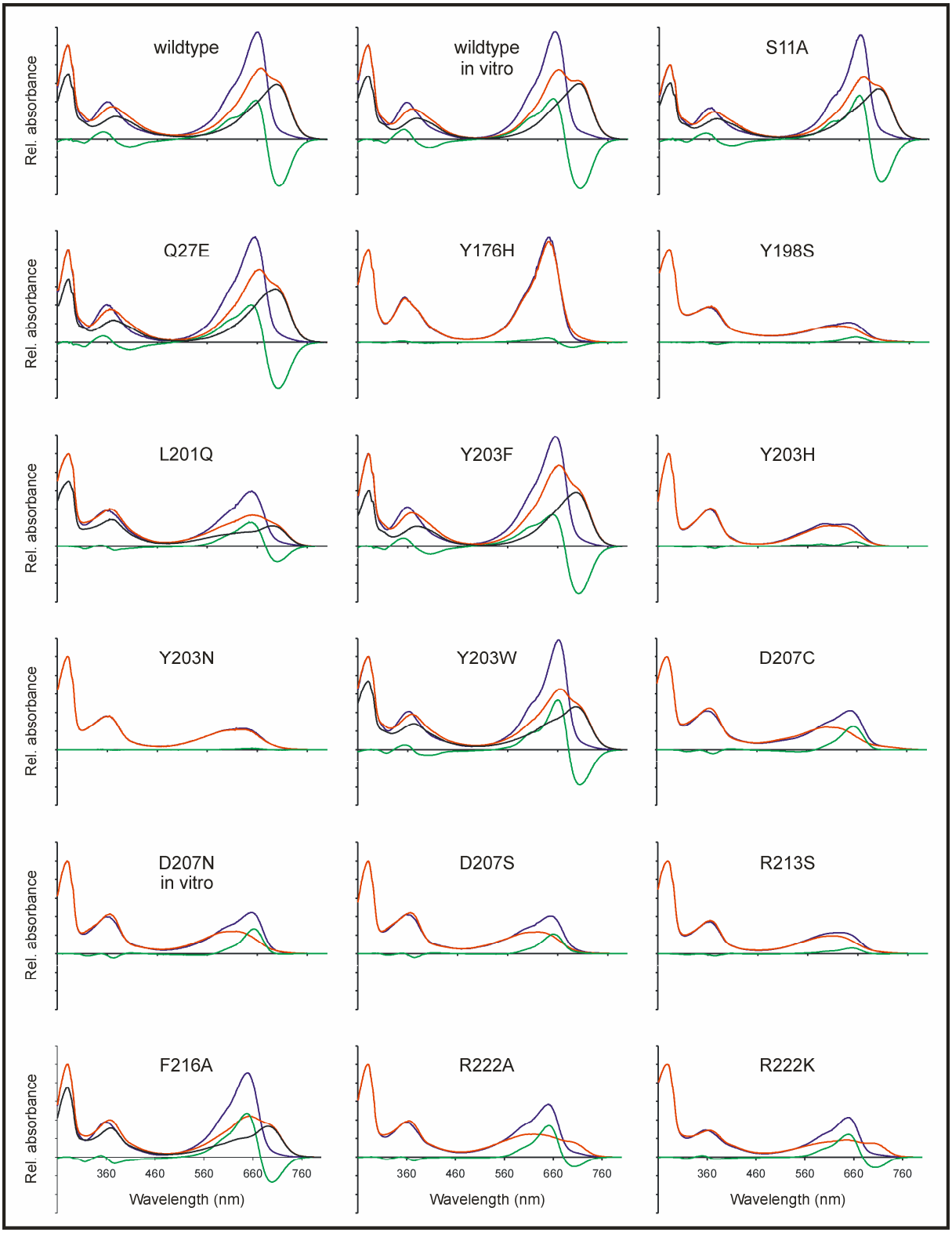

Figure 46: Absorbance spectra of Cph1Δ2 and investigated mutants (1).
The spectra were recorded after FR (blue) and R (red) irradiation. The resulting difference spectra are shown in green and the calculated Pfr spectrum (black) are based on the estimated $\chi_{Pfr,max}$ from Table 6.

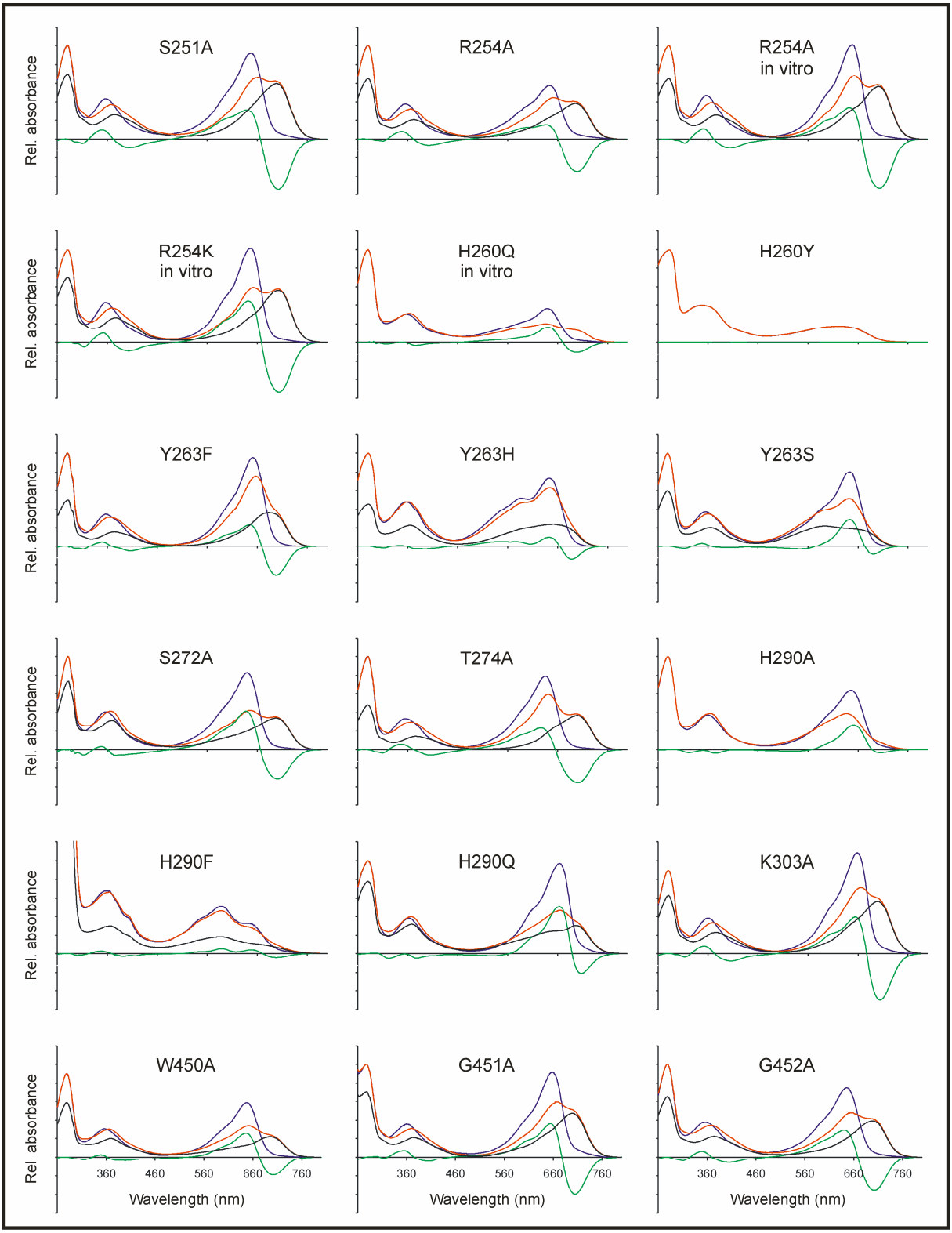

Figure 47: Absorbance spectra of Cph1Δ2 and investigated mutants (2).
The spectra were recorded after FR (blue) and R (red) irradiation. The resulting difference spectra are shown in green and the calculated Pfr spectrum (black) are based on the estimated $\chi_{Pfr,max}$ from Table 6.

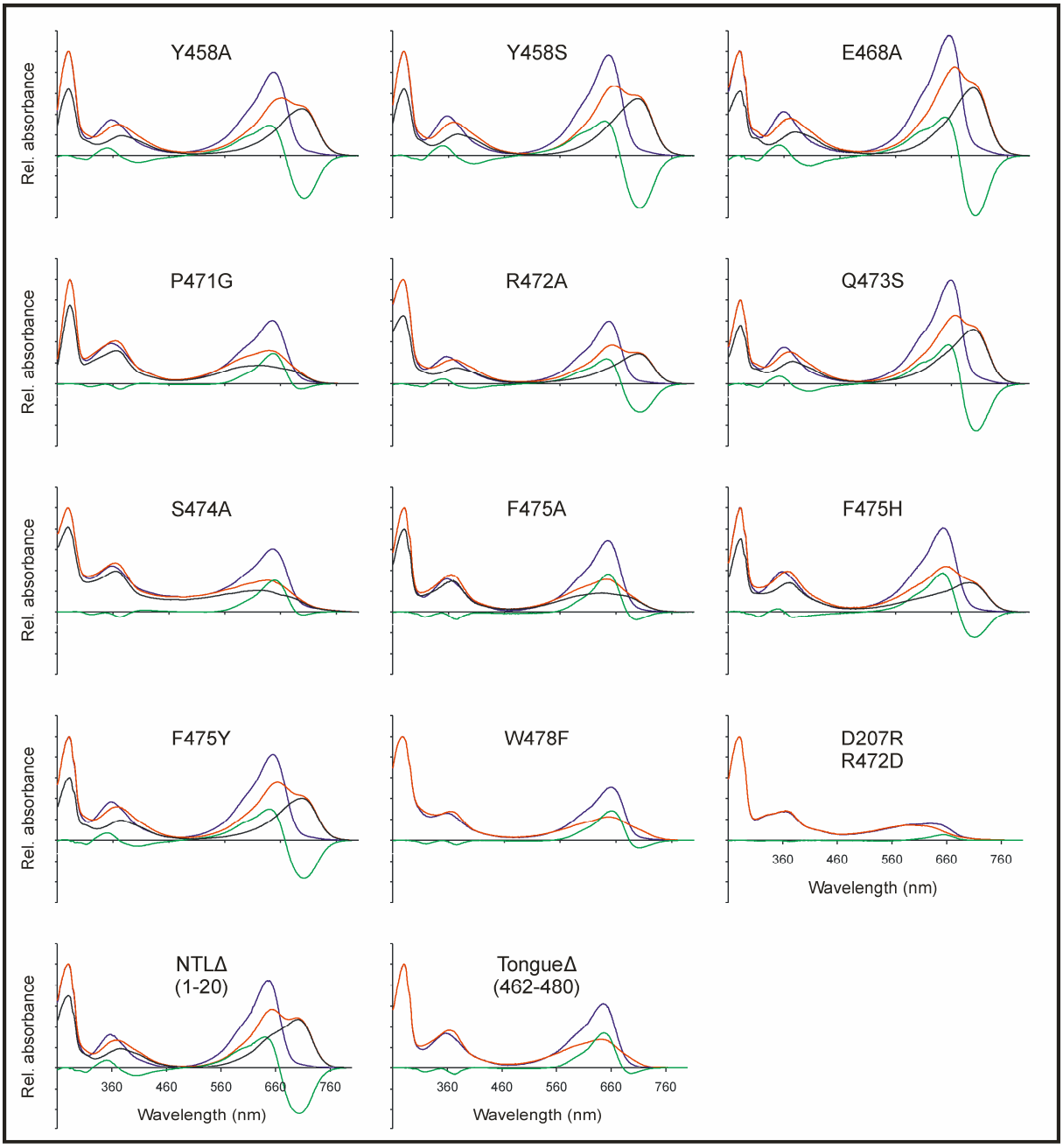

Figure 48: Absorbance spectra of Cph1Δ2 and investigated mutants (3).
The spectra were recorded after FR (blue) and R (red) irradiation. The resulting difference spectra are shown in green and the calculated Pfr spectrum (black) are based on the estimated $\chi_{Pfr,max}$ from Table 6.

11.2.2. UV-Vis absorbance characteristics of Cph1Δ2 and its mutants

Table 6: UV-Vis absorbance characteristics of Cph1Δ2 and analysed mutants.

Protein	λ_{max} (Pr) (nm)	λ_{max} (Pfr) (nm)	λ_{soret} (Pr) (nm)	ratio (Pr)	FWHM (Pr) (nm)	Δλmax (nm)	Δλibp (nm)	Δλmin (nm)	ΔAλmax / ΔAλmin	ε (Pr λ_{max}) (M^{-1} cm^{-1})	a	$\chi_{Pfr,max}$
wt	660	707	360	2.9	42	656	678	704	0.84	85000	1	0.70
wt (*in vitro*)	656	703	358	2.9	44	651	675	706	0.82	85000	1	0.70
NTL Δ(1-20)	649	701	358	2.6	44	641	667	704	0.69	68000	1	0.70
S11A	663	700	360	3.4	38	660	680	705	1.0	84000	0.9	0.75
Q27E	656	697	359	2.8	44	649	674	702	0.81	70000	1.1	0.68
Y176H	642	-	355	2.3	48	641	662	689	0.93	69500	8.9	-
Y198S	638	-	357	0.56	74	656	-	-	-	n.d.	n.d.	-
L201Q	649	691	358	1.5	56	649	677	700	1.6	65500	1.1	0.70
Y203F	655	697	359	2.8	48	650	674	703	0.67	73000	1.3	0.60
Y203H	635	-	365	0.61	72	656	-	-	-	n.d.	n.d.	-
Y203N	635	-	364	0.63	74	648	-	-	-	n.d.	n.d.	-
Y203W	662	697	364	2.9	40	660	682	704	1.4	75000	1	0.74
D207C	647	-	361	1.0	56	653	-	-	-	28000	4.1	-
D207N (*in vitro*)	650	-	359	1.1	48	655	-	-	-	32500	3.4	-
D207 R / R472D	632	-	358	0.59	82	654	-	-	-	n.d.	n.d.	-
D207S	649	-	358	0.96	50	652	-	-	-	27500	4.8	-
R213S	625	-	364	0.67	86	649	-	-	-	n.d.	n.d.	-
F216A	649	691	358	2.4	50	648	676	699	1.8	67500	1.1	0.75
R222A	650	-	358	1.5	48	651	681	703	3.3	n.d.	n.d.	-
R222K	650	-	357	1.5	46	649	679	704	2.2	n.d.	n.d.	-
S251A	647	699	356	2.1	54	639	667	702	0.59	64000	1.2	0.70
R254A	643	696	356	1.5	54	637	661	699	0.44	50000	1.5	0.65
R254A (*in vitro*)	648	701	356	2.1	46	642	667	703	0.64	63000	1.2	0.65
R254K (*in vitro*)	647	702	357	2.4	44	642	668	704	0.83	69500	0.9	0.70
H260Q in vitro	640	-	357	1.2	54	641	670	698	1.6	n.d.	n.d.	-
H260Y	621	-	348	0.4	118	-	-	-	-	n.d.	n.d.	-
Y263F	651	691	357	2.8	50	642	669	698	0.76	85000	1.2	0.50
Y263H	644	652	356	1.5	52	643	666	688	0.96	47000	3.9	0.46
Y263S	643	-	355	2.2	50	643	673	690	3.4	80000	1.6	0.60
S272A	640	697	357	2.0	50	638	667	700	1.3	55000	1.3	0.74
T274A	635	699	356	2.4	52	626	656	700	0.66	67000	1.4	0.48
H290A	646	-	361	1.7	56	652	689	704	9.0	n.d.	n.d.	-
H290F	587	-	358	0.75	152	590	671	697	1.2	n.d.	n.d.	0.46
H290Q	664	697	362	2.6	44	663	689	707	2.4	60000	2.3	0.78
K303A	659	699	361	2.8	44	654	677	704	0.79	82000	1	0.70
W450A	648	695	356	1.9	48	646	673	701	1.3	n.d.	n.d.	0.65
G451A	658	700	361	2.6	46	655	678	704	0.90	74500	1.1	0.70
G452A	646	698	356	2.0	52	639	668	702	0.81	56500	1	0.65
Y458A	648	699	356	2.3	54	640	668	703	0.72	58000	2	0.64
Y458S	647	699	356	2.5	52	640	667	703	0.67	65000	1.3	0.64
E468A	656	698	359	2.7	48	649	673	703	0.64	78000	0.9	0.62
P471G	646	-	356	1.6	52	647	682	697	6.2	37000	2.9	-
R472A	649	700	356	2.3	44	643	670	703	0.9	65500	1.2	0.65
Q473S	659	699	360	2.9	44	655	677	704	0.83	76000	1.2	0.70
S474A	647	-	358	1.4	58	649	688	701	10	n.d.	n.d.	-
F475A	645	-	357	2.1	52	645	680	697	5.0	71000	1.3	-
F475H	647	692	357	2.1	50	644	673	702	1.5	76500	1.1	0.70
F475Y	646	697	357	2.2	52	639	668	702	0.82	75500	1.2	0.60
W478F	652	-	357	1.9	50	652	684	701	4.1	n.d.	n.d.	-
Tongue Δ(462-480)	646	-	357	1.8	52	646	682	697	6.6	n.d.	n.d.	-

Ratio (Pr) designates the $A_{\lambda max,red}$ / $A_{\lambda max,\ Soret}$ oscillator ratio. FWHM was determined for λ_{max} by Gaussian approximation of the main red band, derived from the λ_{max} to 700 nm spectrum. $\chi_{Pfr,max}$ was estimated by proportionally subtracting the spectrum of Pr from that following irradiation at Pr λ_{max} as described. In some cases the extinction coefficient ε could not be determined (n.d.) due to either low protein yield or purity. The specific constant (a) designates the conversion from ΔΔA to the concentration of the protein in the sample.

11.3. Analytical size exclusion chromatography

11.3.1. Size exclusion chromatograms

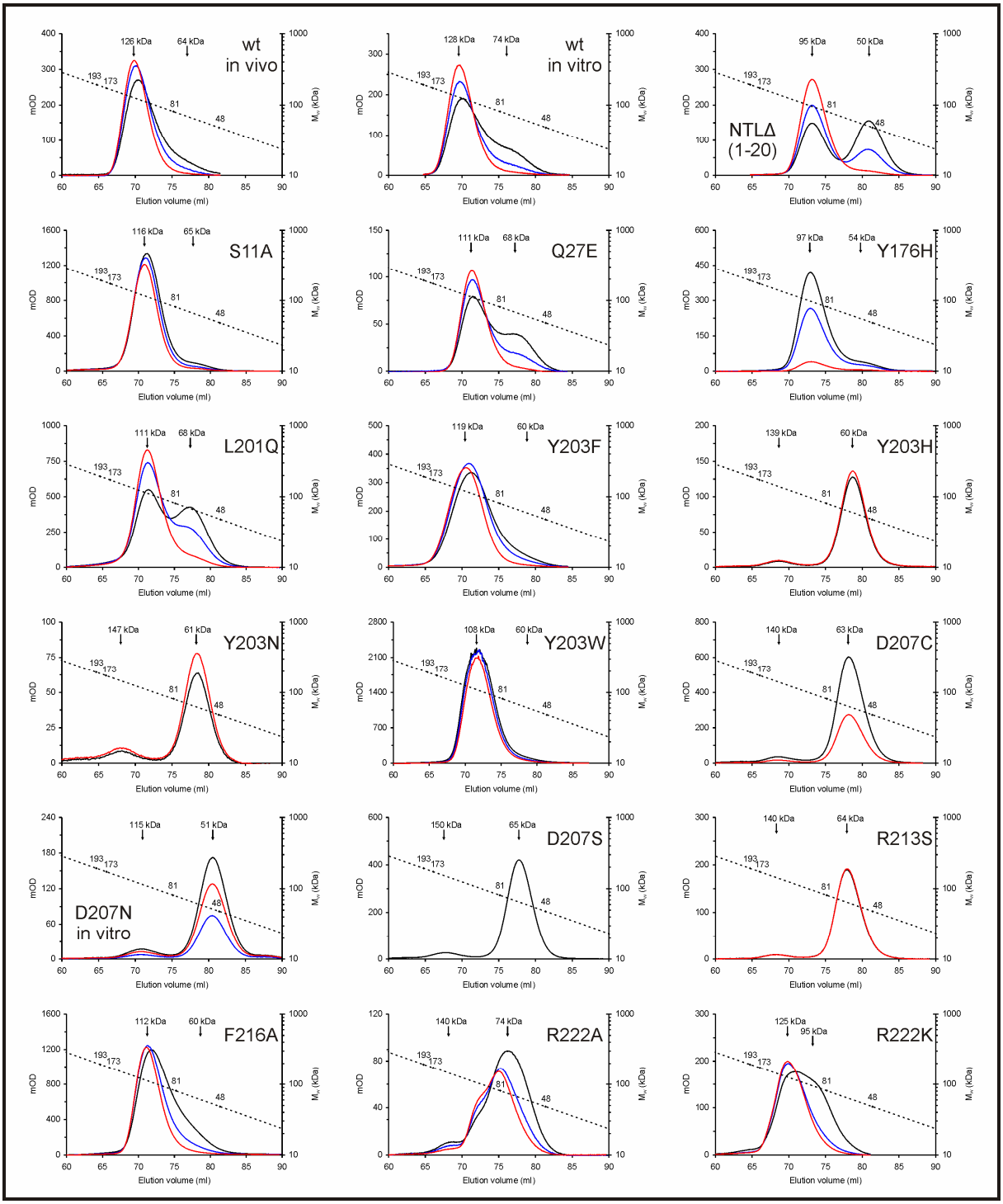

Figure 49: Size exclusion chromatography after red irradiation (1)

Size exclusion chromatography after red irradiation of Cph1Δ2 wild type (*in vivo* and *in vitro* assembled), NTLΔ (1-20), S11A, Q27E, Y176H, L201Q, Y203 mutants, D207 mutants, R213S, F216A and R222 mutants. Size exclusion chromatography runs were monitored at the $\lambda_{max,\ red\ (Pr)}$ (black) and λ_{ibp} (blue) of the specific mutants as well as at 700 nm or the respective $\lambda_{max,\ red\ (Pfr)}$ (red) for Pfr. The dotted line indicates the calibration of the column with specific proteins (kDa).

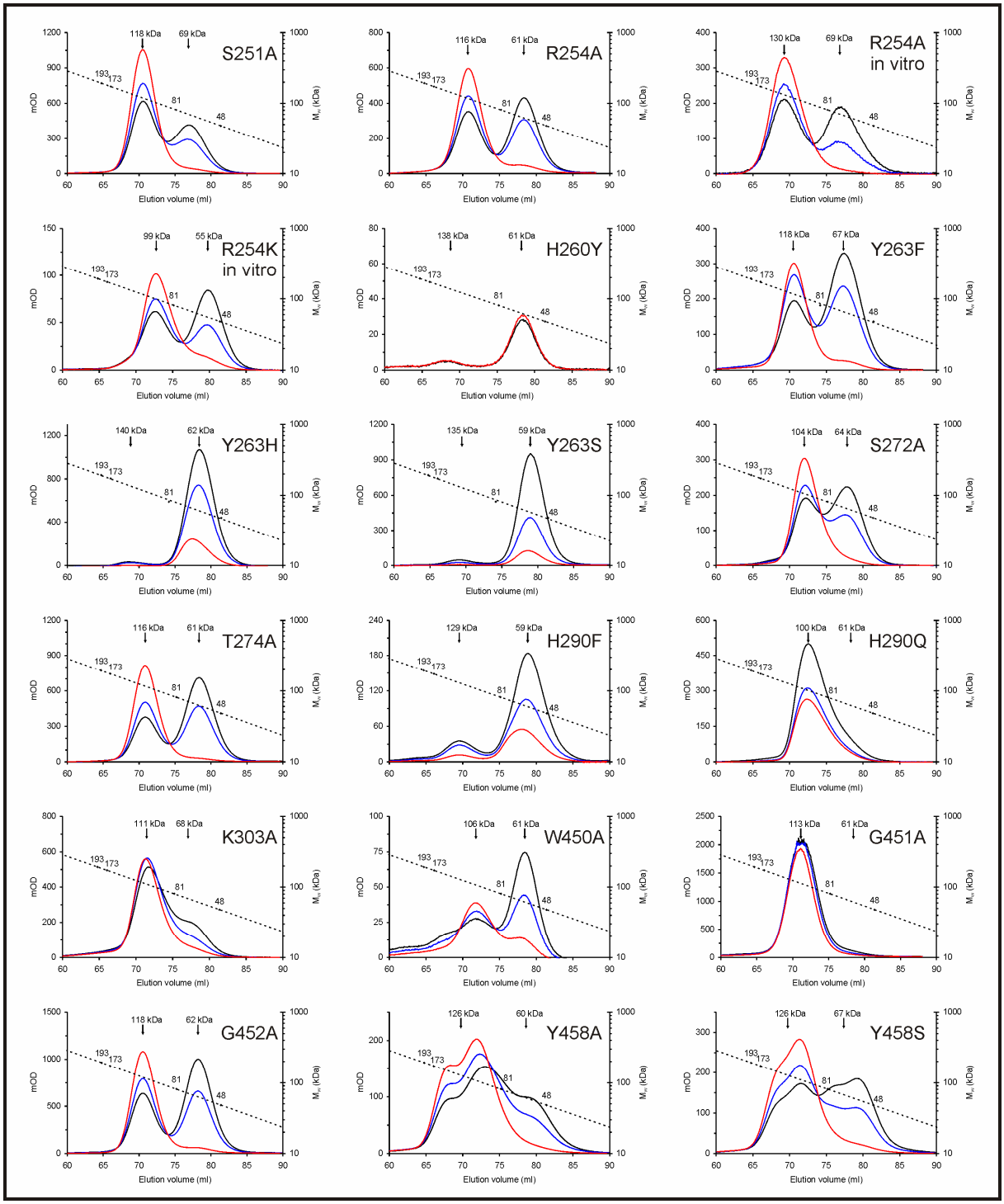

Figure 50: Size exclusion chromatography after red irradiation (2)

Size exclusion chromatography after red irradiation of S251A, R254 mutants, H260Y, Y263 mutants, S272A, T274A, H290 mutants, K303A, W450A, G451A, G452A and Y458 mutants. Size exclusion chromatography runs were monitored at the $\lambda_{max,\ red\ (Pr)}$ (black) and λ_{ibp} (blue) of the specific mutants as well as at 700 nm or the respective $\lambda_{max,\ red\ (Pfr)}$ (red) for Pfr. The dotted line indicates the calibration of the column with specific proteins (kDa).

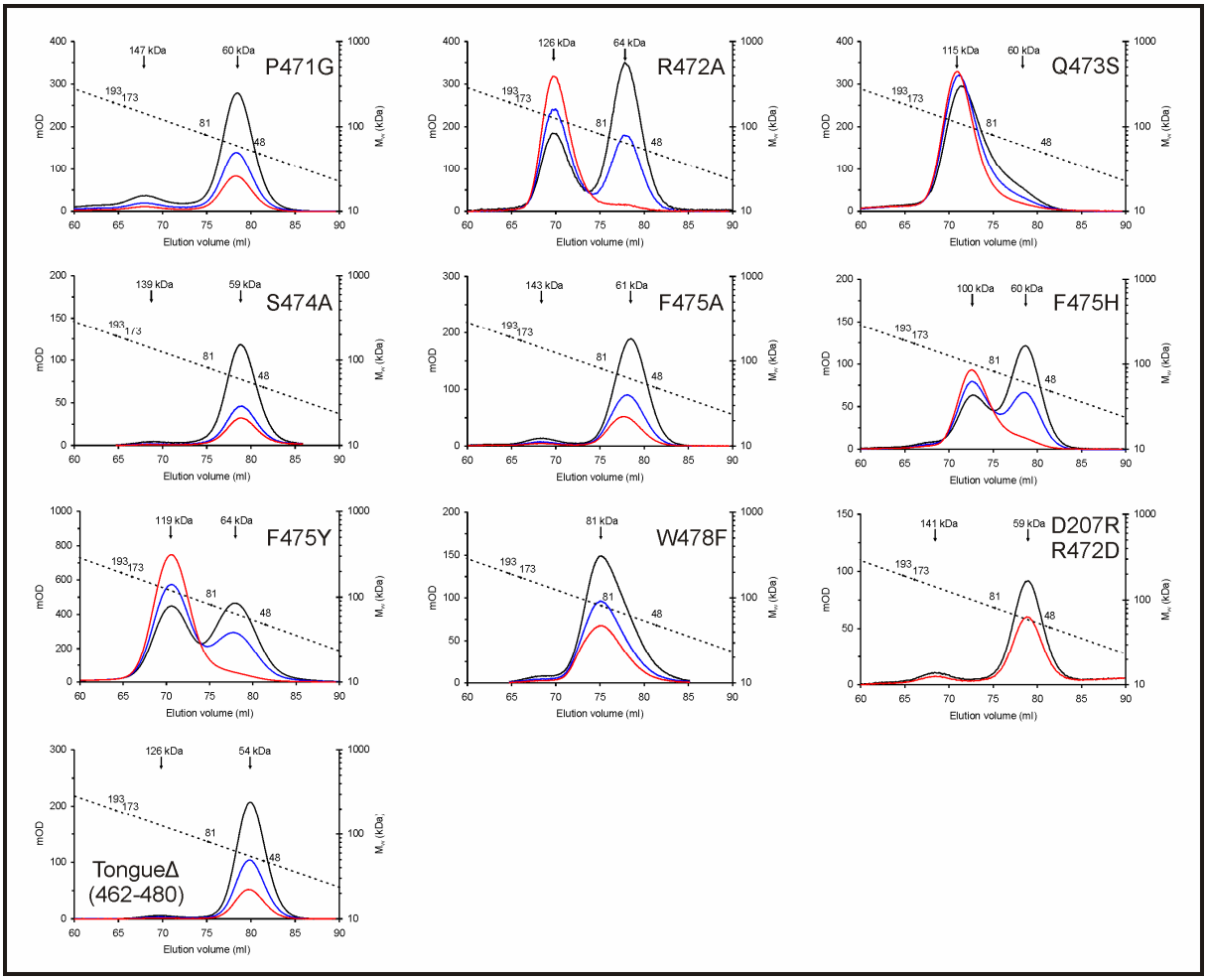

Figure 51: Size exclusion chromatography after red irradiation (3)

Size exclusion chromatography after red irradiation of P471G, R472A, Q473S, S474A, F475 mutants, W478F, D207R/R472D double-mutant and tongueΔ (462-480). Size exclusion chromatography runs were monitored at the $\lambda_{max,\ red\ (Pr)}$ (black) and λ_{ibp} (blue) of the specific mutants as well as at 700 nm or the respective $\lambda_{max,\ red\ (Pfr)}$ (red) for Pfr. The dotted line indicates the calibration of the column with specific proteins (kDa).

11.3.2. Size exclusion data table

Table 7: Analytical size exclusion characteristics of Cph1Δ2 and analysed mutants.

Protein	$c_{Protein}$ (mg / ml)	Apparent M_w (kDa)		Dimerisation		$\chi_{Pfr,max}$
		Dimer	Monomer	Pr	Pfr	
wt	2.3	126	-	√	√	-
wt (in vitro)	2.3	128	74	x	√	-
NTL Δ(1-20)	2.0	95	50	x	√	0.69
S11A	6.0	116	-	√	√	-
Q27E	1.0	111	68	x / √	√	-
Y176H	2.5	97	54	√	-	-
L201Q	5.0	111	68	x	√	0.73
Y203F	2.5	119	-	√	√	-
Y203H	2.0	139	60	x	-	-
Y203N	1.0	147	61	x	-	-
Y203W	10.0	108	-	√	√	-
D207C	8.0	140	63	x	x	-
D207N (in vitro)	2.5	115	51	x	x	-
D207 R / R472D	1.5	141	59	x	x	-
D207S	5.0	150	65	x	x	-
R213S	2.5	140	64	x	x	-
F216A	6.0	112	60	√	√	-
R222A	1.0	140	74	x	x / √	-
R222K	1.5	125	95	x	√	-
S251A	6.0	118	69	x	√	0.71
R254A	6.0	116	61	x	√	0.71
R254A (in vitro)	3.0	130	69	x	√	0.73
R254K (in vitro)	2.5	99	55	x	√	0.62
H260Y	1.0	138	61	x	-	-
Y263F	3.0	118	67	x	√	0.51
Y263H	5.0	140	62	x	x	-
Y263S	5.0	135	59	x	x	-
S272A	3.0	104	64	x	√	0.61
T274A	8.0	116	61	x	√	0.48
H290F	2.0	129	59	x / √	-	-
H290Q	5.0	100	61	√	√	-
K303A	5.0	111	68	x / √	√	-
W450A	1.5	106	61	x	√	0.54
G451A	10.0	113	61	√	√	-
G452A	10.0	118	62	x	√	0.62
Y458A	3.0	126	60	x	√	0.73
Y458S	3.0	126	67	x	√	0.63
P471G	5.0	147	60	x	x	-
R472A	4.5	126	64	x	√	0.56
Q473S	2.5	115	60	√	√	-
S474A	2.5	139	59	x	x	-
F475A	2.0	143	61	x	x	-
F475H	2.0	100	60	x	√	0.57
F475Y	5.0	119	64	x	√	0.65
W478F	2.0	-	81	x	x	-
Tongue Δ(462-480)	2.0	126	54	x	x	-

The apparent M_w of the dimer / monomer was determined based on the calibration of the column. The dimerisation of Pr /Pfr applies to the concentration used, which was approximated in the case of unknown ε (Pr, λ_{max}). $\chi_{Pfr,\ max}$ was determined by integrating the amounts of Pr (monomer) and Pfr (dimer) in the respective peaks at λ_{ibp}.

11.4. 3D structure data

11.4.1. Data statistics for Cph1Δ2

Table 8: Crystallisation statistics for Cph1Δ2 (pdb code: 2VEA)

Data collection										
Dataset (wavelength Å)	native (0.9330)			SeMet I_1 (0.9794)			SeMet I_2 (0.9780)			SeMet I_3 (0.9774)
Diffraction limits[1]	2.20 x 2.70			2.70 x 3.30			2.70 x 3.30			2.70 x 3.30
Cell (Å)	a = 77.29, c = 249.70			a = 77.69, c = 248.42			a = 77.66, c = 248.43			a = 77.67, c = 248.49
Resolution (Å)	25 - 2.2			25 - 2.8			25 - 2.8			25 - 2.8
Measured, unique refelctions	183551, 26369			146168, 14745			194934, 14834			196251, 14865
R_{merge}[2]	0.049 (0.361)			0.060 (0.376)			0.057 (0.361)			0.077 (0.636)
I/s(I)[3]	23.0 (3.5)			26.7 (3.6)			33.0 (4.8)			28.7 (3.4)
B_{Wilson} ($Å^2$)	36.7			53.9			50			52.5
Mosaicity (°)	0.4			0.38			0.38			0.32
Completeness	0.672 (0.067)			0.740 (0.138)			0.743 (0.149)			0.745 (0.149)
Phasing in SHARP										
Resolution (Å)	9.6	6.8	5.6	4.8	4.3	3.9	3.6	3.4	3.2	3.1
Figure of Merit (FOM)	0.52	0.55	0.52	0.48	0.38	0.28	0.17	0.14	0.12	0.1
Total FOM	0.32									
Total FOM after DM	0.75									
Refinement										
Resolution range (Å)	25-2.2									
Reflections (work, test)	25188, 1062									
R-factor / Rfree[4]	0.244 (0.335) / 0.270 (0.271)									
Residues	517									
Water molecules	29									
R.m.s. deviation bonds (Å)	0.006									
R.m.s. deviation angles (°)	1.298									

[1] Values correspond to maximal resolution achieved in the a* (b*) and c* direction, respectively.

[2] $R_{merge} = ((\Sigma\Sigma|I_j(h)-<I(h)>|/(\Sigma\Sigma I_j(h)) \times 100$; values in parentheses correspond to highest resolution shell.

[3] As calculated with the program TRUNCATE.

[4] $R = \Sigma||F_o|-k|F_c||/\Sigma|F_o|$ with k as scaling factor; R_{free} calculated with test set

11.4.2. Primary and secondary structure of Cph1Δ2

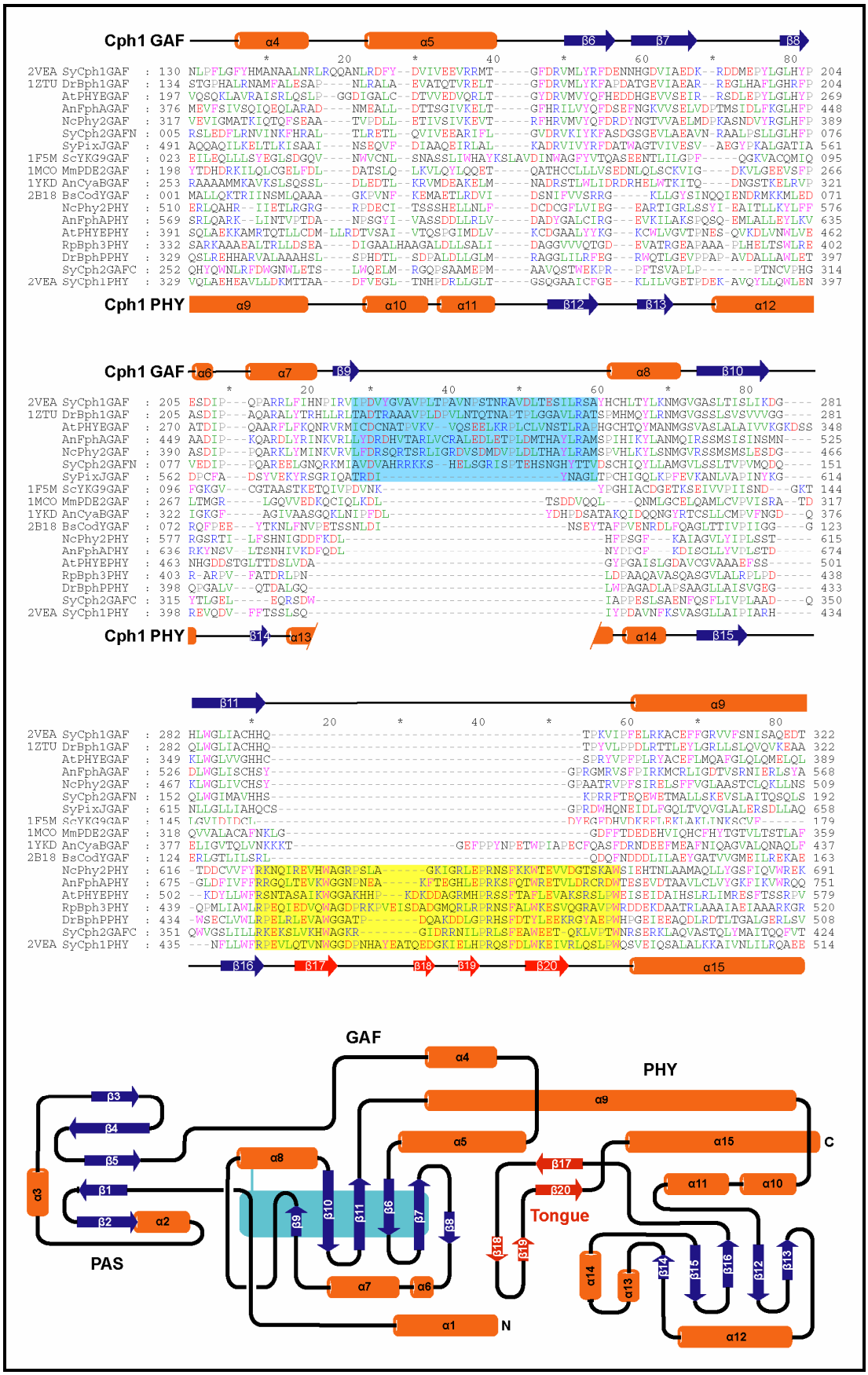

Figure 52: Primary and secondary structures of Cph1Δ2.

(Upper) Structure-based alignment of PHY and other representative GAF superfamily members performed by the program 3DCOFFEE (14) and edited manually. Acidic, basic, hydrophobic, and aromatic residues are shown in red, blue, green, and magenta, respectively. Prolines are shown in grey. The tongue of PHY and knot-forming loop of GAF domains are highlighted yellow and cyan, respectively. The secondary structures of the Cph1 GAF and PHY domains are shown in (Upper) and (Lower), respectively. The PDB coordinate files used are indicated on the left. SyCph1, *Synechocystis* 6803 Cph1 (Swiss-Prot entry Q55168); DrBph1, *Deinococcus radiodurans* BphP1 (Q9RZA4); AtPhyE, *Arabidopsis thaliana* PhyE (P42498); AnFphA, *Aspergillus nidulans* FphyA (Q5K039); NcPhy2, *Neurospora crassa* Phy2 (Q45KI2); RpBph3, *Rhodopseudomonas palustris* BphP3 (Q6NDI6); SyCph2, *Synechocystis* 6803 Cph2 (Q55434); SyPixJ, *Synechocystis* 6803 PixJ1 (Q54A85); ScYKG9, *Saccharomyces cerevisiae* YKG9 (P36088); MmPDE2, *Mus musculus* PDE2a (Q922S4); AnCyaB, *Anabaena* sp. CyaB (P94182); BsCodY, *Bacillus subtilis* CodY (P39779). The numbers of the initial and final residues aligned in each case are also shown. (Lower) Secondary structural diagram of the Cph1 sensor module. The chromophore attached to Cys-259 of α8 is shown in cyan.

11.4.3. Data statistics for Y263F

Table 9: Crystallisation statistics for Y263F

Data collection	
Beamline	ID14-2, ESRF
Detector	ADSC Q4 CCD
Wavelength (Å)	0.933
Space group	C2
Unit cell dimensions (Å)	107.57, 95.15, 73.58
Resolution (Å)	33.9 – 1.95 (2.05 – 1.95)
Total reflections	180537
Unique reflections	53522
Mosaicity	0.57
Wilson B factor (Å^2)	30.4
I / σ(I) [a]	11.1 (1.4)
R_{merge} [b]	0.085 (0.941)
Completeness (%)	99.8 (99.2)
Multiplicity	3.4 (3.1)
Refinement statistics	
Resolution (Å)	1.95
R_{work} [c]	0.174
R_{free} [c]	0.218
Reflections (F > 0)	50593
Mean B value (Å^2)	50.2
No. of atoms	4549
No. of water molecules	328
r.m.s.d. bonds (Å)	0.009
r.m.s.d. angles (°)	1.388

a) As calculated with the program TRUNCATE.

b) $R_{merge} = \Sigma_{hkl} \Sigma_i |I_i(hkl) - \langle I(hkl) \rangle| / \Sigma_{hkl} \Sigma_i I_i(hkl)$;

values in parentheses correspond to the highest resolution shell.

c) $R_{work} = \Sigma |F_{obs} - F_{calc}| / \Sigma F_{obs}$; R_{free} calculated with 5 % of the data.

11.4.4. Data statistics for Y176H

Table 10: Crystallisation statistics for Y176H

Data collection		
Dataset	1	2
Beamline	ID23-2, ESRF	ID23-2, ESRF
Detector	MarCCD 225	MarCCD 225
Wavelength (Å)	0.8726	0.8726
Space group	P4	P4
Unit cell dimensions (Å)	137.94, 137.94, 357.94	137.79, 137.79, 358.17
Resolution	64.36 – 3.50 (3.69 – 3.50)	64.30 – 3.50 (3.69 – 3.50)
Total reflections	165455	104765
Unique reflections	68367	53633
Mosaicity	0.4	0.41
Wilson B factor	35.4	32.2
I / σ [a]	2.5 (0.5)	2.0 (0.3)
R_{merge} [b]	0.464 (1.961)	0.284 (1.912)
Completeness (%)	81.8 (82.2)	64.1 (56.4)
Multiplicity	2.4 (2.3)	2.0 (1.3)

a) As calculated with the program TRUNCATE.

b) $R_{merge} = \Sigma_{hkl} \Sigma_i |I_i(hkl) - \langle I(hkl) \rangle| / \Sigma_{hkl} \Sigma_i I_i(hkl)$;
values in parentheses correspond to the highest resolution shell.

Acknowledgements

I would like to thank Jon Hughes for the supervision of my PhD thesis and for giving me the possibility to work on this project. His often nitpicking (but constructive) and sometimes frustrating attention to details nevertheless improved my way of thoroughly conducting an experiment. I appreciate the support and cooperation of Lars-Oliver Essen concerning protein crystallisation, structure determination and helpful clues on how to refine protein structures. I am grateful to have been able to work with Vitaly Sineshchekov; his expertise on phytochrome fluorescence remains unrivalled. I thank Alfred Batschauer and his group for providing me with appropriate interference filters for the kinetic studies. I would like to thank Dominique Bourgeois, David van Stetten and Stephan Kiontke for their technical assistance at the cryobenches at the ESRF in Grenoble and Marburg, respectively. I am grateful for the kind support and assistance from the group of Lars-Oliver Essen before, during and after often nerve-wracking synchrotron trips. I would like to thank the scientific and technical groups at the ESRF in Grenoble, DESY in Hamburg and SLS in Villigen for the allocation of precious beamtime at their respective synchrotons.

By joining the group in Gießen, Georgios Psakis helped me considerably by sharing thoughts not only about work and putting the focus on those areas, which needed most attention. Without the technical assistance of Christina Lang, the workflow would not be as sound as it is. I thank Kathleen Feilke and Lotte Teufel for their interest in and help during the project. I am grateful for the scientific input from and a lot of entertaining moments with Mathias Zeidler. I would like to thank Jutta Rösler for her differentiated view on the phytochrome world. I appreciate the help and support of all the people in the plant physiology institute.

I thank my parents for their patience and I am grateful for Kathi and her continuous support during my thesis and beyond.

Erklärung

Ich, Joël Mailliet, habe die hier vorliegende Arbeit selbständig und ohne unerlaubte fremde Hilfe und nur mit den Hilfen angefertigt, die ich in der Dissertation angegeben habe. Alle Textstellen, die wörtlich oder sinngemäß aus veröffentlichten Schriften entnommen sind, und alle Angaben, die auf mündlichen Auskünften beruhen, sind als solche kenntlich gemacht. Bei den von mir durchgeführten und in der Dissertation erwähnten Untersuchungen habe ich die Grundsätze guter wissenschaftlicher Praxis, wie sie in der „Satzung der Justus-Liebig-Universität Gießen zur Sicherung guter wissenschaftlicher Praxis“ niedergelegt sind, eingehalten.

Gießen, den 02.08.2011